Evaluating production scenarios of terrestrial gamma-ray flashes

Alexander Broberg Skeltved

Dissertation for the degree of Philosophiae Doctor (PhD)

Department of Physics and Technology
University of Bergen

December 2017

Preface

This sythesis and collection of papers are submitted for the degree of philosophiae doctor (PhD) in physics at the Department of Physics and Technology, University of Bergen.

The thesis is divided into an introductory part and a part consisting of three papers published in international peer reviewed journals.

1. Skeltved, A. Broberg, N. Østgaard, B. Carlson, T. Gjesteland, and S. Celestin, Modeling the relativistic runaway electron avalanche and the feedback mechanism using GEANT4, *Journal of Geophysical Results: Space Physics*, Vol 119, doi:10.1002/2014JA020504, 2014

2. Rutjes, C., D. Sarria, A. Broberg Skeltved, A. Luque, G. Diniz, N. Østgaard, and U. Ebert, Evaluation of monte carlo tools for high energy atmospheric physics, *Geoscientific Model Development*, Vol: 9, doi:10.5194/gmd-9-3961-2016, 2016

3. Skeltved, A. Broberg, N. Østgaard, A. Mezentsev, N. Lehtinen, and B. Carlson, Constraints to do realistic modeling of the electric field ahead of the tip of a lightning leader, *Journal of Geophysical Results: Atmospheres*, Vol: 122, doi:10.1002/2016JD026206, 2017

Additional paper

During my PhD studies I have also contributed to the following paper. It is not a part of the thesis.

- Østgaard, N., B. E. Carlson, R. S. Nisi, T. Gjesteland, Ø. Grøndahl, A. Broberg Skeltved, N. G. Lehtinen, A. Mezentsev, M. Marisaldi, and P. Kochkin, Relativistic electrons from sparks in the laboratory, *Journal of Geophysical Results: Atmospheres*, Vol: 121, doi:10.1002/2015JD024394, 2016

Contents

Preface iii

Acknowledgements vii

1 Introduction 1

2 Atmospheric electricity 5
2.1 Thunderclouds . . . 5
2.2 Lightning discharges . . . 8
2.2.1 Electron avalanches . . . 8
2.2.2 Streamers . . . 9
2.2.3 Leaders . . . 11

3 Observations and modeling to characterize TGFs 15
3.1 The fluence of TGFs . . . 16
3.2 Evidence of the association between lightning and TGFs . . . 18
3.3 Energy spectrum and source altitudes . . . 19
3.4 Maximum energy . . . 20

4 The production of TGFs 23
4.1 Runaway electrons . . . 23
4.2 Relativistic runaway electron avalanches . . . 25
4.3 The two leading production scenarios . . . 28
4.3.1 Acceleration and multiplication of electrons in the ambient electric field . . . 28
4.3.2 Acceleration and multiplication of electrons in the electric field of streamers and lightning leaders . . . 34
4.4 Summary . . . 40

5 Models used to describe the production of TGFs 43
5.1 Electric field models . . . 43

6 Summary of papers **47**

6.1 Paper I: Modeling the relativistic runaway electron avalanche and the feedback mechanism with GEANT4 47

6.2 Paper II: Evaluation of monte carlo tools for high energy atmospheric physics 48

6.3 Paper III: Constraints to do realistic modeling of the electric field ahead of the tip of a lightning leader 49

7 Scientific results **61**

7.1 Modeling the relativistic runaway electron avalanche and the feedback mechanism with GEANT4 63

7.2 Evaluation of monte carlo tools for high energy atmospheric physics . . 83

7.3 Constraints to do realistic modeling of the electric field ahead of the tip of a lightning leader 99

Acknowledgements

First and foremost, I would like to thank my supervisor Nikolai Østgaard. I have always found his door to be open, and his excellent guidance has been invaluable throughout both my Master and PhD Studies.

I have also enjoyed being a part of a group that encourages teamwork, and which I have found to be open and constructive. I attribute that to Nikolai as the leader of the space physics group and the Birkeland Centre and to my amazing colleagues and friends. I would like to give special thanks to the Q4 team, for all the good discussions and their help - Martino, Kolja, Andrew, Thomas, Brant, Pavlo, David and Kjetil. Some of the experiences that I have valued the most are our visits to conferences such as San Francisco and Vienna. As well as non-scientific activities - half marathon in Vienna, skiing, camping and much more.

During my PhD, I was fortunate to have two opportunities to visit Sebastien Celestin at the CNRS/University of Orléans, through the TEA-IS short visit grants. Those were important experiences and helped shape the content of my PhD.

I also enjoyed the collaboration with the group at CWI in Amsterdam, Casper, Gabriel and Ute, and with Alejandro from the Astrophysics group in Andalucia. Thanks for all the fruitful skype meetings and discussions at conferences.

I also want thank my friends and family for support and encouragement throughout all my years pursuing my interest in sports and science. I am extremely grateful.

Bergen, December 2017
Alexander Broberg Skeltved

Chapter 1

Introduction

Terrestrial gamma-ray flashes (TGFs) were discovered in 1991 by the Burst And Transient Source Experiment (BATSE) on board the Compton Gamma Ray Observatory (CGRO) *Fishman et al.* (1994). TGFs are short ($\sim 10 - 100$ μs) bursts of extremely energetic (~ 40 MeV) photons produced in the Earths atmosphere (*Marisaldi et al.*, 2010). The extreme energies of these events make TGFs the most energetic natural photon phenomena on Earth. And with their discovery, the new scientific field of high-energy atmospheric physics has emerged. The BATSE instrument was designed to detect celestial gamma-ray sources, such as cosmic gamma-ray bursts and solar flares. For that purpose, detector modules on the CGRO were positioned to provide maximum coverage of the sky. Although C. T. R. Wilson had proposed that energetic radiation could be produced in the Earth's atmosphere, the intensity and energy of TGFs had not been envisioned (*Wilson*, 1925). That is why considerable effort was made to ensure that the first observations of TGFs where indeed credible as terrestrial events (*Fishman et al.*, 1994). Hence, the discovery of TGFs by the BATSE instrument has been described as serendipitous.

Since their discovery, TGFs have been categorized with increasing accuracy. *Fishman et al.* (1994) immediately recognized that they were associated with regions of high thundercloud activity. They also linked TGFs to the prediction made by Wilson, that energetic electrons immersed in an electric field in the Earth's atmosphere could exist, and could create energetic radiation. The spectrum that was obtained from the BATSE observations were consistent with a bremsstrahlung spectrum, which of course implies a source of energetic electrons. TGFs were first thought to be produced in the quasi-electrostatic field above thunderclouds, similar to other transient events such as, sprites, elves and blue jets (*Fishman et al.*, 1994). However, they were later found to originate inside thunderclouds below 15 km altitude and often in direct association with lightning discharges (*Cummer et al.*, 2005; *Inan et al.*, 1996).

One of the most important unanswered questions on the subject of TGFs, is the

responsible production mechanism. Several scenarios have been proposed, but two remain as the most promising concepts. 1) The acceleration and multiplication of electrons in the uniform ambient electric field of the thundercloud (*Dwyer*, 2003; *Gurevich et al.*, 1992; *Wilson*, 1925). 2) The production of relativistic electrons in the non-uniform electric field in the tips of streamers and further acceleration and multiplication in the electric field ahead of lightning leaders (*Gurevich et al.*, 1992; *Moss et al.*, 2006; *Wilson*, 1925). In both scenarios, subsequent production of photons occurs through the bremsstrahlung process.

In this PhD project, we first aimed to test and constrain the two existing scenarios. We have underlined the importance of using realistic assumptions and constraints (See Papers I (*Skeltved et al.*, 2014) and III (*Skeltved et al.*, 2017)). An important part of this project has also been to compare different computer modeling toolkits (See Papers I (*Skeltved et al.*, 2014) and II (*Rutjes et al.*, 2016)). Where the scenarios can be described as the assumptions and constraints, the computer models can be considered the implementation of these to produce the results. Throughout the project we have also made an effort to understand how the scenarios can be made more realistic. As was discussed in Paper III (*Skeltved et al.*, 2017), the assumed configuration of the electric field may be an important next step to improve the production scenarios further. Although we have made some progress, further work is needed to understand how TGFs can be produced.

In chapter 2, we present relevant theoretical knowledge of the electrification of fair weather clouds to become thunderclouds. We then explain the evolution from free electrons to a highly conducting and several km long leader channel. Key points in this chapter are to understand: 1) How ionization of oxygen and nitrogen (air) depends on the strength of the electric field. 2) How the exponentially increasing rate of ionization quenches and displaces the electric field.

In chapter 3, we discuss how TGFs have been characterized from satellite observations and ground based measurements. From satellite measurements, we can derive the fluence, the intensity, the maximum energy and the energy distribution of TGFs. Ground based measurements refers to radio wave signals from lightning discharges. The purpose of this chapter is to characterize the TGFs, which can then guide the assumptions of the production scenarios.

The production scenarios are presented in chapter 4. The basic principles of acceleration and multiplication of free electrons, will be presented first. The acceleration of thermal electrons ($< 100eV$) in electric fields above the thermal runaway threshold ($E_c = 260$ kV/cm at sea level), or of energetic electrons (> 10 keV) in electric fields above the minimum ionization threshold ($E_t = 2.0$ kV/cm at sea level), and multiplication of these in electric fields roughly 30% stronger than E_t. We will emphasize that

these processes are the same in both scenarios. The differences between the two scenarios will then be made clear. That is, the configuration of the electric field and the initial source of electrons. Finally, strengths and weaknesses of the scenarios will be discussed.

Chapter 5 holds a description of different electric field configurations. We start with the simple uniform electric field that is an approximation of the ambient electric field of a thundercloud. We then discuss different approximations to the nonuniform electric field associated with lightning discharges. It will be made apparent that the screening effects associated with increased ionization rates (presented in chapter 2), may be crucial to a realistic scenario. Since the effects of these concepts have not been evaluated in this thesis, this chapter may be important for future work.

In the final chapter, we summarize the scientific contribution from the three papers that are included in this thesis.

Chapter 2

Atmospheric electricity

To early humans, electricity and lightning in particular must have been a source of fascination and awe. Lightning was attributed to mythological creatures and incorporated in most religious beliefs. For instance, the thunderbolt is the weapon held by the god Seth from ancient Egypt and by Zeus the father of all the gods in Greek mythology. In Norse mythology the thunder god Thor creates lightning with each crack of his hammer Mjollnir. Not until the end of the 16th century was electricity investigated as a physical phenomenon. In 1600, William Gilbert became the first to describe the magnetism of the Earth and to describe the attracting force created by static electricity (*Gilbert*, 1893). In 1752 Benjamin Franklin made a giant leap with his proof of the electrical nature of thunderclouds and that lightning flashes are in fact electrical currents, and finally that the Earth is itself electrically charged (*Franklin*, 1760).

In this chapter, we will provide relevant background information to understand the effects of the electric fields created in thunderclouds. We will first describe how thunderclouds are formed and how charging may occur. Then briefly discuss the different parameters that determine the charge distribution in thunderclouds. Although this charge structure can be very complicated, it is often simplified as a tripole structure. The final section contains a description of the different types of lightning discharges with a more detailed description of the development of the positive intra cloud (+IC) discharge. That includes the description of streamers and lightning leaders.

2.1 Thunderclouds

The formation of clouds and eventually thunderclouds, depends on heating of moist air at ground that subsequently rises into the atmosphere (*Cooray*, 2015, p. 71-72). The temperature of the atmosphere drops at a rate of roughly 6.5°C/km. Fair-weather clouds are formed from updrafts of warm air from ground that cools faster than the

surrounding atmosphere. The moist air will then condensate into microscopic water drops, which become the visible cloud. The thundercloud, however, develops from a fair-weather cloud when the updraft of warm air cools slower than the surrounding air. This happens if the updraft is sufficiently moist, condensation will then continuously supply heat and therefore sustain a higher temperature. This column of rising air is the first stage of the formation of a thundercloud, often referred to as the cumulus stage.

At different temperatures the water particles attain different forms. Some start to freeze at temperatures below 0°C, but some even remain supercooled liquid particles to a temperature of -40°C. Below -40°C all water particles freeze. Some of the supercooled liquid particles collide with ice crystals and then freeze on impact. The ice crystals can then grow from μm to cm scale. These growing ice crystals are called graupels. When the graupels increase in size, they become heavier and eventually start to fall. The thundercloud is then said to be in a mature stage.

Ice-Graupel mechanism

The falling graupels are considered to be a likely source of charge generation in thunderclouds. While the larger graupels are falling, the lighter ice crystals and super cooled particles will rise with the updraft. Upon impact between falling graupels and the lighter cloud particles, the graupels become charged. The ice-graupel mechanism is largely based on experiments reported in *Takahashi* (1978) and *Jayaratne et al.* (1983). They used a cloud chamber that held a mixture of ice crystals and supercooled droplets, and introduced probes to simulate falling graupels. The results showed that the polarity and amount of charge on the probes varied depending on primarily water content and temperature.

A very convincing result was the dependence of the polarity of the charge gained by the probes on temperature. From that result, *Takahashi* (1978) and *Jayaratne et al.* (1983) could predict the polarity of charge regions in thunderclouds given the temperature. Typically, falling graupels will first leave behind positive charge in the cold upper regions of a cloud. In the center of the cloud, at altitudes corresponding to temperatures between -10°C and -20°C, the graupels leaves negative charge. For temperatures above -10°C, the graupels again leave a net positively charged region. The results show that the ice-graupel mechanism can describe both the charge structure and the magnitude of the charge generated in a typical thundercloud.

Tripole structure

Although the charge structure of a thundercloud can be very complicated, a simple tripole model is generally accepted as a good and convenient approximation (*Williams*,

1989). Normal water content in a thundercloud is around 1 g/m^3. Under that condition, the temperature range given in the previous section is in accordance with the experimental results of *Jayaratne et al.* (1983); *Takahashi* (1978). The tripole structure is then assumed to consist of a main negative charge layer (MN) at the center, an equally strong positive charge layer in the upper region (UP) and a much weaker positive charge layer (LP) at the cloud base. This is illustrated in Figure 2.1. A typical representation of the tripole model is shown on the left, with charge layers at altitudes of 2 km, 7 km and 12 km. On the right side we show the electric field measurements from an ascending balloon (taken from Figure 2d in *Stolzenburg et al.* (2007)). We have indicated the location of the charge layers with the squares on the right side of the figure. Note that the altitudes, the vertical separation and extent of the charge layers vary, but the MN charge layer is often found to be consistent with the temperature range found by *Takahashi* (1978) and *Jayaratne et al.* (1983) (-10°C and -20°C).

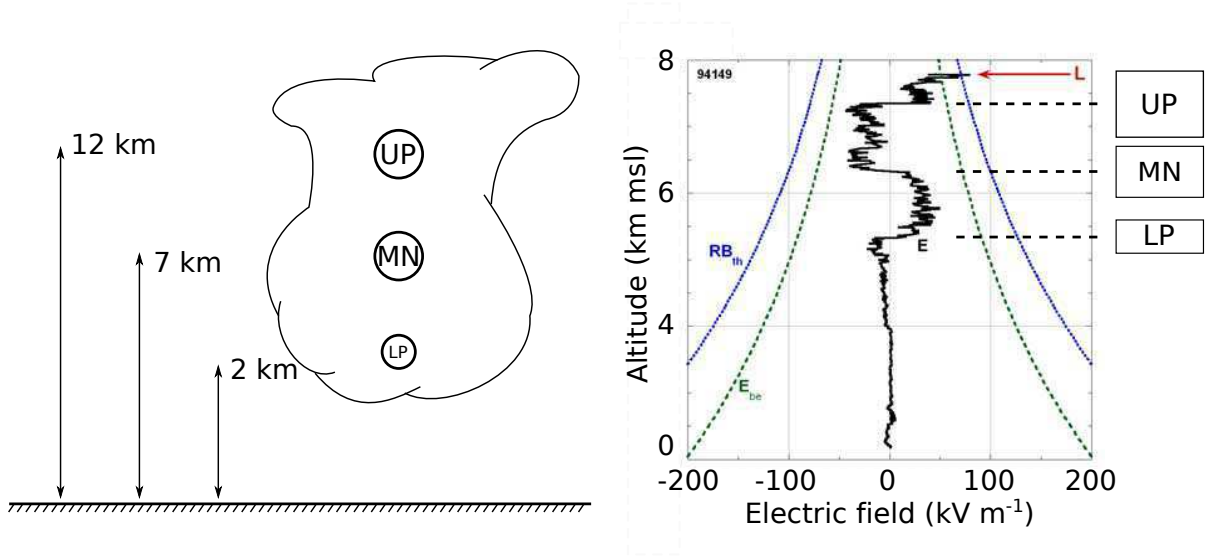

Figure 2.1: On the left: A tripole that represents a generalized simple model of the charge structure of a thundercloud. A main negative (MN) charge layer at 7 km, an equally charged upper positive (UP) charge layer at 12 km and a much weaker lower positive (LP) charge layer at 2 km altitude. On the right: Electric field measurements from an ascending balloon, taken from Figure 2d in *Stolzenburg et al.* (2007). The squares on the right side of the figure indicate the location of the charge layers, which from these measurements can be well represented as a tripole structure.

As the amount of charge in the charge layers builds, the ambient electric field increases. Balloon soundings have shown that the vertical profile of the ambient electric field inside thunderclouds can be well represented by a tripole structure (*Marshall and Rust*, 1991; *Marshall and Stolzenburg*, 1996, 2001; *Stolzenburg et al.*, 2007), as was il-

lustrated in Figure 2.1. The strength of the ambient electric field depends on the amount of charge in the charge layers and the vertical separation between them. Measurements show that the typical electric field is relatively uniform with a field strength between 0.2 kV/cm and 0.5 kV/cm. These typical electric field strengths can be exceeded at certain moments in time. For instance, during one of the balloon ascents reported in *Stolzenburg et al.* (2007), they measured an increase in electric field up to 2 kV/cm at 12 km altitude 15 seconds prior to the occurrence of a discharge (note that this case is not included in Figure 2.1). Electric field strengths above the conventional breakdown threshold, $E_k = 32$ kV/cm at sea level (~ 7.3 kV/cm at 12 km), has as far as we know not been measured.

2.2 Lightning discharges

Lightning discharges can be grouped into four types. 1) Those that connects to the ground known as cloud-to-ground (CG) discharges. 2) Those that develop within a cloud, termed intra cloud (IC) discharges. 3) Discharges between clouds, cloud-to-cloud (CC), and 4) discharges from cloud to air (CA). It is believed that roughly 75% of discharges are ICs (*Rakov and Uman*, 2003, p. 4). CG lightning constitute most of the remaining lightning, while CC and CA are much less common. The most common type of ICs is the +IC discharge that typically develops from the MN charge region to UP charge region. Incidentally, this is also the type of discharge most closely related to the observation of TGFs from space.

The basic concepts that can explain the initiation (which is still considered an unanswered question) and development of an IC leader will now be presented. In short, the development from free electrons to thermal electron avalanches, into self propagating streamers and finally the transition into highly conducting leader channels. The stepped development of the negatively charged end of leader channels will be given extra attention due to its relevance for the production of TGFs.

2.2.1 Electron avalanches

At any moment in time, roughly 10 free electrons exist per cm^{-3} of air at sea level density and pressure (*Cooray*, 2015, p. 7). Most likely, these are either secondary electrons from cosmic ray particles or the product of radon decay from the Earth itself. They have a lifetime on the order of nanoseconds due to attachment to O_2 molecules. When immersed in an electric field these electrons will rapidly gain energy. If the electrons' energy exceeds the ionization energy of nearby oxygen (~ 12 eV) or nitrogen (~ 16 eV) atoms, inelastic collisions may excite or ionize the atoms and consequently

emit additional electrons. An increase of the number of electrons n with distance z, depends on the balance between attachment η and the number of ionizing collisions α, by

$$n = \exp\left((\alpha - \eta)z\right). \tag{2.1}$$

For low energy electrons, the number of collisions increases with increasing electric field strength (and energy), while the rate of attachment decreases. The critical electric field strength that leads to equal rates of attachment and ionization, $\alpha = \eta$ is called the conventional breakdown threshold. This is typically assumed to be $E_k = 32$ kV/cm at sea-level density and pressure (*Moss et al.*, 2006). This rapid development of avalanches give rise to emission of visible light, and is called a corona discharge.

Electric field strengths close to the conventional breakdown threshold have not been observed in thunderclouds. How can one then explain the initiation of electron avalanches in electric fields much weaker than E_k? *Dwyer and Uman* (2014) summarizes a few possible solutions to this unresolved question. 1) That the electric field is in fact larger than E_k, but has not been measured. 2) That the very local and strong intensification of the electric field surrounding sharp edges of cloud particles (hydrometeors) is enough to produce electron avalanches. 3) That a breakdown occurs due to intensification of the electric field ahead of relativistic runaway electron avalanches (RREAs) that are initiated by cosmic air showers. These avalanches are different from the thermal electron avalanches that have been discussed in this section (see section 4.2 for a detailed description of RREAs). An important differences in this context is that the spatial scale of a breakdown due to RREAs would be on the order of tens to hundreds of meters, compared to mm scale of 2). *Dwyer and Uman* (2014) also make the point that 2) and 3) are likely coupled as a breakdown due to RREAs is likely to occur near the sharp edges of hydrometeors.

2.2.2 Streamers

As discussed above, the criterion for an electron to develop into an electron avalanche is that it is accelerated by an electric field $E > E_k$. The distance z_c over which the electric field is larger than E_k determines the total number of electrons by Eq. 2.1. In addition, the avalanche will locally increase the electric field in proportion to the number of electrons. When this electric field increases enough to sustain the avalanche beyond the critical length z_c, the avalanche has transitioned into a self sustained streamer. This critical number of electrons, known as the Raether–Meek criterion, has been suggested to be on the order of $10^8 - 10^9$. We can consider the very simple approximation of the streamer as a point charge with charge $Q = 10^8 e$, where e is the elementary charge $1.6 \cdot 10^{-19}$C. The distance to where E falls below E_k is roughly 200 μm ahead of the

streamer. This distance is known as the boundary of the active region of the streamer, or the boundary within which ionization continues to occur due to the intensification of the electric field created by the streamer itself. It is likely that the propagation of streamers is then largely sustained by photo ionization of UV photons that are absorbed within the active region of the streamer (*Liu and Pasko*, 2004). In Figure 2.2, we illustrate the transition from a free electron to an avalanche and eventually into a streamer. On the left we show how a single free electron multiplies through ionization. And on the right, how the avalanche has become a self sustained streamer when an active region is created ahead of its tip.

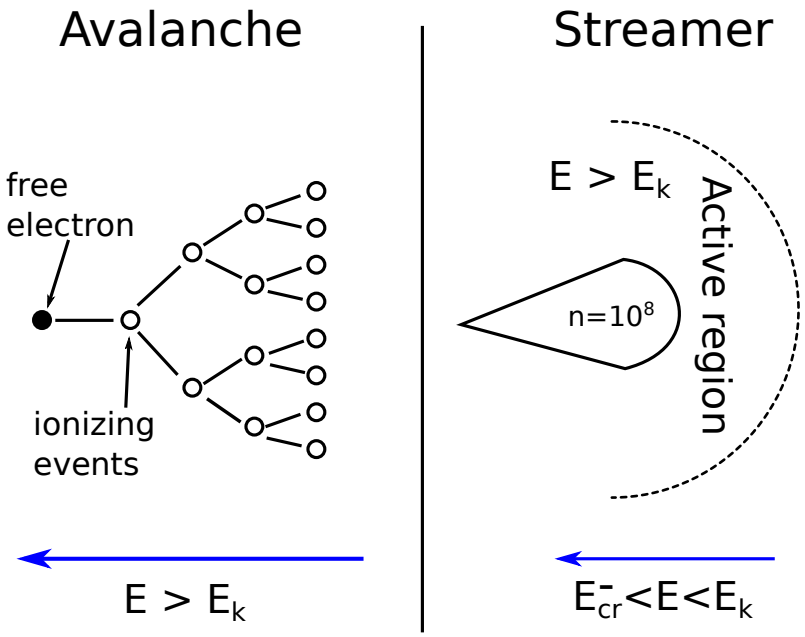

Figure 2.2: On the left, we show how a free electron ionizes and thereby multiplies to become an electron avalanche. On the right, the Raether-Meek criterion is fulfilled and number of electrons is large enough to have created an active region ahead of the avalanche. It has then transitioned into a streamer. The active region is shown as the dashed line. Note that deciding parameter, is the strength of the ambient electric field which is $E > E_k$ on the left, and $E_{cr}^- < E < E_k$ on the right.

Due to the high rate of attachment, streamers quickly become isolated when they propagate beyond the high-field region ($> E_k$). However, in a background electric field larger than roughly $E_k/8 \approx E_{cr}^+$ for positive streamers and $E_k/3 \approx E_{cr}^-$ for negative streamers, they remain self sustained. The isolation of the streamers means that they are also characterized by their low current and conductivity. As the electric field increases, however, the streamers become faster, more numerous and also have a larger current. With a sufficient number of streamers present, the sum of their relatively weak currents becomes large. That can lead to significant heating of the heavier ions and neutral atoms, and eventually the formation of a highly conducting leader channel.

2.2.3 Leaders

In streamers, the electron population has a much higher temperature than the heavier atoms. The streamer to leader transition can be described as the transfer of that energy from the electrons to the surrounding ions and neutral atoms. In that way a heated and highly conducting channel is created. As was explained in the previous section, in a sufficiently strong electric field, the number of electrons increases quickly. Energy transfer at this stage is primarily due to attachment and vibrational excitation. When the electron density reaches roughly 10^{17} cm^{-3}, coulomb interaction between the electrons and ions become important (*Cooray*, 2015, p. 19). When this happens, the rapid energy transfer from the high density of electrons to ions start to equalize the temperature. Furthermore, an increase in the kinetic energy of the ions lead to thermal ionization. That is ionization through collisions between ions and neutral atoms. With thermal ionization, the number of electrons increases further. The sum of the heating ions, the heating of neutral atoms, and the increase in electron density, leads to a local increase in the conductivity in what is called a leader stem. The temperature of the gas will eventually reach a state of thermal equilibrium (electrons ions and neutrals have the same temperature). At that stage, the leader stem has transitioned into a highly conducting (up to 10^4 S/m) leader channel. Although the duration of the streamer to leader transition in a natural lightning leader is not known. It is reasonable to assume a timescale below μs, but not instantaneous.

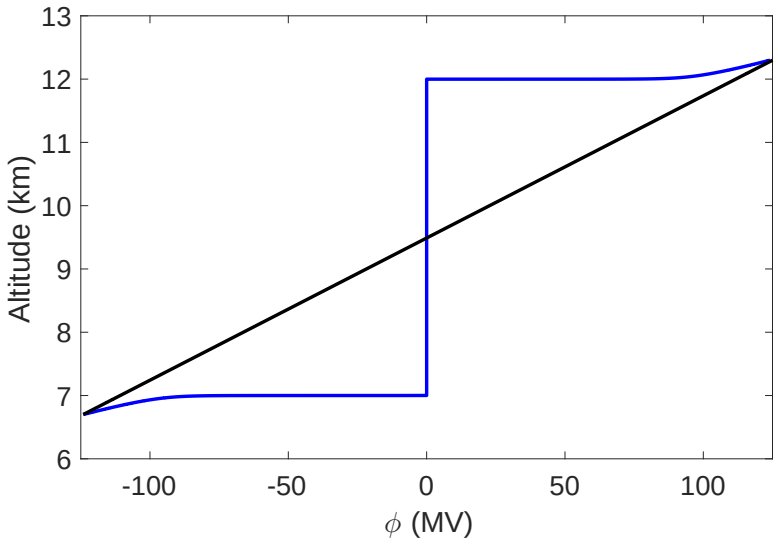

Figure 2.3: The potential difference in a thundercloud with an ambient electric field of 0.4 kV/cm. The ambient potential difference from 6.7 km to 12.3 km is shown as the black line. The corresponding potential drop through center axis of a leader that extends from 7 km to 12 km altitude in the same field is shown as the blue line. On the x-axis we show the potential with respect to the center of the leader.

The conducting leader channels have a radius of up to a few cm and can develop to a length of up to several km (*Rakov and Uman*, 2003, p. 5). The length is determined from the gap between regions with higher charge density of opposite polarity, which when connected discharges the channel. IC leaders are bidirectional. Typically, the positively charged end develops continuously towards the MN charge layer, and the negatively charged end develops in a stepped manner towards the UP charge layer. As they propagate, the amount of charge in each end, and the potential difference between the two tips, increases. This increase depends on the strength of the ambient electric field and the length of the leader. Although, the leader channel has a finite conductivity, it is customary to approximate it as a perfectly conducting object immersed in a uniform electric field. The potential drop through the center of the channel is then 0, but accumulates ahead of its tips, as shown in Figure 2.3.

The potential difference from the tip of the leader to the distance where the leader field is negligible compared to the ambient electric field, can be expressed by

$$\Delta\phi_{\text{tip}} = \frac{1}{2}\int_{h_\text{o}}^{h_1} E_\text{o}(h)dh = \frac{E_\text{o}^{av}\cdot L}{2}, \tag{2.2}$$

where h_o and h_1 is the lower an upper altitude of the channel, $E_\text{o}(h)$ is the ambient electric field at altitude h and E_o^{av} is the average ambient electric field over the full length L of the leader. This approximation has been used by several studies that consider the electric field created by the leader (*Celestin and Pasko*, 2011; *Celestin et al.*, 2015; *Köhn and Ebert*, 2015; *Mallios et al.*, 2013; *Pasko*, 2013; *Xu et al.*, 2012, 2015).

The development of a bidirectional leader is illustrated in Figure 2.4, which will be referred to throughout this section. Once the leader channel is established, the two ends begin to develop. The formation of negative streamers in the high field region ($> E_k$) close to the leader tip is necessary to sustain the leader development. Hence, this region is called the streamer zone. The electric field (blue) that is directed away from the positive leader tip (left side) accelerates the negative streamers (red arrows) towards the leader tip. Thereby, the positive ions in the leader tip become neutralized and the ions left in the wake of the streamers form the new tip, a continuous process. In the streamer zone ahead of the negative tip of the leader, negative streamers are accelerated away from the tip (right side of Figure 2.4). After the initial expansion of the streamer zone, a leader stem forms at a distance of between several tens (*Rakov and Uman*, 2003) to hundreds (*Cummer et al.*, 2015) of meters ahead of the channel. It is not well understood, how and why this space leader is formed. The space leader is also bidirectional, with a positive end that develops toward the main leader tip, and a negative end that develops much slower in the opposite direction. Both are preceded by smaller streamer zones of their own. When the leader and space leader attach, a

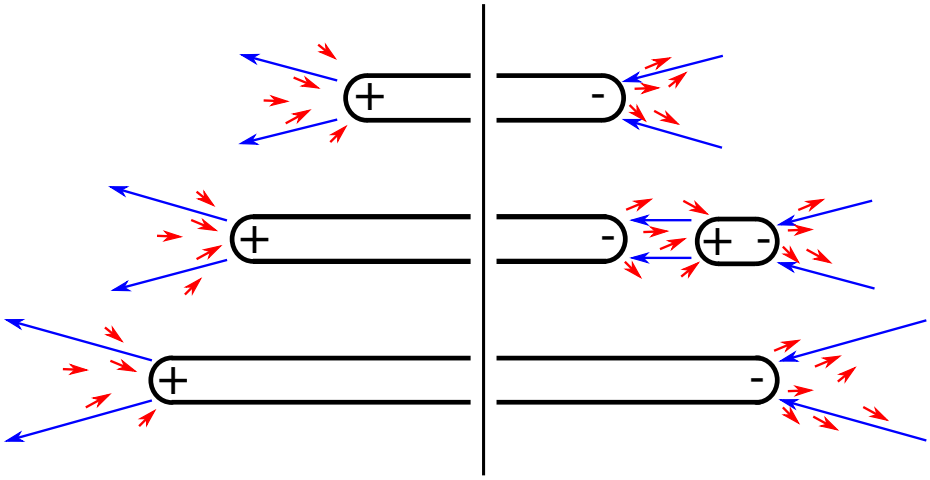

Figure 2.4: Illustration of the development of the bidirectional IC leader. The continuous development of the positive end is shown on the left, while the stepped development of the negatively charged end is shown on the right. The blue arrows illustrates the electric field lines, while the red arrows symbolizes the direction of streamers ahead of the leader tips.

discharge wave redistributes the charge such that the negative tip of the space leader becomes the new (main channel) leader tip (*Bazelyan and Raizer*, 2000, p.197-198). How quickly the charge redistributes during and after attachment is, as far as we know, poorly understood. However, it will become apparent that this open question is important to understand the relationship between lightning and production of TGFs.

Chapter 3

Observations and modeling to characterize TGFs

In the early 1900s C.T.R Wilson followed in the line of scientists interested in the electrical properties of thunderclouds. Wilson received his Nobel prize in 1927 for his method of making the paths of electrically charged particles visible by condensation of vapor (cloud chambers). With the use of cloud chambers he found that the friction force of electrons decreases with increasing energy (*Wilson*, 1925). Realizing this, he postulated that high-energy radiation could be produced in the strong electric fields in thunderclouds (*Wilson*, 1924, p. 6):

"It would be of interest to test by direct experiment whether a thundercloud does emit any measurable amount of extremely penetrating radiation of β- or γ-ray type."

The discovery of Terrestrial gamma-ray flashes (TGFs) was made more than 60 years later by the Burst and Transient Source Experiment (BATSE) on board the Compton Gamma Ray Observatory (CGRO) in 1991 (*Fishman et al.*, 1994). Since then, a combination of satellite measurements (*Briggs et al.*, 2010; *Marisaldi et al.*, 2010; *Smith et al.*, 2005) and radio atmospherics ("sferics") from lightning (*Inan et al.*, 1996) have improved our understanding over a period of more than three decades. Computer models that aim to explain the measurements have further expanded our knowledge, but are to some degree limited by the quality of the observations. In the following sections, we aim to describe the characteristics of TGFs from the observations. These will be used as a baseline when the proposed production scenarios are presented in Chapter 4.

3.1 The fluence of TGFs

A very important and difficult question to answer is: How common are TGFs? Firstly, to fully understand how common TGFs are, one must define exactly what a TGF is. For instance, what is the minimum and maximum energy threshold and what is the intensity that can be considered a TGF? Must a TGF escape the Earths atmosphere to be a TGF? Although we will not attempt to address these questions, we will summarize the current knowledge based on observations done so far.

Although they provided the important first detection of TGFs, *Fishman et al.* (1994) noted that only the stronger events could trigger the recording mode of the BATSE instrument. The reason was the duration of the trigger window, which was 64 ms and significantly longer than the duration of a TGF. Thus, only strong events would give a sufficiently large signal to noise ratio and trigger the instrument. The Reuven Ramaty High Energy Solar Spectroscopic Imager (RHESSI) satellite on the other hand, telemeters all its data to ground allowing postobservation analysis of the recorded data (*Smith et al.*, 2005). While BATSE discovered 78 TGFs between 1991 and 2000 (https://gammaray.nsstc.nasa.gov/batse/misc/ triggers.html), RHESSI reported 86 TGFs over the first 6 months. Furthermore, *Grefenstette et al.* (2009) developed an algorithm to search the stored data for new TGFs and found a total of 820 TGFs that was then reported in the first RHESSI catalog. These results already confirmed that TGFs are much more common than first thought.

Two newer satellites capable of observing TGFs are the Fermi Gamma-ray Burst Monitor (Fermi) (*Briggs et al.*, 2010) and the Astrorivelatore Gamma a Immagini Leggero (AGILE) satellites (*Marisaldi et al.*, 2010). Initially, the TGF detection rate of AGILE was roughly 0.3/day (*Marisaldi et al.*, 2015). However, detections were significantly affected by dead time due to an anticoincidence shield that inhibited detection of events shorter than 100 μs. Realizing this, a new software configuration was implemented that increased the AGILE detection efficiency by an order of magnitude to 3.0/day (*Marisaldi et al.*, 2015). Fermi carries a Gamma-ray Burst Monitor (GBM) that enables the detection of gamma rays in the 100 keV to 40 MeV energy range. The GBM consists of two sets of scintillating detectors. 12 sodium iodide (NaI) scintillating detectors that covers the energy range from 100 keV - 1 MeV, and 2 bismuth germanate (BGO) scintillating detectors that covers the energy range from 200 keV to 40 MeV. Initially, TGF detection relied on triggering the NaI detectors. However, the energy of TGFs extend well into the range of the BGO. When the triggering algorithm was improved to include the BGO, the TGF detection efficiency increased from roughly 0.03/day to 0.25/day (*Fishman et al.*, 2011). Another improvement was made when the capacity for telemetry of data to ground

was increased and continuous collection of data, over parts of the orbit, was possible (*Briggs et al.*, 2013). Fermi is currently operating with continuous telemetry of data (https://fermi.gsfc.nasa.gov/ssc/data/access/gbm/tgf/). Based on the detection from the selective collection, *Briggs et al.* (2013) estimated the detection rate to be ≈ 2.3/day from continuous collection of data over the full orbit. That is 10 times more than triggered detection rate.

Its is apparent that measurements of TGFs are limited, both by the capabilities of the detectors and by how the data are handled. A second search algorithm by *Gjesteland et al.* (2012) discovered another population of weaker RHESSI TGFs that then became the second catalog. These are shown in Figure 3.1, where the fluence of the new population is shown as the black curve and that of the first RHESSI catalog is shown as the red curve. A significant drop in TGF fluence is apparent at low counts. It is not established whether that is because all TGFs, when produced, are intense, or if it is due to instrument limitations. A more recent study showed that at least some weaker TGFs had been missed by the earlier search algorithms. In *Østgaard et al.* (2015), they superposed RHESSI data at times that was correlated with lightning discharges detected by the World Wide Lightning Location Network (WWLLN). With this method another set of weaker TGFs emerged from the RHESSI data.

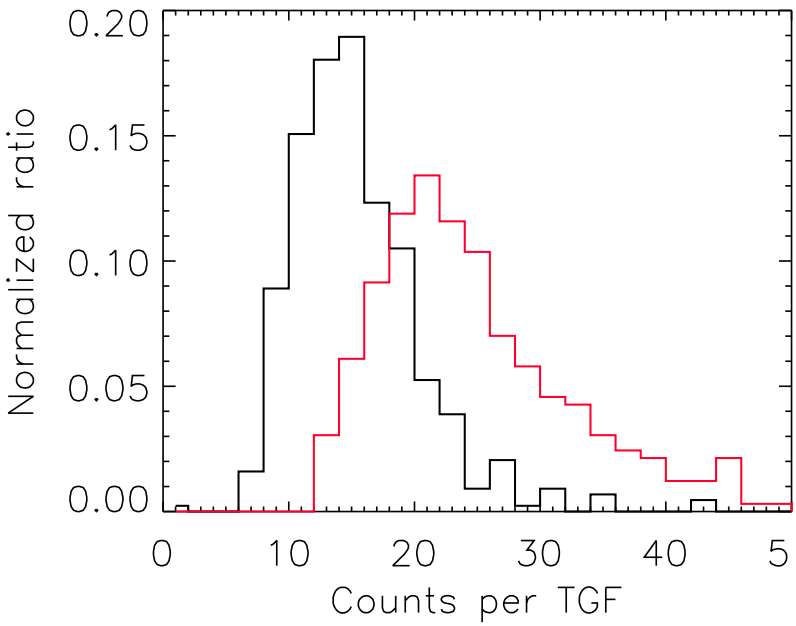

Figure 3.1: This figure shows the fluence distribution of the first RHESSI catalog of TGFs (*Grefenstette et al.*, 2009) (red) compared to the population discovered by *Gjesteland et al.* (2012) (black). It shows that the newer population is significantly weaker, but also more numerous. Taken from *Gjesteland et al.* (2012).

Østgaard et al. (2012) addressed the question: How common are TGFs? They concluded that they cannot rule out that all lightning discharges produce TGFs. However, depending on how bright the TGFs are and how deep into the atmosphere they are produced, they may not be detectable from space.

3.2 Evidence of the association between lightning and TGFs

Inan et al. (1996) were first to associate lightning generated ELF/VLF sferics to TGFs. They identified two matches between BATSE observations of TGFs and lightning strokes measured at Palmer station in Antarctica. For further comparison, WWLLN provided a list of times associated with lightning generated radio waves. Thus, the timing of TGFs detected by RHESSI and Fermi could be compared with the WWLLN time tags. RHESSI and WWLLN time tags were matched at a rate of between 3% in 2002 and 26 % in 2010 (*Collier et al.*, 2011; *Gjesteland et al.*, 2012). Roughly the same rate of correlations for the new catalog, as found for the same years for the first catalog by *Collier et al.* (2011). Fermi and WWLLN were matched for 15 out of 50 TGFs (30%) by *Connaughton et al.* (2010), also comparable to the results by the RHESSI-WWLLN association.

For some matches, a more detailed analysis has been possible. *Cummer et al.* (2005) reported on 26 RHESSI TGFs measured over the Caribbean and Americas that had been associated with lightning discharges. They used the radio waves from the magnetic field sensors at Duke University to determine the timing between the discharge of the +ICs and TGFs. 13 out of 26 sferics where seen within -3/+1 ms of the TGFs. *Shao et al.* (2010) and *Lu et al.* (2010) compared timing of TGFs with measurements of associated +IC lightnings, using lightning mapping arrays. They found evidence that TGFs are produced during the upward propagation of lightnings that discharged below 14 km altitude. These findings have been confirmed by *Cummer et al.* (2011, 2015), where better temporal resolution helped provide more detailed insight into the exact timing. *Cummer et al.* (2015) were able to show that TGFs are often produced after leaders have become roughly 1-2 km long and that these leaders continue to develop after the TGF production. Lastly, it is worth mentioning the study done by *Østgaard et al.* (2015). As opposed to previous studies, they used VLF detection of lightning by WWLLN to find RHESSI matches. They successfully found hundreds of new, weaker TGFs.

It is clear that TGFs are often associated with +IC discharges. Although not all TGFs are found to match a specific lightning stroke, they have been found to be correlated with thunderstorm activity within a few 100 km radius surrounding the satellite foot points (*Connaughton et al.*, 2010). It is uncertain whether TGFs can occur with-

out the presence of a lightning discharge, the so called “dark lightning” (*Dwyer et al.*, 2013).

3.3 Energy spectrum and source altitudes

Immediately after the discovery of TGFs, *Fishman et al.* (1994) suggested that the counts were photons consistent with a bremsstrahlung spectrum created by runaway electrons (see section 4.1 for a description of Wilsons runaway electrons). This was tested by *Lehtinen et al.* (1996), who correlated the counts obtained by BATSE measurements to an attenuated bremsstrahlung spectrum and found that these were in agreement. The collected data from the RHESSI and AGILE instruments, combined with the energy response matrix of the detectors, made it possible to derive a more detailed energy spectrum of the measured counts (*Dwyer and Smith*, 2005; *Marisaldi et al.*, 2010; *Smith et al.*, 2005). It was derived by accumulating counts from many events. These results suggests that the source is actually high energy electrons. Several atmospheric attenuation models have been developed (*Carlson et al.*, 2007; *Dwyer and Smith*, 2005; *Gjesteland et al.*, 2010; *Østgaard et al.*, 2008) and have found the production altitude to be below 21 km, which is in agreement with the upper altitudes of thunderclouds. Figure 3.2 shows the correlation by *Dwyer and Smith* (2005), between bremsstrahlung spectra of different source altitudes and the RHESSI spectrum.

As discussed above, TGFs have been associated with radio signals generated by lightning discharges (*Inan et al.*, 1996). In particular, a close relationship between TGFs and +IC lightning, which develop in a stepped manner transporting electrons from the MN charge layer toward the UP charge layer, has been reported (*Cummer et al.*, 2005, 2011, 2015; *Lu et al.*, 2010; *Østgaard et al.*, 2013; *Shao et al.*, 2010; *Stanley et al.*, 2006). These measurements suggest that the typical production altitude is actually inside thunderclouds, between 10 km and 15 km altitude. *Dwyer and Smith* (2005) also found that a source of electrons that is emitted isotropically in a cone with half angle of 45° would lead to a significant lowering of the matched spectrum, approximately 15 km. The flux of source electrons would then be $\sim 2 \times 10^{17}$.

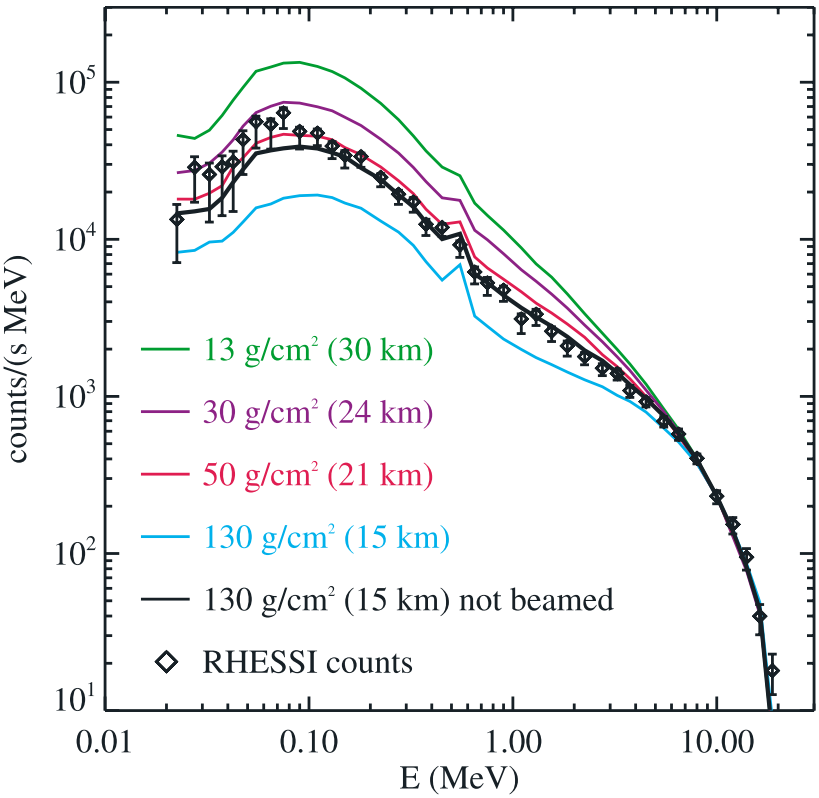

Figure 3.2: The energy spectrum of superposed RHESSI counts, matched to energy spectra produced by RREAs and attenuated from different source altitudes. Taken from *Dwyer and Smith* (2005).

3.4 Maximum energy

The BATSE satellite could not distinguish between photons of a few 100 keV and much higher energies, while the RHESSI instrument is limited to a maximum energy of 20 MeV (*Smith et al.*, 2005). The AGILE detector, however, cover energies up to GeVs and may therefore be better suited to measure the maximum energies of TGFs. *Marisaldi et al.* (2010) reported maximum energies between roughly 5 MeV and 43 MeV, which is generally referred to as the maximum energy. Another AGILE study was reported in *Tavani et al.* (2011), which claimed to see TGF photons with energy up to 100 MeV. However, the energy spectrum associated with these very high energy observations does not follow the exponential cut off associated with the typical relativistic electron energy spectrum, but instead a power law at the highest energies. *Celestin et al.* (2012) was able to reproduce this type of spectrum assuming that the relativistic electrons were accelerated in nonuniform and extremely strong electric fields with a peak at roughly 60 times the conventional breakdown threshold. In *Celestin and Pasko* (2011) they show

how the initial development of the electron population is a highly transient process that may follow a power law energy distribution before it reaches the exponential cut-off associated with a steady state. We will refer to the results in *Marisaldi et al.* (2010) of roughly 40 MeV.

Chapter 4

The production of TGFs

Several scenarios have been presented to explain the production of TGFs. However, none of the scenarios can convincingly explain the observations when realistic constraints are introduced.

In this chapter, we introduce the concept of how Wilson's runaway electrons are accelerated and multiplied through the RREA mechanism. In the final section, we will present the two leading production scenarios. They shall be referred to by their inherent electric field: 1) The ambient field scenario. 2) The streamer-leader field scenario. Emphasis will be put on understanding the physical concepts, such that differences between the scenarios become transparent and weaknesses and strengths can be identified.

4.1 Runaway electrons

As mentioned previously, at any moment in time there is roughly 10 free electrons per cm^{-3} at sea level. Most commonly they are secondary electrons from cosmic ray particles (see Section 4.3.1 for more details) or less commonly the product of radioactive decay from radon in the Earth itself. As Wilson discovered, when these free electrons of sufficient energy are accelerated, the experienced friction force decreases (*Wilson*, 1924). The friction force experienced by relativistic electrons is mainly due to inelastic collisions with air molecules at energies below ~ 1 MeV, and due to bremsstrahlung emission above ~ 1 MeV. The friction force is shown in Figure 4.1 for electrons in air at sea-level density and pressure. The horizontal lines indicate electric field strengths that correspond to various electrical breakdown processes. On average, the energy gained by runaway electrons, $d\varepsilon$, over a distance, dz, in an electric field, E, larger than the friction force, F_d, can be expressed as

$$d\varepsilon = (F_d - eE)dz. \tag{4.1}$$

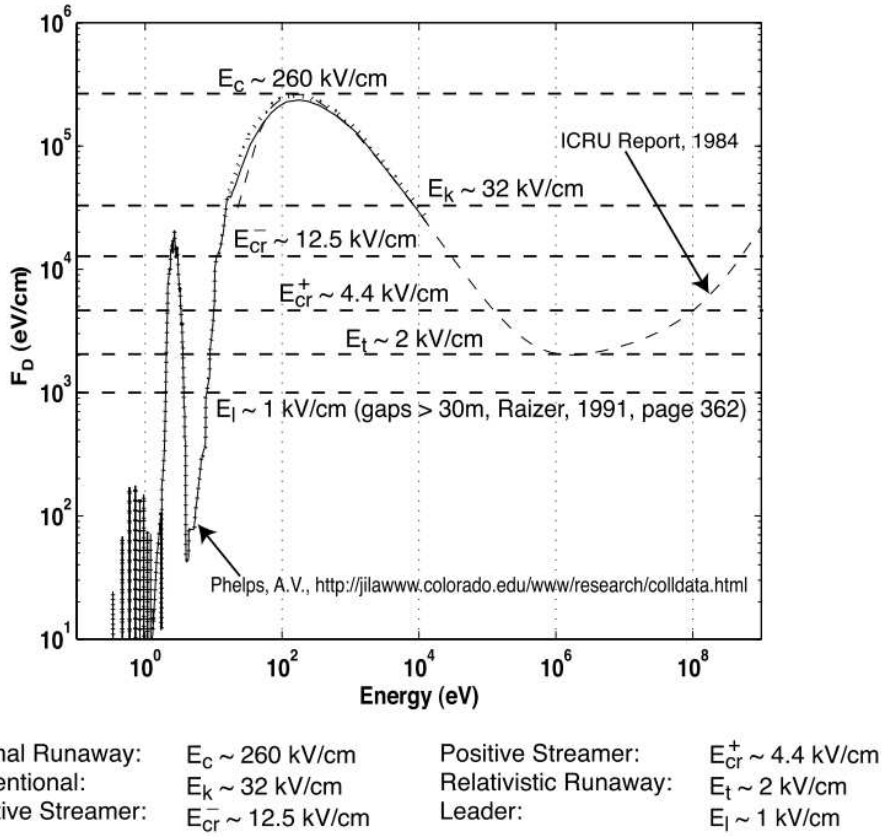

Figure 4.1: Friction force in air at sea-level density and pressure. Taken from *Moss et al.* (2006)

In Section 2.2.1 we introduced the conventional breakdown threshold, $E_k = 32$ kV/cm at sea level. It is the threshold field strength required to accelerate low energy electrons enough to ionize the oxygen and nitrogen atoms, and hence create a breakdown. In order to accelerate the electrons to become runaway, a much stronger electric field is required. As can be seen in Figure 4.1, the maximum friction force is experienced when the electrons have reached energies of roughly 100 eV. At this energy, the friction force can be balanced by an electric field strength of $E_c \sim 260$ kV/cm, which is the thermal runaway threshold. The mechanism of accelerating low energy electrons to runaway energies (> 10 keV, see the next paragraph) is often referred to as thermal acceleration, reflecting the initial energy of the free electrons. One of the few places where such strong electric fields may occur naturally is in the very local region in the tips of streamers propagating in the strong electric fields created by lightning leaders (*Celestin and Pasko*, 2011; *Chanrion and Neubert*, 2010; *Moss et al.*, 2006). *Cooray et al.* (2009) also suggested that the electric field between colliding streamers may become sufficiently strong. However, modeling results have indicated that ionization between the streamers will quench the electric field on a timescale of a few ps (*Ihaddadene and Celestin*, 2015; *Köhn et al.*, 2017a). In *Ihaddadene and Celestin* (2015), a fluid model

approach was used to determine the evolving electron density, and from that the electric field. They found that the electric field was insufficient to overcome E_c. *Köhn et al.* (2017a) used a self consistent particle in cell approach that continuously updates particle movement and electric field. Although the resulting electric field exceeded E_c, the extent and lifetime of the electric field between the streamers was insufficient to produce electrons with energies above 700 eV. As will be described in the following paragraph, that is less than the 10s of keV required for the electrons to be runaway.

Thermal acceleration requires an electric field strength stronger than 260 kV/cm. However, electrons with energy in the keV to MeV regime, such as secondary particles from cosmic rays, experience a decreasing friction force with increasing energy. Thus, these electrons can be runaway in much weaker electric field strengths. At electric field strengths close to E_k, which can exists for several tens of ns to μs over cm to meter scale, the energy of the electrons must be larger than 10 keV. The minimum electric field strength required to sustain the runaway electrons is the relativistic runaway threshold, $E_t \sim 2$ kV/cm, which is experienced by electrons with an energy of ~ 1 MeV. Electric fields close to E_t can exists for longer periods of time over several 100s of meters.

4.2 Relativistic runaway electron avalanches

Several attempts were made to confirm the existence of the runaway electrons proposed by Wilson (see *Parks et al.* (1981) and references therein). However, the strong friction force that act on the electrons make them short ranged and difficult to measure directly. In search for evidence of the runaway electrons, a NASA-aircraft mission was launched. The aircraft carried x-ray detectors to look for the much longer ranged x-ray emissions that must be produced if the high energy electrons are present (*Parks et al.*, 1981). This first flight confirmed the existence of up to at least 12 keV photons *Parks et al.* (1981). Further flight missions were conducted, and significant fluxes of bremsstrahlung photons with energies >115 keV that lasted for up to a few seconds, were detected (*Mccarthy and Parks*, 1985). *Mccarthy and Parks* (1985) concluded that these were consistent with emissions from runaway electrons, and that the electric fields inside thunderclouds could be responsible for accelerating the electrons. However, the flux of runaway electrons created by cosmic rays was calculated to be insufficient to explain the intensity of the emissions.

The results from *Mccarthy and Parks* (1985) prompted the search for an alternative mechanism. *Gurevich et al.* (1992) then showed that if one consider elastic scattering on atomic electrons (Møller scattering) an exponential increase of the runaway electrons will occur if the electric field is sufficiently strong. This is the multiplication

mechanism referred to as a RREA. *Dwyer* (2003) found that, as the scattering of the electrons with both atomic nuclei and atomic electrons cause the electrons to propagate out of alignment of the electric field, the minimum electric field strength required to sustain RREAs is

$$E_{RREA} = 2.84 \text{ kV/cm}, \tag{4.2}$$

30 % larger than the relativistic runaway threshold.

Not only Møller scattering contributes to the multiplication of runaway electrons. The electrons also interact with the field of nuclei, which emits bremsstrahlung photons. These will produce secondary electrons through photoelectric absorption and Compton scattering, and both electrons and positrons through pair-production. *Köhn and Ebert* (2015) also showed that elastic collisions between neutrons and electrons will contribute. The majority of the secondary electrons are of course low-energy. *Dwyer and Babich* (2011) found that the rate of ionization per runaway electron is between 6900 and 8350 per meter. Although they will not be accelerated to higher energies, they can create measurable currents and will increase the local conductivity.

Simulations with Monte Carlo models, that take some or all of these interactions into account, have been performed to determine the rate of multiplication (*Babich et al.*, 1998, 2001; *Babich*, 2005; *Celestin and Pasko*, 2011; *Coleman and Dwyer*, 2006; *Dwyer*, 2003; *Köhn and Ebert*, 2015; *Lehtinen et al.*, 1999; *Skeltved et al.*, 2014). The result is often represented in terms of the avalanche (e-folding) length, λ. *Dwyer et al.* (2012) presented a detailed comparison of avalanche rate obtained by some of these models, which can approximately be represented by

$$\lambda(E) \approx \frac{7.3 \text{ MeV}}{eE - F_d}, \quad 3 \leq E \leq 30 \text{ kV/cm} \tag{4.3}$$

where $F_d = 0.276$ MeV/m is approximately equal to the average energy loss experienced by minimum ionizing electrons (*Coleman and Dwyer*, 2006; *Dwyer*, 2003). The total number of runaway electrons, N_{RE}, can be estimated as a function of the number of initial seed electrons, N_0, distance, z and the electric field dependent avalanche length, $\lambda(E)$,

$$N_{RE} = N_0 \exp\left(\frac{z}{\lambda(E)}\right). \tag{4.4}$$

The energy spectrum of RREAs is another important feature that has been identified from modeling results. In Paper III (*Skeltved et al.*, 2017), using the energy spectrum and electric field thresholds presented in *Dwyer et al.* (2012) and *Celestin et al.* (2015), we argued that the RREA must develop over a minimum of $\sim$3.5 avalanche lengths to reach steady state and thereby reach the characteristic energy spectrum, which is given

as

$$f_{RE} = \frac{dN(\varepsilon)}{d\varepsilon} = \frac{N_{RREA}}{7.3\ \text{MeV}} \exp\left(-\frac{\varepsilon}{7.3\ \text{MeV}}\right) \tag{4.5}$$

To derive the avalanche length (Equation 4.4) and the corresponding energy spectrum (Equation 4.5, from Equations. 4.4 and 4.1) we refer to Appendix A in Paper I (*Skeltved et al.*, 2014). The comparison from *Dwyer* (2012), is shown in Figure 4.2.

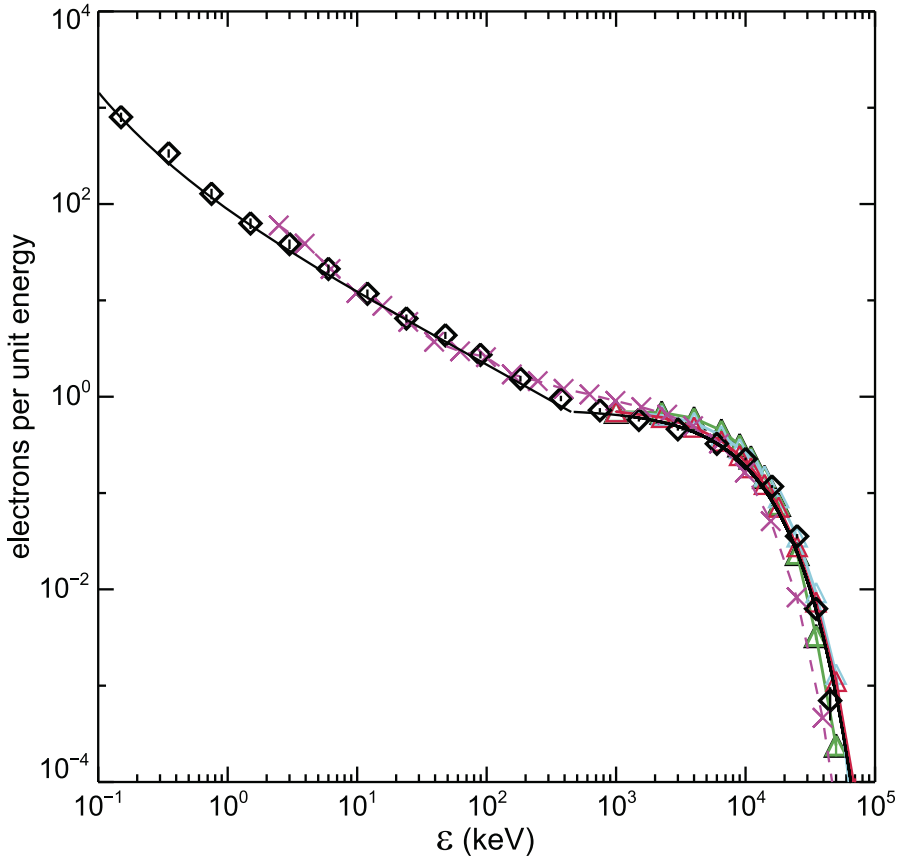

Figure 4.2: The RREA energy spectrum shows the characteristic 7.3 MeV cut-off at energies above roughly 300 keV and a power law at lower energies. This is illustrated by comparison of the independent models reported in *Celestin and Pasko* (2011) (crosses) and *Dwyer and Babich* (2011) (diamonds), and for electric field strengths 400 kV/cm, 750 kV/cm and 2000 kV/cm (triangles) using the custom model first presented in *Dwyer* (2003). The Figure is taken from *Dwyer et al.* (2012).

The models used in *Gurevich et al.* (1992), *Lehtinen et al.* (1999), *Dwyer* (2003), *Celestin and Pasko* (2010) and in Paper I *Skeltved et al.* (2014) simulate RREAs in uniform electric fields, while *Babich et al.* (1998) considers both uniform and non-uniform fields. The simulations performed in *Celestin et al.* (2012, 2015); *Xu et al.* (2012) use the same model as *Celestin and Pasko* (2010), but expanded to include non-uniform electric fields. It is interesting to note, that multiplication of runaway electrons

is independent of electric field configuration. The primary difference is the number of initial particles and the rate of multiplication with time and distance. Accordingly, the exponent of Equation 4.4 can be integrated to take into account a non-uniform electric field within the boundaries, z_1 and z_2 of the electric field region

$$N_{RE} = N_o \exp\left(\int_{z_1}^{z_2} \frac{dz}{\lambda(E(z))}\right), \tag{4.6}$$

as we showed in Paper III (*Skeltved et al.*, 2017).

4.3 The two leading production scenarios

It is established that the production of TGFs occur inside thunderclouds at altitudes below roughly 15 km and often at times closely associated with the development of +IC discharges. The energies of the detected photons have been measured to be in the MeV range up to at least 43 MeV. To find the spectrum at the source of TGFs, bremsstrahlung production and attenuation models have been used. It has been inferred from these models, that a source of $\sim 10^{16} - 10^{17}$ electrons following the typical energy distribution of RREAs with an exponential cut off of 7.3 MeV, and a maximum energy that is higher than the maximum photon energy, is required.

In the previous section, we discussed x-ray measurements above thunderclouds. To explain these measurements, *Gurevich et al.* (1992) presented the RREA multiplication mechanism. The energy distribution of the source electrons of TGFs are consistent with RREA multiplication. The maximum energy of the electrons depends on the available electric potential in the production region. However, RREAs initiated by cosmic ray secondary particles alone cannot explain the much higher intensities associated with the production of TGFs. Thus, another source of seed electrons, or multiplication is required.

The objective of the production scenarios is to explain this gap: How can such high intensities and energies be produced naturally in the Earth's atmosphere?

4.3.1 Acceleration and multiplication of electrons in the ambient electric field

In this scenario, one assumes that the acceleration and multiplication of runaway electrons occurs in the ambient electric field of a thundercloud. Two different configurations of the ambient electric field will be discussed. A vertically uniform electric field and an ambient electric modified by an extensively branched lightning discharge.

Generally, the scenario assumes three stages of acceleration and multiplication: 1) An initial flux of 1 MeV seeding electrons, often assumed to be the result of secondary

particles from cosmic rays and extensive air showers. However, it is not exclusive of any seeding mechanism. 2) Multiplication of these through RREAs. 3) A multiplication of RREAs through the relativistic feedback mechanism *Dwyer* (2003).

Cosmic ray secondary particles as seeding for RREAs

High energy radiation that is produced outside the solar system is typically called cosmic rays. When they enter the Earths atmosphere, these primary particles produce large numbers of secondary particles in what is called an extensive air shower. The cosmic ray primary particles are extremely energetic and are distributed in energy up to at least 20^{20} eV, falling as roughly

$$\frac{dN_p}{d\varepsilon} \propto \frac{1}{\varepsilon^3}, \tag{4.7}$$

where N_p is the number of primaries and ε is their energy (*Carlson et al.*, 2008). The primary particles penetrate far into the atmosphere before extensive air showers are initiated, with the highest energies penetrating farthest. It is then interesting to know the number of seeding particles per unit in time that enters a region with sufficient electric field. *Carlson et al.* (2008) used Monte Carlo simulations to investigate this question. They found that primary particles with energies between 10^9 eV and 10^{15} eV, where the most likely candidates.

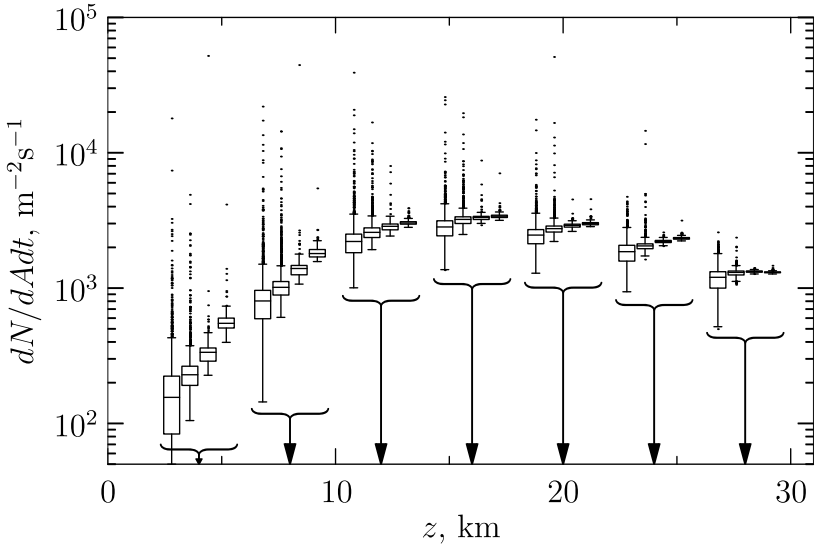

Figure 4.3: The flux of seeding electrons as a function of altitudes that may be considered source TGFs. The results are estimated for the altitudes indicated by brackets and arrows, for four different combinations of areas and times from left to right (radius/time) 100m / 0.3μs, 300m / 1μs, 1km / 3μs, 3km / 10μs. This figure is taken from *Carlson et al.* (2008).

The results showed that although, directionality, particle type and energy plays a role, one can expect RREAs to be initiated within 1 μs. The altitude that gives the highest average density of seed electrons was found to correspond well with the source altitude of TGFs, between 13-20 km. In Figure 4.3, we show the flux of seed electrons as a function of altitude.

Relativistic feedback

It is customary to assume that a sufficient flux of 1 MeV seed electrons have entered a region with electric field strength above the RREA threshold, $E_{RREA} = 2.84$ kV/cm. A rough estimate of the multiplication due to RREAs then requires an assumption of the strength of the electric field and its vertical extent (electric potential). Considering a typical large thunderstorm, it is reasonable to assume a potential difference between the main charge layers of up to 150 MV (*Marshall and Stolzenburg*, 2001). An electric field that is 2 times the RREA threshold then gives a vertical extension of roughly 250 m. That corresponds to between 10 and 11 avalanche lengths (Eq. 4.3), or a multiplication of between 10^4 and 10^5. Furthermore, it is also reasonable to assume roughly 10^3 seed electrons to be present pr. $\mathrm{km}^{-2}\mu\mathrm{s}^{-1}$ (*Carlson et al.*, 2008). It is clear, that to explain the 10^{16} to 10^{17} source electrons that is required to produce the measured TGFs, this estimate falls many orders of magnitude short.

Dwyer (2003) was first to test the effect of collisions between atomic electrons and backward propagating positrons (Bhabha scattering), and backward scattering photons. To differentiate this high energy case from the low energy feedback that occurs in Townsend gas discharges, they called this the relativistic feedback discharge (*Dwyer*, 2012). To quantify the effect, they introduced the feedback factor γ, which is the ratio between one generation of RREAs and the number of RREAs produced by feedback from that generation (*Dwyer*, 2003). The time it takes a photon to propagate from the start of the avalanche region to its end, and back again is one feedback cycle $t_{fb} = L/c$, where L is the total length of the avalanche region. The feedback factor can be derived as the common ratio of a geometric series (see Appendix C in Paper I (*Skeltved et al.*, 2014)), which in its general from can be added to Equation 4.4 by

$$N_{RE} = N_0 \left(\frac{1 - \gamma^{(t/t_{fb})}}{1 - \gamma} \right) \exp\left(\frac{z}{\lambda(E)} \right), \quad \text{for} \quad \gamma \neq 0, \tag{4.8}$$

where t is time and t_{fb} is the duration of a single feedback cycle.

When $\gamma < 1$, the number of electrons that is produced due to RREAs, increases by

a simple multiplicative factor and Equation 4.8 becomes

$$N_{RE} = N_0 \frac{1}{1-\gamma} \exp\left(\frac{z}{\lambda(E)}\right), \quad \text{for} \quad \gamma < 1, \tag{4.9}$$

but still relies on a steady supply of seeding electrons in order to be sustained. Note that although $\gamma < 1$, the number of electrons will be significantly increased as $\gamma \to 1$, compared to RREA multiplication on its own. The significant number of low energy secondaries produced as $\gamma \to 1$, may cause a discharge or partial discharge by itself (*Dwyer*, 2012).

For the case of $\gamma = 1$, the feedback factor is expressed in terms of the number of feedback cycles it has undergone. Equation 4.8 then becomes

$$N_{RE} = N_0 \frac{t}{t_{fb}} \exp\left(\frac{z}{\lambda(E)}\right), \quad \text{for} \quad \gamma = 1, \tag{4.10}$$

where t is time and t_{fb} is the length of one feedback cycle.

If $\gamma > 1$, the number of RREAs will increase exponentially with each feedback cycle. Figure 4.4 shows the evolution from a single RREA in the top panel to multiple RREAs, that are the results of feedback, in the middle and lower panel. The number of RREAs produced by the ambient flux of seed electrons quickly becomes negligible compared to the effect of feedback. Equation 4.4 now becomes

$$N_{RE} = N_0 \gamma^{\,t/t_{fb}} \exp\left(\frac{z}{\lambda(E)}\right), \tag{4.11}$$

for large values of n.

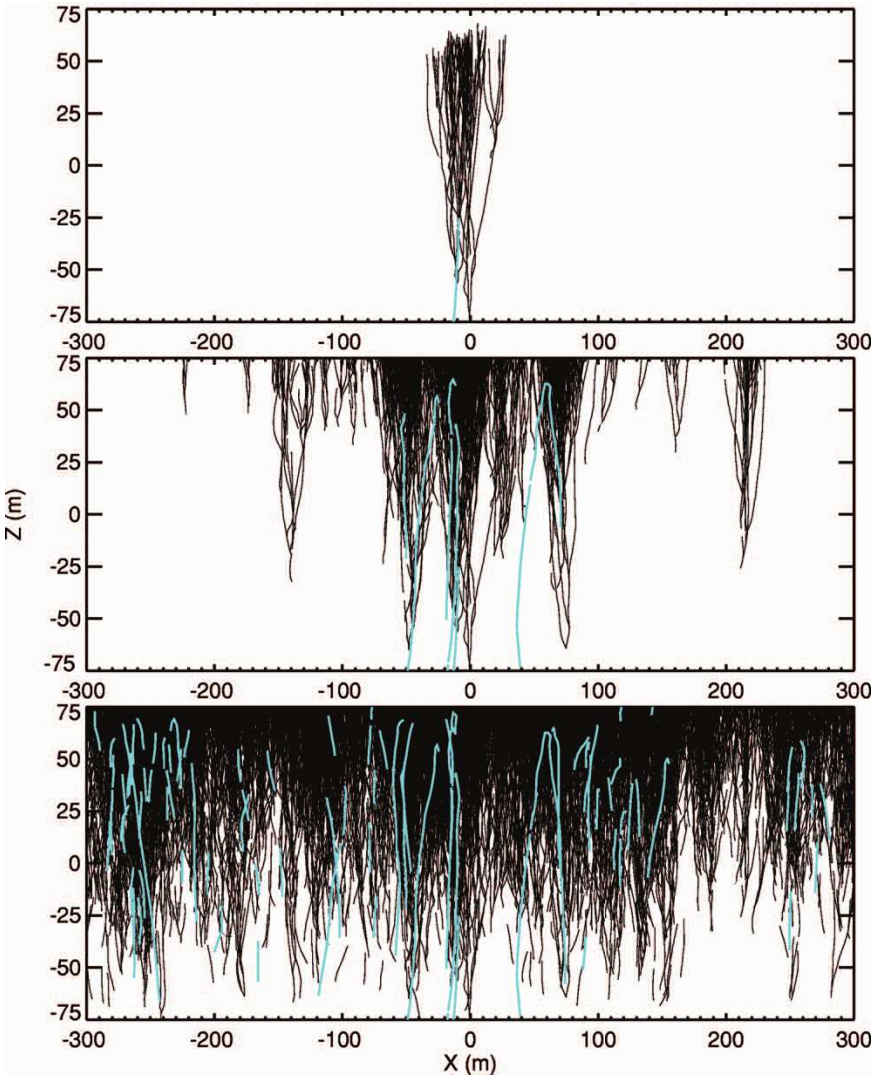

Figure 4.4: Track of electrons (black lines) in a RREA in the upper panel, and the feedback by photons and positrons (blue lines) with the following initiation of new RREAs in the middle and lower panels. It can all start from a single seed electron. Taken from *Dwyer* (2007).

The feedback factor depends on a combination of the electric field strength and its extension in the direction of the avalanches. *Dwyer* (2003) used a custom Monte Carlo model to estimate what combination of field strength and extension that is required in order to have $\gamma = 1$. In Paper I (*Skeltved et al.*, 2014), we tested their results, using the open source Geant 4 modeling toolkit. We found that the results were in good agreement with *Dwyer* (2003). In Figure 4.5, we use the results from Paper I (*Skeltved et al.*, 2014), to present the requirements for $\gamma = 1$. The two panels show the required combination of field strength and potential on the left (sea level), and fraction of E/E_{RREA} and vertical extension at 12 km altitude on the right.

In-situ measurements of electric fields in thunderclouds are most often performed

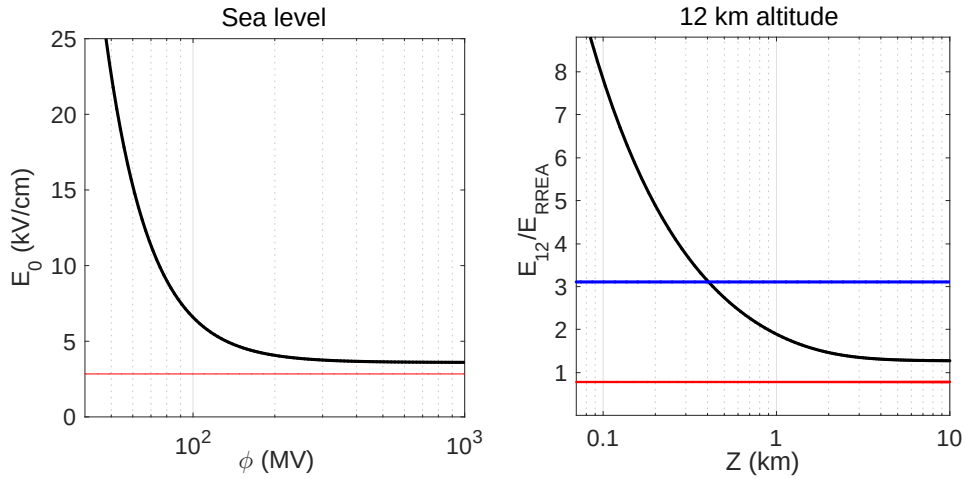

Figure 4.5: Conditions for the RFD to be self sustained, $\gamma = 1$. The required combination of electric field strength and potential (sea level equivalent) on the left. On the right, the combination of the ratio E_{12}/E_{RREA} and vertical extension at 12 km altitude is shown. The RREA threshold is shown as the red line in both panels, and the peak field strength reported by *Stolzenburg et al.* (2007) is indicated as the blue line in the right panel.

from balloons. Compared to the electric field changes in the cloud, the balloons rise slowly. However, they may provide an estimate of typical electric field strengths and extents, and thereby also potential differences between charge regions. *Stolzenburg et al.* (2007) reported several such ascents. The red lines in Figure 4.5, indicate the RREA threshold E_{RREA} at sea-level in the left panel and at 12 km altitude in the right. The blue line in the right panel, correspond to the maximum electric field measurement reported in *Stolzenburg et al.* (2007), 2 kV/cm $\sim 3E_{RREA}$, which incidentally was followed by a discharge after roughly 15s. Note that this electric field must be extended over roughly 400m, in the direction of the avalanche, in order for $\gamma > 1$.

From Figure 4.5, one can also see that the electric field must be a minimum of $\sim 1.25E_{RREA}$, for $\gamma > 1$, and that close to this limit, the requirement for vertical extension quickly becomes on the order of several km. More commonly, electric field measurements are reported to be below the RREA threshold. If relativistic feedback is important it is likely to be during large thunderstorms and under optimal conditions.

Possible association between RFDs and +IC lightning

In the previous section, we presented a scenario in which TGF production may occur when the ambient electric field and its extension increases enough to push the feedback factor γ above 1. This would indicate that TGFs could be produced also without association to lightning discharges *Dwyer* (2012). Another scenario was presented in *Dwyer* (2012), where the change in conductivity and thereby charge distribution in a region surrounding a developing +IC leader is taken into account. A simple visualization of

the two models is presented in Figure 4.6, where the ambient field scenario is shown without a leader discharge on the left and with on the right. The scenario on the right, il-

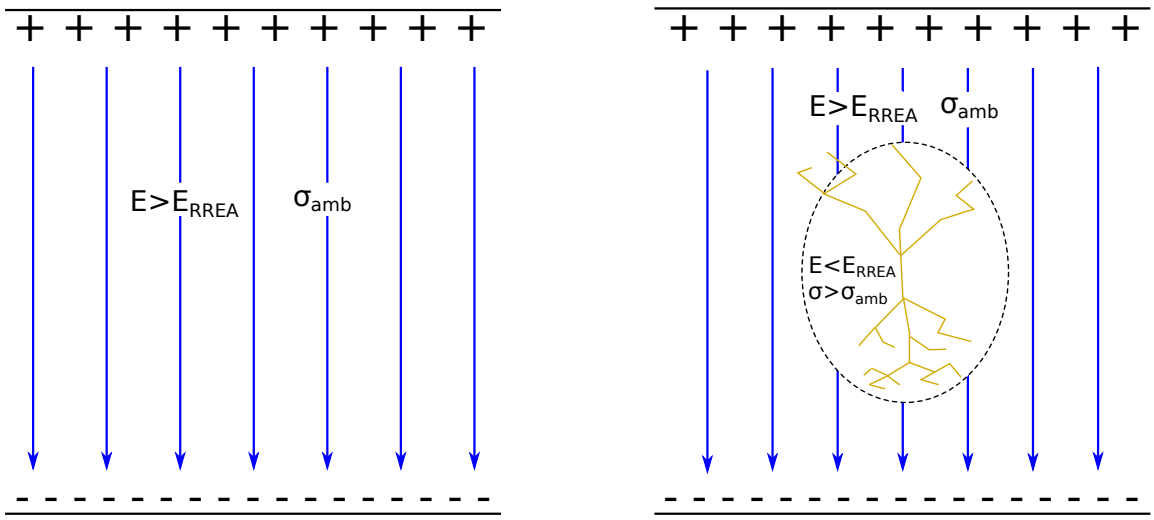

Figure 4.6: A visualization of two different scenarios that have been proposed where the feedback factor can be pushed above 1 in a thundercloud. The ambient field without the influence of a leader is shown on the left. On the right, the conductivity and charge distribution is modified in a discharge region created by a propagating leader. The ambient electric field near the boundaries of this region is then sufficiently increased.

lustrates a lightning leader with extensive branching that leads to a significant increase in the conductivity in a region surrounding the leader channels, the discharge region (*Dwyer*, 2012). In both scenarios, the area is on the order of a km^2 and the extension of the electric field is between a few 100m to km scale. With increased conductivity, the distribution of charges inside the discharge region changes and the electric field ahead of its boundaries increases. The increase in electric field and thereby electric potential outside the discharge region may then become sufficient to push the feedback factor above 1. For the scenarios to be efficient, *Dwyer* (2012) showed that the relativistic feedback discharges must develop over a potential difference of 200-400 MV. This was also highlighted in Paper I (*Skeltved et al.*, 2014).

4.3.2 Acceleration and multiplication of electrons in the electric field of streamers and lightning leaders

This scenario is typically described as consisting of two stages of multiplication: 1) The production of seed electrons at the tips of streamers (*Celestin and Pasko*, 2011; *Chanrion and Neubert*, 2010; *Moss et al.*, 2006). 2) The continued multiplication and acceleration of these, through RREAs, in the electric field created by the leader (*Celestin et al.*, 2012; *Köhn and Ebert*, 2015; *Köhn et al.*, 2017b; *Moss et al.*, 2006; *Skeltved*

et al., 2017; *Xu et al.*, 2012). Although relativistic feedback is not considered crucial for this scenario, the contribution may be noticeable (*Köhn et al.*, 2017b).

Acceleration of electrons in the tips of streamers

It was proposed by *Moss et al.* (2006), that acceleration of low energy electrons to runaway energies (thermal acceleration) could occur in the electric field created in the tips of propagating streamers. That requires a strength of more than the thermal runaway threshold $E_c \sim 8E_k$ (see Figure 4.1). As was emphasized in Section 4.1, the thermal runaway threshold, $E_c = 260$ kV/cm, can only exist on a time scale of less than a few ps at sea level (*Ihaddadene and Celestin*, 2015; *Köhn et al.*, 2017a; *Liu and Pasko*, 2004).

Monte Carlo models have been used to investigate under which circumstances electric fields stronger than E_c may exist in the tips of streamers (*Celestin and Pasko*, 2011; *Moss et al.*, 2006). They found that one such circumstance is when streamers propagate in electric fields stronger than the conventional breakdown threshold, $E_k = 32$ kV/cm. *Celestin and Pasko* (2011); *Moss et al.* (2006) modeled the propagation of a streamer immersed in the electric field ahead of a lightning leader, where the leader field strength was chosen to be $1.5E_k$. This field strength was given in (*Bazelyan and Raizer*, 2000, p. 68) who argues that this is a realistic maximum field strength. It is reasonable to assume that such field strengths exists, since a developing +IC leader is preceded by a conical streamer zone. Thus, the field strength must be sufficient to initiate and sustain streamer development. The threshold for a streamer to become self sustained is ~ 12.5 kV/cm for a negative and ~ 4.4 kV/cm for a positive streamer (sea level equivalent). The results have show that in an electric field of $1.5E_k$, the streamer become faster and the radius will undergo exponential growth (*Celestin and Pasko*, 2011; *Liu and Pasko*, 2004; *Moss et al.*, 2006). The electric field was then shown to reach values of up to $10E_k$, just prior to branching, which is larger than the thermal acceleration threshold, $E_c \approx 8E_k$.

An important mechanism for streamer development is photoionization ahead of the streamer tip, so called preionization. The preionization relies on the excitation and ionization of O_2 and N_2 molecules, which then emits UV photons that can travel ahead of the developing streamer. Models have shown that the primary source of ionization is the very thin region, where the electric field is near its peak, inside the streamer head (*Celestin and Pasko*, 2011; *Liu and Pasko*, 2004). Figure 4.7 shows a cross sectional view of a streamer, where the electron density is shown on the left and the electric field is shown on the right. This figure clearly illustrates the exponential growth and the very thin region with peak electric field strength (*Celestin and Pasko*, 2011). If sufficient preionization occurs, electrons are supplied to the streamer tip which then allows it to

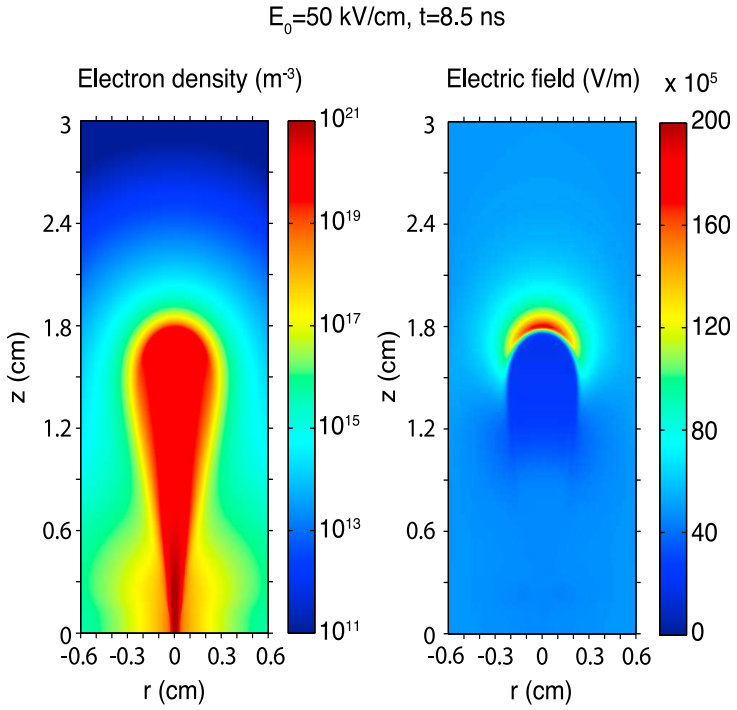

Figure 4.7: A cross sectional view of a streamer propagating in an electric field of $1.5E_k = 50$ kV/cm after 8.5 ns. The electron density is shown on the left and the electric field is shown on the right. Notice the very thin region with peak electric field. This figure is taken from *Celestin and Pasko* (2011).

continue to propagate and grow. The modeling results have shown that the radius of the streamer may eventually become greater than the characteristic absorption length of UV photons (*Liu and Pasko*, 2004). When this happens, the rate of preionization ahead of the streamer tip becomes smaller and thereby halts its propagation. The streamer compensates by increasing its electric field to values up $10E_k$ (*Celestin and Pasko*, 2011; *Liu and Pasko*, 2004; *Moss et al.*, 2006). Eventually branching will occur. This may be crucial for the production of seed electrons. *Moss et al.* (2006) showed that just prior to the branching of a streamer a significant flux of electrons between 2-8 keV were produced. *Celestin and Pasko* (2011) later found that the energies of the accelerated electrons may be closer to an average of ~ 65 keV and that roughly 1/100 low energy electrons become runaway.

The total number of seed electrons can be estimated by assuming the number of streamers and the number of electrons in each streamer. Based on the exponential growth of streamer radius and total charge in streamer head, the number of electrons was estimated to be up to 10^{10} by *Celestin and Pasko* (2011). The number of streamers in the streamer zone ahead of the leader can be assumed to be

$$N_s = Q_s/q_s, \tag{4.12}$$

where Q_s is the total charge in the streamer zone, and q_s is the charge carried by each streamer (*Bazelyan and Raizer*, 2000, p. 70). Q_s can be approximated by

$$Q_s = \pi \varepsilon_0 R_{sz} \Delta\phi_{tip}, \tag{4.13}$$

where R_{sz} is the radius of the streamer zone and $\Delta\phi_{tip}$ is expressed in Equation 2.2. q_s is generally on the order of 1 nC (*Bazelyan and Raizer*, 2000, p. 69-71). Leading to a total number of streamers of $\sim 10^6$ and thereby a total number of seed electrons of up to 10^{16}.

RREA multiplication in electric fields created ahead of +IC leaders

Moss et al. (2006) also proposed that further acceleration of these seed electrons can occur in the weaker, but spatially more extended leader electric field. One may then consider the instant just after a negative leader step have been completed. At that moment in time, it is reasonable to assume that a corona discharge occurs, and that the charges on the new segment have been redistributed and all the potential has been transferred to the new tip (*Celestin and Pasko*, 2011; *Celestin et al.*, 2012, 2015; *Köhn and Ebert*, 2015; *Köhn et al.*, 2017b; *Skeltved et al.*, 2017; *Xu et al.*, 2012).

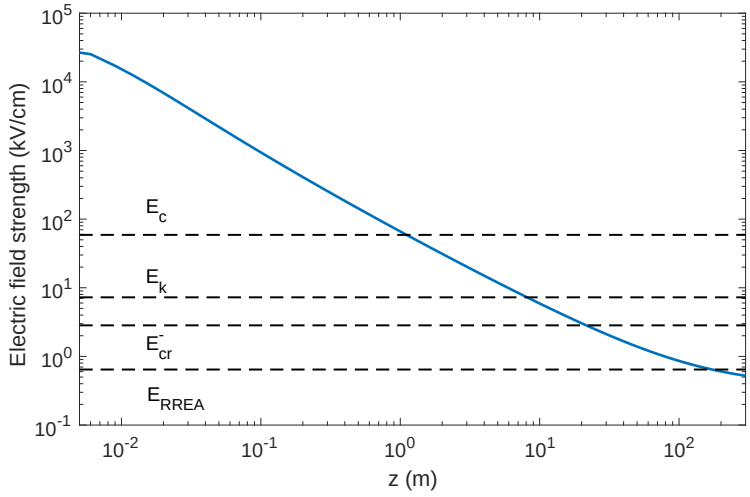

Figure 4.8: The electric field ahead of a leader channel of 5 km length immersed in an ambient electric field of 0.4 kV/cm. The dashed lines shows, from top to bottom, the thermal runaway threshold $E_c = 260$ kV/cm, the conventional breakdown threshold $E_k = 32$ kV/cm, the critical field for negative streamers to propagate $E_{cr}^- = 12.5$ kV/cm and the RREA threshold $E_{RREA} = 2.84$ kV/cm, scaled to 12 km altitude.

In this scenario, the leader is approximated as a perfectly conducting channel immersed in an ambient electric field and the potential at the tip can be expressed as in

Equation 2.2. We have calculated the leader electric field using the stable method of moments (see Appendix A of Paper III (*Skeltved et al.*, 2017)). The leader is assumed to be a capped cylinder with 5 km length, a radius of 4 cm immersed in an ambient electric field of 0.4 kV/cm, with the negative tip located at 12 km altitude. The resulting electric field is then strongly nonuniform, with field strengths 10s to 100s times the conventional breakdown threshold close to the leader tip, see Figure 4.8. A short description of different electric field models will be given in section 5.1. Without any constraints, it follows that the potential increase on the new tip has been transferred instantaneously. That is of course not physical. The time associated with the potential transfer, although not known, will allow a streamer zone to develop to some distance ahead of the new leader tip. The ionization and change in conductivity in the streamer zone will screen the electric field. To approximate the screening effects, a maximum electric field strength is typically introduced. This maximum limit varies between different models and is listed in Table 4.1. The first two models have used the a conservative upper limit, which is based on arguments first presented in *Bazelyan and Raizer* (2000), while the last three models have assumed extreme upper limits. An important consequence of approximating the streamer zone by an upper limit to the electric field, is that the screened electric field that would otherwise be displaced, is not accounted for. In Paper III (*Skeltved et al.*, 2017), we showed that between roughly $\sim 25-75\%$ of the leader potential is then "lost", depending on the chosen electric field limit.

Study	$E_{\mathbf{max}}$
Celestin and Pasko (2011)	$1.5 \times E_k$
Celestin et al. (2015)	$1.5 \times E_k$
Skeltved et al. (2017)	$1.5 \times E_k$
Xu et al. (2012)	$8 \times E_k$
Celestin et al. (2012)	$60 \times E_k$
Köhn and Ebert (2015); *Köhn et al.* (2017b)	$74 \times E_k$

Table 4.1: The maximum electric field strength introduced to approximate the effect of screening ahead of the leader tip. Note that the upper limit of $1.5E_k$ was based on the arguments first presented in *Bazelyan and Raizer* (2000).

With the limitations of the assumptions, the effects of the leader electric field on the seed electrons, can be estimated. These are most commonly assumed to be 65 keV electrons that are initiated at the position that corresponds to the distance where the electric field (i.e. Figure 4.8) drops below the maximum limit. Further multiplication

and acceleration then occur in the electric field created by the leader. This is illustrated in Figure 4.9.

The choice of different maximum electric field thresholds leads to different results. In Paper III (*Skeltved et al.*, 2017), we found that to obtain the characteristic ~ 7.3 MeV cut off in the electron energy spectrum, a potential drop between the tips of the leader of at least 300 MV is required. That was consistent with the results of *Celestin et al.* (2015). We also found that more than 400 MV is required to explain the maximum photon energy of 43 MeV (see Paper III (*Skeltved et al.*, 2017)). *Xu et al.* (2012) chose an electric field limit close to the thermal runaway threshold ($E_c \approx 8E_k$) and could reproduce observations with an assumed potential difference of 200 MV. In *Celestin et al.* (2012), *Köhn and Ebert* (2015) and *Köhn et al.* (2017b), the electrons were initiated in regions of electric field strength a factor of $\sim$10 larger than the thermal runaway threshold. With that assumption, acceleration of electrons in the tip of streamers is not required since the low-energy electrons can be accelerated directly to runaway energies in the leader field. Accordingly, *Köhn and Ebert* (2015); *Köhn et al.* (2017b) initiated the seed electrons with 0.1 eV energy and were also able to reproduce the observed intensity and energy of TGFs.

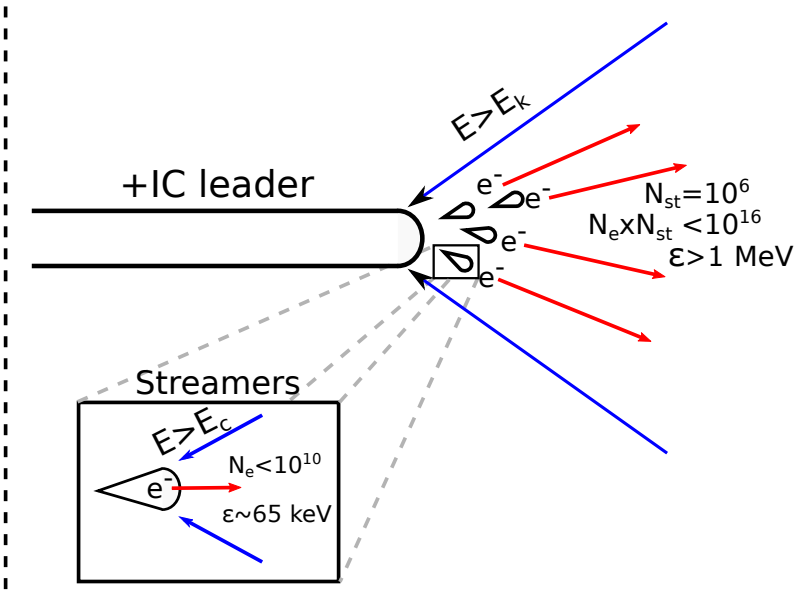

Figure 4.9: Illustration of the streamer-leader scenario. 10^6 streamers produced close to the tip of the negative end of +IC leader. At the tips of each streamer, up to 10^{10} electrons are accelerated to an average energy of 65 keV (*Celestin and Pasko*, 2011). The result is an intensity of up to 10^{16} relativistic electrons that then undergo further multiplication ($\sim 4\lambda$) and acceleration ($>$1 MeV) in the more extended leader electric field.

Interestingly, *Köhn et al.* (2017b) assumed a leader channel with potential difference between the tip and the center of the channel of 25 MV. They were able to reproduce a

sufficient intensity of electrons and photons with energies up to 50 MeV, estimated at an altitude of 150 km after 0.5 ms. In Paper III (*Skeltved et al.*, 2017), we showed that the effect of the ambient electric field become more important at higher altitude due to the lowering of density and thereby the friction force. The electric field thresholds (see Figure 4.1) are scaled by a simple factor

$$E^h = E^0 \frac{n(h)}{n(0)}, \tag{4.14}$$

where $n(h)$ is the density at an altitude h. The different studies assume different ambient electric field strengths. The assumed ambient electric field strengths, given as the fraction of E_{RREA} at the assumed altitudes h, are listed in Table 4.2.

Study	$\mathbf{E_0}$	**h (km)**
Celestin et al. (2012, 2015)	$0.17 \times E_{RREA}$	0
Skeltved et al. (2017)	$0.2 - 0.3 \times E_{RREA}$	10-14
Xu et al. (2012)	$0.17 \times E_{RREA}$	0
Köhn and Ebert (2015)	$1.45 \times E_{RREA}$	16
Köhn et al. (2017b)	$0.3 \times E_{RREA}$	4

Table 4.2: The assumed ambient electric field used in different leader field models. The threshold field strength is scaled to match the assumed altitude (last column) given in the cited papers.

For *Köhn and Ebert* (2015), relativistic feedback will become dominant as the RREAs develop beyond the high-field region of the leader, similar to the ambient field scenario. For *Köhn et al.* (2017b) the ambient electric field would become important at altitudes above roughly 13.6 km, where the assumed ambient field strength becomes equal to E_{RREA}. That could account for the difference between the obtained energies and that available in the region ahead of the leader where $E > E_{RREA}$.

4.4 Summary

Given rather extreme assumptions on electric field strength and spatial extent, the two scenarios can reproduce the intensity, energy and energy spectra of electrons and photons that correspond to measurements of TGFs.

It is important to emphasize, that the physical processes involved are very similar between the two scenarios. Both require seed electrons, both rely on RREAs to multiply and both can include relativistic feedback. However, there are also important differences. The ambient field scenario is more typically assumed to be initiated by cos-

mic ray secondaries. Although this scenario does not exclude streamers as the source of seed electrons, the streamer-leader scenario rely solely on streamers as its source. Furthermore, relativistic feedback may have a noticeable effect in the streamer-leader scenario, but it is of course crucial to the ambient field scenario.

The ability of the production scenarios to explain the measurements of TGFs

The correlation between +IC lightning and observations of TGFs (*Cummer et al.*, 2005, 2015), may suggest that a scenario involving the streamer-leader fields is likely. However, only up to 30% of TGFs has been associated with a lightning attributed radio wave signal (*Collier et al.*, 2011; *Connaughton et al.*, 2010; *Gjesteland et al.*, 2012), which means that roughly 70% may not be associated with discharges. Therefore, the association between production of TGFs and +IC lightning does not exclude the ambient field scenario.

The energy spectrum of TGFs has been associated with the 7 MeV exponential cut off characteristic to a fully developed RREA. Modeling results have shown that roughly 3.5 avalanche lengths is required to obtain this characteristic spectrum (*Celestin et al.*, 2015; *Skeltved et al.*, 2017). It was noted that the shape of the photon energy spectrum, that is the results of bremsstrahlung emission from RREAs, does not change much depending on whether the RREA is fully developed, or not. Furthermore, the measured maximum photon energy of TGFs ranges from roughly 5 MeV to 40 MeV (*Marisaldi et al.*, 2010). It may be possible that the photon spectrum consistent with the less energetic TGFs is produced by RREAs that was not in a fully developed state. As we pointed out in Paper III (*Skeltved et al.*, 2017), that could be explained by streamer-leader field scenario if one assume shorter leader channels, or long channels in a weaker ambient electric field.

Chapter 5

Models used to describe the production of TGFs

Direct measurement of the electrons and photons at the source of a TGF is of course very hard to obtain. Therefore we rely on computer modeling to provide further insight. The computer models that have been discussed throughout this thesis are Monte Carlo models. Monte Carlo models uses cross-sections to estimate how particles interact under given assumptions. Several studies have compared the results from different models that uses similar assumptions (*Dwyer et al.*, 2012; *Rutjes et al.*, 2016; *Skeltved et al.*, 2017, 2014). In Paper II (*Rutjes et al.*, 2016), we established a series of baseline tests to do a comprehensive comparison of the different models. *Dwyer et al.* (2012) and Papers I and II (*Rutjes et al.*, 2016; *Skeltved et al.*, 2014) found that results obtained from existing Monte Carlo models were in good agreement. Note that we did not consider the effects of electric fields in Paper II (*Rutjes et al.*, 2016).

Given the same assumptions and simulation setup, the models we tested in Paper II gave similar results (*Rutjes et al.*, 2016). However, the choice of assumptions is important. An unresolved question in terms of the production of TGFs is the configuration of the electric field. As have been discussed throughout this thesis, the electric field is the driving force of the electron acceleration and multiplication. Thus of primary importance. In this chapter, we will discuss different electric field configurations that may be a realistic representation of the electric field that is the source of TGF production.

5.1 Electric field models

The simplest electric field model is the uniform ambient electric field, which is the basis for the ambient field scenario (*Dwyer*, 2003, 2012; *Köhn et al.*, 2017b; *Skeltved et al.*, 2017, 2014). Although simple, it is important to note that the altitude and density should be taken into account. The threshold field strengths scales with density, but the ambient electric field depends only on the charge in the charge layers and the sep-

aration between them. Therefore, the effect of the ambient electric field becomes more important with increasing altitude (as shown in Paper III (*Skeltved et al.*, 2017)).

The assumption of the uniform ambient electric field is also important to determine the electric field created by the leader. We now consider the simple case of a perfectly conducting channel immersed in an ambient electric field. Different shapes of the leader channel have been assumed. For the cylindrical shaped channel, with flat or capped ends, the numerical method of moments (*Balanis*, 2012, p. 679-691) and the stable method of moments (*Harrington*, 1993, p. 28-33) has been used (*Celestin et al.*, 2012, 2015; *Skeltved et al.*, 2017; *Xu et al.*, 2012). When assuming an elliptic channel, an analytical method can be applied (*Köhn and Ebert*, 2015; *Landau and Lifshitz*, 1960, p. 20-27). In Paper III (*Skeltved et al.*, 2017), we showed that the stable method of moments is more accurate than the method of moments. The solution converges to a stable solution with increasing number of elements, whereas the solution from the method of moments becomes unstable when the length of an element is smaller than the radius of the object. In addition, we pointed out that the analytical method is of course accurate, but an elliptically shaped channel is not a realistic representation of a natural lightning leader (see Paper III (*Skeltved et al.*, 2017)). The electric field ahead of the leader is then the sum of that created by the leader and the ambient electric field. This approximation does not take into account the screening effects of the streamer zone.

As discussed in Section 4.3.2, we will now consider the moment when a streamer zone has fully developed, just before the space leader forms. *Bazelyan and Raizer* (2000) argue that the extent of the streamer zone is typically related to the potential difference between center of the leader and its tip by

$$z_{sz} = \frac{\phi_{tip}}{E_{cr}^{-}} \tag{5.1}$$

where $E_{cr}^{-} = 12.5$ kV/cm is the critical field strength for negative streamers to propagate, and ϕ_{tip} is given from Equation 2.2. After the streamer zone has formed, the electric field can be considered to be radially uniform with a strength equal to E_{cr}^{-}. The potential drop ahead of the leader tip, with distance, is shown in Figure 5.1. The sum of the electric field created by the leader and the ambient electric field, is shown as the blue curve, and the radially uniform electric field consistent with a fully developed streamer zone is the red curve. Using Equation 5.1, where $\phi_{tip} = 80$ MV, and $E_{cr}^{-} = 12.5$ kV/cm, one find the length of the streamer zone to be $z_{sz} = 64$ m.

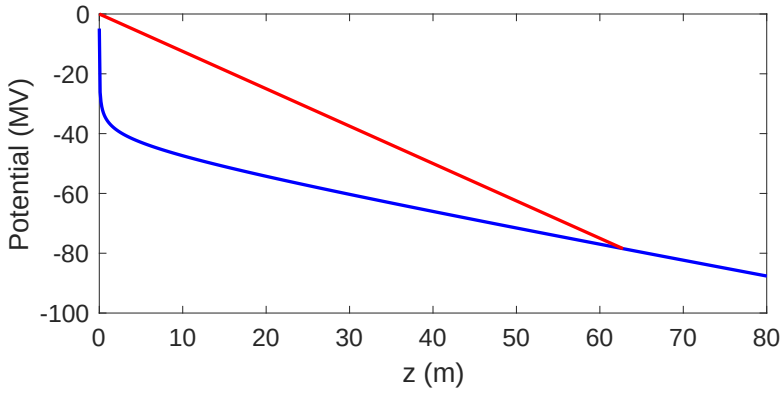

Figure 5.1: The potential drop ahead of the leader tip. The blue curve shows the potential drop given the nonuniform electric field of a perfectly conducting leader. The red curve shows the assumed potential drop through a fully developed streamer zone. Calculated for sea-level density and pressure.

The relationship between the leader tip potential and threshold field strength for negative streamers, and the length of the streamer zone (described by Equation 5.1), has been used by several models that discuss the propagation of negative leader discharges (*Arevalo and Cooray*, 2011; *Mazur et al.*, 2000). The production of TGFs with this assumption of electric field configuration, may not be realistic. As was explained in section 4.3.2, the streamer-leader field scenario relies on the production of seed electrons in streamer tips. Moreover, to produce seed electrons the electric field in streamer tips must exceed the thermal runaway threshold $E_c \approx 260$ kV/cm (sea level equivalent). That may not be realistic as models have shown that electric fields near $1.5E_k \approx 4E_{cr}^{-}$ is required (*Celestin and Pasko*, 2011; *Moss et al.*, 2006). However, as was pointed out, it is not well understood how the potential increases on the leader tip after a step has completed. A combination of the non-existing and fully developed streamer zones, may be a more realistic representation of the electric field at the time when TGFs are assumed to be produced.

We will not attempt to estimate the temporal development of the leader electric field during the leader step. However, the concept is illustrated in Figure 5.2. 1) A fully developed streamer zone (dashed blue segment). 2) Formation and initial development of space leader. 3) Positive end of space leader develops either faster or just before the negative end, during which a streamer zone has formed ahead of the negative end of the space leader. 4) As the space leader and main leader attach, a discharge wave redistributes charge from the main channel to the new segment (red)(*Bazelyan and Raizer*, 2000, p. 198). 5) During the charge redistribution, the streamer zone ahead of the space leader can develop. 6) The step is completed and a corona discharge can occur. However, the region ahead of the leader has a developed streamer zone. The radius of the

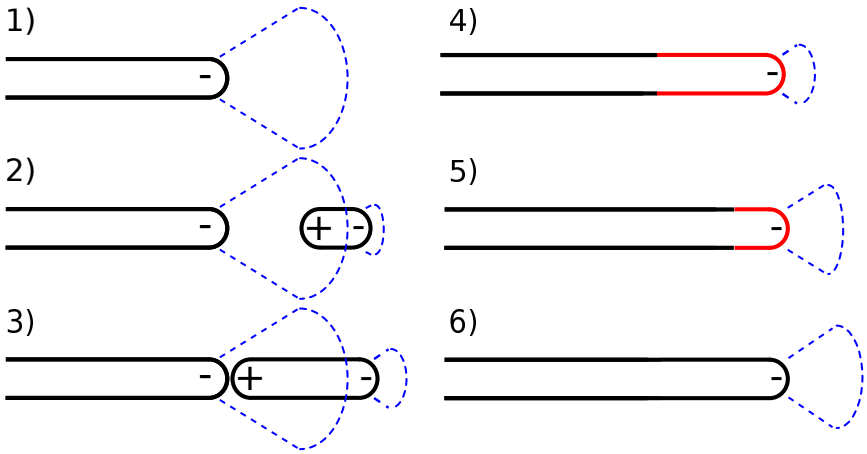

Figure 5.2: The stepping of a negative end of a +IC leader. This figure illustrates the concept of the development of the streamer zone ahead of the negative ends of the main leader channel and the space leader.

streamer zone depends on the total time of the step and on the characteristic shape of the discharge wave.

Chapter 6

Summary of papers

6.1 Paper I: Modeling the relativistic runaway electron avalanche and the feedback mechanism with GEANT4

The first paper that is included in this thesis aimed to test the relativistic feedback scenario. Relativistic feedback was introduced in *Dwyer* (2003) as a mechanism to explain the multiplication of electrons that is needed to produce the observed TGFs. *Gurevich et al.* (1992) had shown that a significant flux of electrons could be produced by RREAs initiated from cosmic ray secondary particles. However, the flux of electrons fell orders of magnitude short of the assumed intensity that is necessary to produce TGFs. *Dwyer* (2003) proposed that backscattering of photons and positrons within the avalanche region, where $E > E_{RREA} = 2.84$ kV/cm, could increase the number of RREAs at an exponential rate. This mechanism was shown to be effective when regions with sufficient electric field and electric potentials was present within a thundercloud. Following the results in *Dwyer* (2003), this mechanism was further developed in *Coleman and Dwyer* (2006); *Dwyer* (2008, 2012).

We used the open source Geant4 modeling toolkit (http://geant4.cern.ch). It is a well established Monte Carlo modeling toolkit develop at CERN, which is the acronym of the French "Conseil Européen pour la Recherche Nucléaire", or European Council for Nuclear Research. To test the accuracy of the model, we modeled the development of RREAs from a monoenergetic beam of 1 MeV electrons. We used the comparisson presented in *Dwyer* (2012) as a reference to compare with the Geant4 results. We tested two different physics libraries developed for low-energy (< 100 MeV) physics. Based on how the two physics lists implemented cross-sections to the model, we concluded that the LBE (Low Background Experiments) library, which also provided results that was consistent with *Dwyer* (2003), was the most accurate. The result was important, since the inconsistencies between models were between 25% and 60% depending on

the eletric field strength. It highlighted the importance of testing the physics libraries, even with well established open source computer models.

Previously, relativistic feedback had only be estimated by *Dwyer* (2003) using a custom model. We used the confirmed LBE physics list to estimate the conditions required for relativistic feedback to be effective, that is for the feedback factor $\gamma > 1$. The results was in good agreement with the results by *Dwyer* (2003) and an important confirmation of the results.

Satellite observations of TGFs are most often assumed to be of energetic photons. It is therefore useful to estimate the ratio of bremsstrahlung photons to runaway electrons. We compared the number of produced photons with energy above different thresholds, ε_{th}, to the number of runaway electrons above the same energy threshold. The simulations were also performed for different electric field strengths. We found that the ratio decreased with increasing electric field strength and with increasing energy thresholds. For a lower energy threshold of 1 MeV, the ratio decreased from 1 to 0.1 with increasing electric field strengths from 4 kV/cm to 20 kV/cm. For an electric field strength of 4 kV/cm, the ratio also decreased from 1 to 0.1 with increasing energy thresholds from 100 keV to 10 MeV.

6.2 Paper II: Evaluation of monte carlo tools for high energy atmospheric physics

In this paper, out goal was to determine the differences between Monte Carlo models that have been used in the context of explaining TGFs. We compared Geant4, EGS5 and FLUKA which are established open sourced toolkits, and the custom made codes MC-PEPTITA and GRRR. A set of basic tests were performed to test how the transport of electrons, photons and positrons were handled.

In short, we focused on the evolution of monoenergetic and beams of electrons, positrons and photons with kinetic energies between 100 keV and 40 MeV through homogeneous air in the absence of electric and magnetic fields, using a low energy cutoff of 50 keV. The effects of introducing an electric field is discussed, but not included.

With this comparison we found that the different models produce converging results, but some differences were identified. One important source of inconsistency between the models is straggling. Straggling is when high energy particles only lose energy as function of distance rather than the explicit production of low energy particles. Depending on how the continuous energy loss is introduced, change in direction and energy can become less accurate. We also found that EGS5 has an approximation for bremsstrahlung that is not accurate in the energy range of TGFs. Lastly, for

all models, we found that the opening angle of photons after Compton interactions are very sensitive to the low energy cut off.

Another useful parameter is the efficiency of the codes. There is a big difference between the completion time of the different codes, given the same simulation setups.

With this study, we also wished to remark the importance of making open sourced and custom made codes available for use, testing and comparison. Future work is aimed at comparing more custom made codes as well as more comprehensive benchmark tests.

6.3 Paper III: Constraints to do realistic modeling of the electric field ahead of the tip of a lightning leader

This paper was written in the context of the production of TGFs from electron acceleration and multiplication in the electric fields in streamer tips and ahead of a lightning leader. We compared the constraints introduced in previous studies (*Celestin et al.*, 2012, 2015; *Köhn and Ebert*, 2015; *Xu et al.*, 2012), and then presented an argument for a realistic set of constraints.

We argued that a maximum electric field of around 1.5 times the conventional breakdown threshold is the most realistic upper limit, consistent with *Bazelyan and Raizer* (2000). The region ahead of the leader that is between this maximum limit and the distance where the electric field drops below the RREA threshold, was then defined to be the acceleration and multiplication (AM) region. The number of avalanche lengths, the potential difference and the ratio of the potential difference in the AM region to the potential difference between the tip and the center of the leader, was estimated. To explain the characteristic RREA energy spectrum and a maximum energy of ~ 40 MeV, we concluded that leaders of more than 200 MV potential difference, center to tip, or 400 MV between the tips, are required. Different from the conclusions of *Köhn and Ebert* (2015); *Xu et al.* (2012).

Furthermore, we compared typical ambient electric field strengths from balloon measurements (*Marshall and Stolzenburg*, 2001; *Stolzenburg et al.*, 1998, 2007), to the assumptions used in the computer models. The balloon measurements show that the ambient electric field strengths are relatively uniform and depends on amount of charge in the charge layer, not on density. We showed that when scaling of the threshold field strengths are taken into account, the ambient electric field therefore become increasingly important with altitude. We then compared typical balloon measurements to assumptions that has been used in different models. We found that the strength of the ambient fields that was used by *Celestin et al.* (2015); *Xu et al.* (2012) were much

weaker, and that in *Köhn and Ebert* (2015) the assumed ambient field was roughly 3 times stronger than measurements suggest.

We also discussed the configuration of the strongly nonuniform electric field that has been used by existing models of the streamer-leader scenario (*Celestin and Pasko*, 2011; *Köhn and Ebert*, 2015; *Skeltved et al.*, 2017; *Xu et al.*, 2012). In short, the effects of a streamer zone ahead of the leader, which would otherwise displace the electric field in that region, is approximated by an artifical upper limit of electric field. By that method, the portion of the electric field that would have been discplaced, is "lost", and thereby does not contribute to the acceleration of electrons. We argued that a more realistic representation of how the electric field changes with time ahead of the leader, is likely to have an important effect. We found that the approximation of a maximum electric field strength near the leader tip will lead to a loss of 25%-75% of the potential difference in the AM region, depending on the set limit.

Bibliography

Arevalo, L., and V. Cooray, Preliminary study on the modelling of negative leader discharges, *Journal of Physics D: Applied Physics*, *44*(31), 315,204, doi:10.1088/0022-3727/44/31/315204, 2011. 45

Babich, L., I. M. Kutsyk, E. N. Donskoy, and A. Y. Kudryavtsev, New data on space and time scales of relativistic runaway electron avalanche for thunderstorm environment: Monte Carlo calculations, *Physics Letters A*, *245*, 460–470, 1998. 26, 27

Babich, L., E. Donskoy, I. Kutsyk, A. Kudryavtsev, R. Roussel-Dupre, B. Shamraev, and E. Symbalisty, Comparison of relativistic runaway electron avalanche rates obtained from Monte Carlo simulations and kinetic equation solution, *IEEE Transactions on Plasma Science*, *29*(3), 430–438, doi:10.1109/27.928940, 2001. 26

Babich, L. P., The feedback mechanism of runaway air breakdown, *Geophysical Research Letters*, *32*(9), doi:10.1029/2004GL021744, 2005. 26

Balanis, C. A., *Advanced Engineering Electronmagnetics*, 2. edition ed., 2012. 44

Bazelyan, E. M., and Y. P. Raizer, *Lightning Physics and Lightning Protection*, 1.st ed., Nicki Dennis, New York, 2000. 13, 35, 37, 38, 44, 45, 49

Briggs, M. S., et al., First results on terrestrial gamma ray flashes from the Fermi Gamma-ray Burst Monitor, *Journal of Geophysical Research*, *115*(A7), A07,323, doi:10.1029/2009JA015242, 2010. 15, 16

Briggs, M. S., et al., Terrestrial gamma-ray flashes in the Fermi era: Improved observations and analysis methods, *Journal of Geophysical Research: Space Physics*, *118*(6), 3805–3830, doi:10.1002/jgra.50205, 2013. 17

Carlson, B. E., N. G. Lehtinen, and U. S. Inan, Constraints on terrestrial gamma ray flash production from satellite observation, *Geophysical Research Letters*, *34*(8), L08,809, doi:10.1029/2006GL029229, 2007. 19

Carlson, B. E., N. G. Lehtinen, and U. S. Inan, Runaway relativistic electron avalanche seeding in the Earth's atmosphere, *Journal of Geophysical Research*, *113*(A10), A10,307, doi:10.1029/2008JA013210, 2008. 29, 30

Celestin, S., and V. P. Pasko, Soft collisions in relativistic runaway electron avalanches, *Journal of Physics D: Applied Physics*, *43*(31), 315,206, doi:10.1088/0022-3727/43/31/315206, 2010. 27

Celestin, S., and V. P. Pasko, Energy and fluxes of thermal runaway electrons produced by exponential growth of streamers during the stepping of lightning leaders and in transient luminous events, *Journal of Geophysical Research*, *116*(A3), 1–14, doi:10.1029/2010JA016260, 2011. 12, 20, 24, 26, 27, 34, 35, 36, 37, 38, 39, 45, 50

Celestin, S., W. Xu, and V. P. Pasko, Terrestrial gamma ray flashes with energies up to 100 MeV produced by nonequilibrium acceleration of electrons in lightning, *Journal of Geophysical Research: Space Physics*, *117*(5), 1–9, doi:10.1029/2012JA017535, 2012. 20, 27, 34, 37, 38, 39, 40, 44, 49

Celestin, S., W. Xu, and V. P. Pasko, Variability in fluence and spectrum of high-energy photon bursts produced by lightning leaders, *Journal of Geophysical Research: Space Physics*, *120*(10), 712–723, doi:10.1002/2015JA021410, 2015. 12, 26, 27, 37, 38, 39, 40, 41, 44, 49

Chanrion, O., and T. Neubert, Production of runaway electrons by negative streamer discharges, *Journal of Geophysical Research*, *115*, A00E32, doi:10.1029/2009JA014774, 2010. 24, 34

Coleman, L. M., and J. R. Dwyer, Propagation speed of runaway electron avalanches, *Geophysical Research Letters*, *33*(11), 1–4, doi:10.1029/2006GL025863, 2006. 26, 47

Collier, A. B., T. Gjesteland, and N. Østgaard, Assessing the power law distribution of TGFs, *Journal of Geophysical Research: Space Physics*, *116*(10), 1–18, doi:10.1029/2011JA016612, 2011. 18, 41

Connaughton, V., et al., Associations between Fermi Gamma-ray Burst Monitor terrestrial gamma ray flashes and sferics from the World Wide Lightning Location Network, *Journal of Geophysical Research: Space Physics*, *115*(12), 1–14, doi:10.1029/2010JA015681, 2010. 18, 41

Cooray, V., *An Introduction to Lightning*, 1st ed., Springer, Uppsala,Sweden, doi:10.1007/978-94-017-8938-7, 2015. 5, 8, 11

Cooray, V., L. Arevalo, M. Rahman, J. Dwyer, and H. Rassoul, On the possible origin of X-rays in long laboratory sparks, *Journal of Atmospheric and Solar-Terrestrial Physics*, *71*(17-18), 1890–1898, doi:10.1016/j.jastp.2009.07.010, 2009. 24

Cummer, S. A., Y. Zhai, W. Hu, D. M. Smith, L. I. Lopez, and M. A. Stanley, Measurements and implications of the relationship between lightning and terrestrial gamma ray flashes, *Geophysical Research Letters*, *32*(8), L08,811, doi:10.1029/2005GL022778, 2005. 1, 18, 19, 41

Cummer, S. a., G. Lu, M. S. Briggs, V. Connaughton, S. Xiong, G. J. Fishman, and J. R. Dwyer, The lightning-TGF relationship on microsecond timescales, *Geophysical Research Letters*, *38*(14), 1–6, doi:10.1029/2011GL048099, 2011. 18, 19

Cummer, S. A., F. Lyu, M. S. Briggs, G. Fitzpatrick, O. J. Roberts, and J. R. Dwyer, Lightning leader altitude progression in terrestrial gamma-ray flashes, *Geophysical Research Letters*, *42*, 7792–7798, doi:10.1002/2015GL065228, 2015. 12, 18, 19, 41

Dwyer, J. R., A fundamental limit on electric fields in air, *Geophysical Research Letters*, *30*(20), 1–4, doi:10.1029/2003GL017781, 2003. 2, 26, 27, 29, 30, 32, 43, 47, 48

Dwyer, J. R., Relativistic breakdown in planetary atmospheres, *Physics of Plasmas*, *14*(4), 042,901, doi:10.1063/1.2709652, 2007. 32

Dwyer, J. R., Source mechanisms of terrestrial gamma-ray flashes, *Journal of Geophysical Research*, *113*(D10), 1–12, doi:10.1029/2007JD009248, 2008. 47

Dwyer, J. R., The relativistic feedback discharge model of terrestrial gamma ray flashes, *Journal of Geophysical Research*, *117*(A2), 1–25, doi:10.1029/2011JA017160, 2012. 27, 30, 31, 33, 34, 43, 47

Dwyer, J. R., and L. P. Babich, Low-energy electron production by relativistic runaway electron avalanches in air, *Journal of Geophysical Research: Space Physics*, *116*(9), doi:10.1029/2011JA016494, 2011. 26, 27

Dwyer, J. R., and D. M. Smith, A comparison between Monte Carlo simulations of runaway breakdown and terrestrial gamma-ray flash observations, *Geophysical Research Letters*, *32*(22), 1–4, doi:10.1029/2005GL023848, 2005. 19, 20

Dwyer, J. R., and M. A. Uman, The physics of lightning, *Physics Reports*, *534*, 147–241, doi:10.1016/j.physrep.2013.09.004, 2014. 9

Dwyer, J. R., D. M. Smith, and S. a. Cummer, High-Energy Atmospheric Physics: Terrestrial Gamma-Ray Flashes and Related Phenomena, *Space Science Reviews*, *173:133*, doi:10.1007/s11214-012-9894-0, 2012. 26, 27, 43

Dwyer, J. R., N. Liu, and H. K. Rassoul, Properties of the thundercloud discharges responsible for terrestrial gamma-ray flashes, *Geophysical Research Letters*, *40*(15), 4067–4073, doi:10.1002/grl.50742, 2013. 19

Fishman, G. J., et al., Discovery of intense gamma-ray flashes of atmospheric origin., *Science (New York, N.Y.)*, *264*(5163), 1313–1316, doi:10.1126/science.264.5163.1313, 1994. 1, 15, 16, 19

Fishman, G. J., et al., Temporal properties of the terrestrial gamma-ray flashes from the Gamma-Ray Burst Monitor on the Fermi Observatory, *Journal of Geophysical Research: Space Physics*, *116*(7), 1–17, doi:10.1029/2010JA016084, 2011. 16

Franklin, B., *Experiments and Observations on Electricity*, 3rd ed., 154 pp., London: D Henry and E. Cave, Philadelphia, 1760. 5

Gilbert, W., *On the Loadstone and Magnetic Bodies, and on the Great Magnet the Earth. Translated by P. Fleury Mottelay*, 359 pp., Royal College of Physicians of London, London, 1893. 5

Gjesteland, T., N. Østgaard, P. H. Connell, J. Stadsnes, and G. J. Fishman, Effects of dead time losses on terrestrial gamma ray flash measurements with the Burst and Transient Source Experiment, *Journal of Geophysical Research*, *115*, 1–26, doi:10.1029/2009JA014578, 2010. 19

Gjesteland, T., N. Østgaard, A. B. Collier, B. E. Carlson, C. Eyles, and D. M. Smith, A new method reveals more TGFs in the RHESSI data, *Geophysical Research Letters*, *39*(5), 93–97, doi:10.1029/2012GL050899, 2012. 17, 18, 41

Grefenstette, B. W., D. M. Smith, B. J. Hazelton, and L. I. Lopez, First RHESSI terrestrial gamma ray flash catalog, *Journal of Geophysical Research: Space Physics*, *114*(2), 1–19, doi:10.1029/2008JA013721, 2009. 16, 17

Gurevich, a. V., G. M. Milikh, and R. Roussel-Dupré, Runaway electron mechanism of air breakdown and preconditioning during a thunderstorm, *Physics Letters A*, *165*(5-6), 463–468, doi:10.1016/0375-9601(92)90348-P, 1992. 2, 25, 27, 28, 47

Harrington, R. F., *Field computation by Moment Method*, IEEE Press, Macmillan Publishing Company, Arizona, 1993. 44

Ihaddadene, M. A., and S. Celestin, Increase of the electric field in head-on collisions between negative and positive streamers, *Geophysical Research Letters*, *42*(13), 5644–5651, doi:10.1002/2015GL064623, 2015. 24, 35

Inan, U. S., S. C. Reising, G. J. Fishman, and J. M. Horack, On the association of terrestrial gamma-ray bursts with lightning and implications for sprites, *Geophysical Research Letters*, *23*(9), 1017–1020, 1996. 1, 15, 18, 19

Jayaratne, E., C. Saunders, and J. Hallet, Laboratory studies of the charging of soft-hail during ice crystal interactions., *Q.J.R. Meteor. Soc.*, *109*, 609–630, doi:10.1002/qj.49710946111, 1983. 6, 7

Köhn, C., and U. Ebert, Calculation of beams of positrons, neutrons, and protons associated with terrestrial gamma ray flashes, *Journal of Geophysical Research: Atmospheres*, *120*, 1620–1635, doi:10.1002/2014JD022229, 2015. 12, 26, 34, 37, 38, 39, 40, 44, 49, 50

Köhn, C., O. Chanrion, and T. Neubert, Electron acceleration during streamer collisions in air, *Geophysical Research Letters*, *44*(5), 2604–2613, doi:10.1002/2016GL072216, 2017a. 24, 25, 35

Köhn, C., G. Diniz, and M. N. Harakeh, Production mechanisms of leptons, photons, and hadrons and their possible feedback close to lightning leaders, *Journal of Geophysical Research: Atmospheres*, *122*, 1365–1383, doi:10.1002/2016JD025445, 2017b. 34, 35, 37, 38, 39, 40, 43

Landau, L. D., and E. M. Lifshitz, *Electrodynamics of continous media, Volume 8 of Course of Theoretical Physics*, Pergamon press, Oxford, London, New York, Paris, 1960. 44

Lehtinen, N. G., M. Walt, U. Inan, T. F. Bell, and V. P. Pasko, Gamma-ray emission produced by a relativistic beam of runaway electrons accelerated by quasi-electrostatic thundercloud fields, *Geophysical Research Letters*, *23*(19), 2645–2648, 1996. 19

Lehtinen, N. G., T. F. Bell, and U. S. Inan, Monte Carlo simulation of runaway MeV electron breakdown with application to red sprites and terrestrial gamma ray flashes, *Journal of Geophysical Research*, *104*(A11), 24,699, doi:10.1029/1999JA900335, 1999. 26, 27

Liu, N., and V. P. Pasko, Effects of photoionization on propagation and branching of positive and negative streamers in sprites, *Journal of Geophysical Research*, *109*(A4), A04,301, doi:10.1029/2003JA010064, 2004. 10, 35, 36

Lu, G., et al., Lightning mapping observation of a terrestrial gamma-ray flash, *Geophysical Research Letters*, *37*(11), n/a–n/a, doi:10.1029/2010GL043494, 2010. 18, 19

Mallios, S. a., S. Celestin, and V. P. Pasko, Production of very high potential differences by intracloud lightning discharges in connection with terrestrial gamma ray flashes, *Journal of Geophysical Research: Space Physics*, *118*(2), 912–918, doi:10.1002/jgra.50109, 2013. 12

Marisaldi, M., et al., Detection of terrestrial gamma ray flashes up to 40 MeV by the AGILE satellite, *Journal of Geophysical Research*, *115*, 1–12, doi:10.1029/2009JA014502, 2010. 1, 15, 16, 19, 20, 21, 41

Marisaldi, M., et al., Enhanced detection of terrestrial gamma-ray flashes by AGILE, *Geophysical Research Letters*, *42*, 9481–9487, doi:10.1002/2015GL066100, 2015. 16

Marshall, T. C., and D. W. Rust, Electric Field Soundings Through Thunderstorms, *Journal of Geophysical Research*, *96*(91), 22,297–22,306, doi:10.1029/91JD02486, 1991. 7

Marshall, T. C., and M. Stolzenburg, Electric field measurements above mesoscale convective systems, *Journal of Geophysical Research*, *101*, 6979–6996, doi:10.1029/95JD03764, 1996. 7

Marshall, T. C., and M. Stolzenburg, Voltages inside and just above thunderstorms, *Journal of Geophysical Research*, *106*(2000), 4757–4768, doi:10.1029/2000JD900640, 2001. 7, 30, 49

Mazur, V., L. H. Ruhnke, and P. Lalande, Computer simulation of a downward negative stepped leader and its interaction with a ground structure, *Journal of Geophysical Research: Atmospheres*, *105*(D17), 22,361–22,369, doi:10.1029/2000JD900278, 2000. 45

Mccarthy, M., and G. K. Parks, Further observations of X-rays inside thunderstorms, *Geophysical Research Letters*, *12*(6), 393–396, 1985. 25

Moss, G. D., V. P. Pasko, N. Liu, and G. Veronis, Monte Carlo model for analysis of thermal runaway electrons in streamer tips in transient luminous events and streamer zones of lightning leaders, *Journal of Geophysical Research*, *111*(A2), 1–37, doi:10.1029/2005JA011350, 2006. 2, 9, 24, 34, 35, 36, 37, 45

Østgaard, N., T. Gjesteland, J. Stadsnes, P. H. Connell, and B. Carlson, Production altitude and time delays of the terrestrial gamma flashes: Revisiting the Burst and Transient Source Experiment spectra, *Journal of Geophysical Research*, *113*(A2), 1–14, doi:10.1029/2007JA012618, 2008. 19

Østgaard, N., T. Gjesteland, R. S. Hansen, A. B. Collier, and B. Carlson, The true fluence distribution of terrestrial gamma flashes at satellite altitude, *Journal of Geophysical Research*, *117*(November 2011), 1–8, doi:10.1029/2011JA017365, 2012. 18

Østgaard, N., T. Gjesteland, B. Carlson, A. Collier, S. Cummer, G. Lu, and H. Christian, Simultaneous observations of optical lightning and terrestrial gamma flash from space, *Geophysical Research Letters*, *40*, 2423–2426, doi:doi:10.1002/grl.50466, 2013. 19

Østgaard, N., K. H. Albrecthsen, T. Gjesteland, and A. Collier, A new population of terrestrial gamma-ray flashes in the RHESSI data, *Geophysical Research Letters*, *42*(24), doi:10.1002/2015GL067064, 2015. 17, 18

Parks, G. K., B. H. Mauk, R. Spiger, and J. Chin, Xray enhancements detected during thunderstorm and lightning activities, *Geophysical Research Letters*, *8*(11), 1176–1179, doi:10.1029/GL008i011p01176, 1981. 25

Pasko, V. P., Electrostatic modeling of intracloud stepped leader electric fields and mechanisms of terrestrial gamma ray flashes, *Geophysical Research Letters*, *41*, 179–185, doi:10.1002/2013GL058983, 2013. 12

Rakov, V. a., and M. A. Uman, *Lightning, Physics and Effects*, Cambridge University Press, Cambridge, 2003. 8, 12

Rutjes, C., D. Sarria, A. B. Skeltved, A. Luque, G. Diniz, N. Østgaard, and U. Ebert, Evaluation of monte carlo tools for high energy atmospheric physics, *Geoscientific Model Development*, *9*(11), 3961–3974, doi:10.5194/gmd-9-3961-2016, 2016. 2, 43

Shao, X.-M., T. Hamlin, and D. M. Smith, A closer examination of terrestrial gamma-ray flash-related lightning processes, *Journal of Geophysical Research*, *115*(April 2004), A00E30, doi:10.1029/2009JA014835, 2010. 18, 19

Skeltved, A., N. Østgaard, A. Mezentsev, N. Lehtinen, and B. Carlson, Constraints to do realistic modeling of the electric field ahead of the tip of a lightning leader, *Journal of Geophysical Research: Atmospheres*, *122*, doi:10.1002/2016JD026206, 2017. 2, 26, 28, 34, 37, 38, 39, 40, 41, 43, 44, 50

Skeltved, A. B., N. Østgaard, B. Carlson, T. Gjesteland, and S. Celestin, Modeling the relativistic runaway electron avalanche and the feedback mechanism with GEANT4, *Journal of Geophysical Research: Space Physics*, *119*(11), 9174–9191, doi:10.1002/2014JA020504, 2014. 2, 26, 27, 30, 32, 34, 43

Smith, D. M., L. I. Lopez, R. P. Lin, and C. P. Barrington-Leigh, Terrestrial gamma-ray flashes observed up to 20 MeV., *Science (New York, N.Y.)*, *307*(5712), 1085–1088, doi:10.1126/science.1107466, 2005. 15, 16, 19, 20

Stanley, M. a., X.-M. Shao, D. M. Smith, L. I. Lopez, M. B. Pongratz, J. D. Harlin, M. Stock, and A. Regan, A link between terrestrial gamma-ray flashes and intracloud lightning discharges, *Geophysical Research Letters*, *33*(6), L06,803, doi:10.1029/2005GL025537, 2006. 19

Stolzenburg, M., W. D. Rust, and T. C. Marshall, Electrical structure in thunderstorm convective regions 3. Synthesis, *Journal of Geophysical Research*, *103*(D12), 14,097–14,108, doi:10.1029/97JD03545, 1998. 49

Stolzenburg, M., T. C. Marshall, W. D. Rust, E. Bruning, D. R. MacGorman, and T. Hamlin, Electric field values observed near lightning flash initiations, *Geophysical Research Letters*, *34*(4), 1–7, doi:10.1029/2006GL028777, 2007. 7, 8, 33, 49

Takahashi, T., Riming Electrification as a Charge Generation Mechanism in Thunderstorms, *Journal of the Atmospheric Sciences*, *35*(8), 1536–1548, doi:10.1175/1520-0469(1978)035<1536:REAACG>2.0.CO;2, 1978. 6, 7

Tavani, M., et al., Terrestrial Gamma-Ray Flashes as Powerful Particle Accelerators, *Physical Review Letters*, *106*(1), 1–5, doi:10.1103/PhysRevLett.106.018501, 2011. 20

Williams, E. R., The Tripole Structure of Thunderstorms, *Journal of Geophysical Research: Atmospheres*, *94*(11), 2156–2202, doi:10.1029/JD094iD11p13151, 1989. 6

Wilson, C. T. R., The electric field of a thundercloud and some of its effects, *Proc. Phys. Soc. London 37 32D*, 1924. 15, 23

Wilson, C. T. R., The Acceleration of β-particles in Strong Electric Fields such as those of Thunderclouds, *Mathematical Proceedings of the Cambridge Philosophical Society*, *22*(04), 534, doi:10.1017/S0305004100003236, 1925. 1, 2, 15

Xu, W., S. Celestin, and V. P. Pasko, Source altitudes of terrestrial gamma-ray flashes produced by lightning leaders, *Geophysical Research Letters*, *39*(8), doi:10.1029/2012GL051351, 2012. 12, 27, 35, 37, 38, 39, 40, 44, 49, 50

Xu, W., S. Celestin, and V. P. Pasko, Optical emissions associated with energetic electrons produced by stepping leaders in cloud-to-ground lightning discharges, *Journal of Geophysical Research: Space Physics*, *120*, 5610–5616, doi:10.1002/2015GL064419, 2015. 12

Chapter 7

Scientific results

Paper I

7.1 Modeling the relativistic runaway electron avalanche and the feedback mechanism with GEANT4

Alexander Broberg Skeltved, Nikolai Østgaard, Brant Carlson, Thomas Gjesteland and Sebastien Celestin

Journal of Geophysical Research: Space Physics, 119, doi:10.1002/2014JA020504 (2014)

AGU PUBLICATIONS

JGR

Journal of Geophysical Research: Space Physics

RESEARCH ARTICLE
10.1002/2014JA020504

Key Points:
- Testing the feedback mechanism with GEANT4
- Validating the GEANT4 programming toolkit
- Study the ratio of bremsstrahlung photons to electrons at TGF source altitude

Correspondence to:
A. Broberg Skeltved,
abskeltved@yahoo.no

Citation:
Broberg Skeltved, A., N. Østgaard, B. Carlson, T. Gjesteland, and S. Celestin (2014), Modeling the relativistic runaway electron avalanche and the feedback mechanism with GEANT4, *J. Geophys. Res. Space Physics*, *119*, doi:10.1002/2014JA020504.

Received 12 AUG 2014
Accepted 12 OCT 2014
Accepted article online 16 OCT 2014

Modeling the relativistic runaway electron avalanche and the feedback mechanism with GEANT4

Alexander Broberg Skeltved[1], Nikolai Østgaard[1], Brant Carlson[1,2], Thomas Gjesteland[1], and Sebastien Celestin[3]

[1]Birkeland Centre for Space Science, Institute of Physics and Technology, University of Bergen, Bergen, Norway, [2]Physics and Astronomy, Carthage College, Kenosha, Wisconsin, USA, [3]Laboratory of Physics and Chemistry of the Environment and Space, University of Orleans, CNRS, Orleans, France

Abstract This paper presents the first study that uses the GEometry ANd Tracking 4 (GEANT4) toolkit to do quantitative comparisons with other modeling results related to the production of terrestrial gamma ray flashes and high-energy particle emission from thunderstorms. We will study the relativistic runaway electron avalanche (RREA) and the relativistic feedback process, as well as the production of bremsstrahlung photons from runaway electrons. The Monte Carlo simulations take into account the effects of electron ionization, electron by electron (MÃller), and electron by positron (Bhabha) scattering as well as the bremsstrahlung process and pair production, in the 250 eV to 100 GeV energy range. Our results indicate that the multiplication of electrons during the development of RREAs and under the influence of feedback are consistent with previous estimates. This is important to validate GEANT4 as a tool to model RREAs and feedback in homogeneous electric fields. We also determine the ratio of bremsstrahlung photons to energetic electrons N_γ/N_e. We then show that the ratio has a dependence on the electric field, which can be expressed by the avalanche time $\tau(E)$ and the bremsstrahlung coefficient $\alpha(\varepsilon)$. In addition, we present comparisons of GEANT4 simulations performed with a "standard" and a "low-energy" physics list both validated in the 1 keV to 100 GeV energy range. This comparison shows that the choice of physics list used in GEANT4 simulations has a significant effect on the results.

1. Introduction

Terrestrial gamma ray flashes were first discovered in the early 1990 by the Burst And Transient Source Experiment (BATSE) on board NASA's Compton Gamma Ray Observatory [*Fishman et al.*, 1994]. Since then, the observations of these submillisecond bursts of up to several tens of MeV photons have been confirmed in multiple studies [*Smith et al.*, 2005; *Briggs et al.*, 2010; *Marisaldi et al.*, 2010]. From modeling results and comparisons with the average photon energy spectrums obtained by satellite measurements, terrestrial gamma ray flashes (TGF) production has been determined to occur below 21 km altitude inside thundercloud regions [*Dwyer and Smith*, 2005; *Carlson et al.*, 2007; *Østgaard et al.*, 2008; *Gjesteland et al.*, 2010]. Measurements have shown that the intensities of TGFs range from 10^{14} photons [*Østgaard et al.*, 2012] to 10^{17} [*Dwyer and Smith*, 2005] if they are produced at 15 km altitude. *Hansen et al.* [2013] show that this intensity may vary with up to 3 orders of magnitude depending on the production altitude assumed. *Østgaard et al.* [2012], from the measurements available so far, argue that it cannot be ruled out that all discharges produce TGFs and that the lower intensity limit is then 10^{12}, again given a production altitude of 15 km. The number of electrons that are required, at source altitude, to produce these large fluxes of photons is generally assumed to be between the same and 1 order of magnitude larger than the number of photons.

The exact mechanism responsible for the production and multiplication of the energetic electrons is not yet fully understood. It is known, however, that the electric fields generated inside thunderclouds are capable of accelerating electrons to the energies required. Two leading theories currently exist to explain the multiplication of the energetic electrons and the subsequent production of bremsstrahlung photons.

1. The thermal acceleration of electrons in the tips of streamers and the subsequent acceleration during the stepping of lightning leaders [*Moss et al.*, 2006; *Williams et al.*, 2006; *Dwyer*, 2008, *Carlson et al.*, 2009, 2010; *Chanrion and Neubert*, 2010; *Celestin and Pasko*, 2011; *Xu et al.*, 2012].
2. The initiation of high-energy electrons from seed particles such as the products of cosmic rays. The continued multiplication and acceleration of these electrons through the relativistic runaway electron

AGU Journal of Geophysical Research: Space Physics 10.1002/2014JA020504

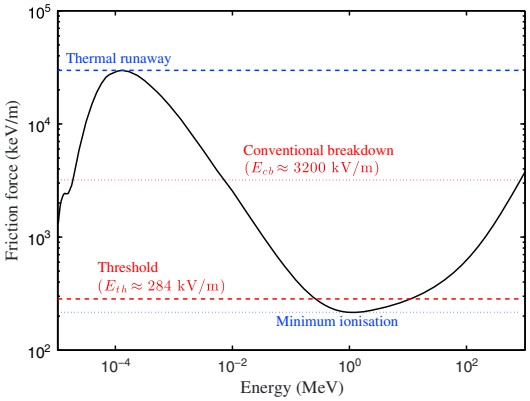

Figure 1. The friction force experienced by electrons in air at sea level with respect to their kinetic energy (solid black line). The dotted red line indicates the conventional breakdown field, $E_{cb} = 3200$ kV/m. The dashed red line show the effective minimum threshold force experienced by runaway electrons and corresponds to $E_{th} = 284$ kV/m [*Dwyer*, 2003]. The dashed blue line shows the upper threshold for thermal runaway to occur, and the lower dotted blue line indicates the minimum ionization threshold. The data set was obtained from *International Commission on Radiation Units and Measurements* [1984].

avalanche (RREA) process in the ambient electric field of the thundercloud [*Gurevich et al.*, 1992]. Finally, further multiplication of RREAs from backscattering photons and positrons, which is the feedback mechanism [*Dwyer*, 2003, 2007; *Dwyer and Babich*, 2011; *Dwyer*, 2012].

The electron multiplication through the feedback mechanism will be the subject of this paper. This mechanism is constrained by the available potential in the cloud as well as the strength, location, and vertical extent of the electric field. We will also discuss the ratio of bremsstrahlung photons to electrons at the end of the electric field region. This ratio is important when estimating the total number of electrons that is required at the source of TGFs. Results will be obtained using the GEometry And Tracking 4 (GEANT4, version 9.6) programming toolkit, which will be discussed in section 2.

This study completes the work first presented at the European Geophysical Union 2013 spring meeting [*Skeltved et al.*, 2013]. Another study that uses GEANT4 simulations of relativistic feedback discharges was presented at the American Geophysical Union 2013 fall meeting [*Gwen et al.*, 2013].

1.1. Runaway Electrons

Wilson [1925], based on observations of the tracks of energetic electrons in a cloud chamber, suggested a theory to explain the behavior of energetic electrons in a thundercloud. Wilson proposed that energetic electrons in air, such as can be produced from cosmic rays, can be accelerated to large energies by the strong electric fields produced in thunderclouds. These electric fields must be sufficiently strong to oppose the effective friction force resulting from electron interactions with air molecules. Electrons that continue to be accelerated then become runaway electrons (REs). The effective frictional force in air at sea level pressure and density, with respect to the kinetic energy of the electron, is shown in Figure 1. The minimum friction force for REs is experienced by electrons with a kinetic energy of ≈1 MeV. Monte Carlo simulations show that in order for REs to propagate large distances, the electric field threshold E_{th} is approximately 30% larger than the minimum ionization threshold and is equal to 284 kV/m (dashed red line) [*Dwyer*, 2003]. This is due to the effect of elastic scattering, which causes electrons to scatter out of alignment of the electric field. The upper limit, where local ionization can occur and which will cause streamers and subsequent lightning discharges to form, is called the conventional breakdown field, $E_{cb} \approx 3200$ kV/m (dotted red line). Thermal runaway occurs at approximately $10E_{cb}$. The average energy gained $d\varepsilon$ by runaway electrons traveling a given distance dz through a thundercloud can be expressed as a function of the electric field E and the opposing friction force F_d

$$d\varepsilon = dz(eE - F_d), \tag{1}$$

where e is the elementary charge.

1.2. Relativistic Runaway Electron Avalanche

In 1984 *McCarthy and Parks* [1985] reported intensive bursts of X-rays, which lasted a few seconds each and emanated from regions inside thunderstorms. McCarthy and Parks suggested that runaway electrons, which Wilson first described, produced the measured bremsstrahlung X-rays. However, this process could not explain the measured fluxes by itself. *Gurevich et al.* [1992] then introduced the idea that runaway electrons

AGU Journal of Geophysical Research: Space Physics 10.1002/2014JA020504

could undergo a multiplication process through high-energy electron-electron elastic scattering (primarily Møller scattering), and form an avalanche process antiparallel to the electric field. This process is called a relativistic runaway electron avalanche (RREA). Wilson also appears to have been aware of this avalanche effect as he in his personal notes described it as the "Snowball effect" [*Williams*, 2010].

The initiation of RREAs still relies upon the presence of seed electrons. A suggested source of high-energy seed electrons in the Earth's atmosphere are the extensive air showers (EAS) resulting from cosmic rays. *Carlson et al.* [2008] calculated that cosmic ray secondaries will be present within $\approx$ 1μs in spherical volumes of radius 100 m to 3 km at altitudes of 0.5 km to 29.5 km. We can then assume that RREAs will quickly be initiated when a region within a thundercloud is of sufficient electric field strength.

Gurevich et al. [1992] showed that the number of runaway electrons in one avalanche increases with time t and distance z and can be expressed as

$$\frac{dN_{RREA}}{dz} = \frac{1}{\lambda} N_{RREA}, \tag{2}$$

$$\frac{dN_{RREA}}{dt} = \frac{1}{\tau} N_{RREA}, \tag{3}$$

where λ is the avalanche growth length and τ is the avalanche growth time. Integrating over the total length of the avalanche region, from $z = 0$ to $z = L$, we get the total number of runaway electrons produced in a RREA

$$N_{RREA} = N_0 \exp(L/\lambda), \tag{4}$$

or, over total time, from $t = 0$ to $t = t$

$$N_{RREA} = N_0 \exp(t/\tau). \tag{5}$$

Based on the MC model presented in *Dwyer* [2003], *Coleman and Dwyer* [2006] presented the e-folding length or avalanche length λ expressed as a function of electric field strength, E,

$$\lambda(E) = \frac{7300\,\text{kV}}{E - 276\,\text{kV/m}}. \tag{6}$$

In addition, the avalanche time τ was expressed as

$$\tau(E) = \frac{27.3\,\text{kV}\,\mu\text{s/m}}{E - 277\,\text{kV/m}} = \frac{\lambda}{0.89c}, \tag{7}$$

where c is the speed of light and $0.89c$ is the average speed of the propagating avalanche (also determined from Monte Carlo (MC) simulations [*Coleman and Dwyer*, 2006]). The number of produced bremsstrahlung photons can then be determined by multiplying the number of electrons (equation (5)) by a factor $\alpha(\varepsilon_{th})\tau(E)$:

$$N_\gamma = \alpha(\varepsilon_{th})\tau(E) N_0 \exp(t/\tau(E)), \tag{8}$$

where we assume that $t >> \tau(E)$, α is the bremsstrahlung coefficient, $\tau(E)$ is the avalanche growth time of RREAs, and N_0 is the number of initial seed electrons (see Appendix B for a derivation of the bremsstrahlung photon to runaway electron ratio).

In a review of terrestrial gamma ray flashes, which includes comparisons of studies concerning RREAs, *Dwyer et al.* [2012] present the electron energy spectrum. If the initial number of cosmic ray seed electrons is N_0, the total number of electrons in the RREA at the end of the avalanche region is given by equation (4). We can then find the change $dN(z)$ over a distance dz, and by rewriting equation (1) to $dz = d\varepsilon/(eE - F_d)$, we then derive the electron energy distribution function (EEDF) after a few avalanche lengths, or the number of runaway electrons per unit energy,

$$f_{re} = \frac{dN_{RREA}(\varepsilon)}{d\varepsilon} = \frac{N_{RREA}}{7.3\,\text{MeV}} \exp(-\varepsilon/7.3\,\text{MeV}), \tag{9}$$

where 7.3 MeV is the mean energy of RREA EEDF obtained from MC results by *Dwyer et al.* [2012]. This equation also shows that we should expect the energy distribution to follow the exponential cut-off

AGU Journal of Geophysical Research: Space Physics 10.1002/2014JA020504

$\exp(-\varepsilon/7.3\,MeV)$. In Appendix A, we give a complete derivation of the energy spectrum using the mean energy found from GEANT4 simulations.

In Appendix B we express the X-ray fluence distribution $f_\gamma(\varepsilon_\gamma)$ (equation (B1)) by the bremsstrahlung differential cross section $\frac{d\sigma_\gamma}{d\varepsilon_\gamma}(\varepsilon_{re}, \varepsilon_\gamma)$. We then show that the ratio of photons to electrons $N_\gamma(\varepsilon_{th})/N_{re}(\varepsilon_{th})$ can be expressed analytically by the ratio of the respective fluence distributions or by the bremsstrahlung coefficient $\alpha(\varepsilon_{th})$ and avalanche time $\tau(E)$, where the differential bremsstrahlung cross section integrated from the lower energy threshold of integration of the electrons ε_{th} to infinity. In order to find the amount of electrons required to produce a given flux of photons, we can determine $\alpha(\varepsilon_{th})$ and $\tau(E)$ empirically from simulation results.

1.3. Feedback

As previously explained, MC modeling has been used to explain the observations by the RHESSI and BATSE satellites. Results have indicated that between 10^{14} and 10^{17}, runaway electrons are required to produce a TGF, assuming a production altitude of 15 km and that the ratio of bremsstrahlung photons to electrons is roughly 1. According to *Carlson et al.* [2008], we can assume that cosmic rays produce a maximum seed population of 10^6 energetic electrons. Furthermore, we can expect an electric potential of 100 MV to be available in a large thundercloud, which would roughly correspond to 100 MV/7.3 MV = 13.9 avalanche lengths or a maximum multiplication $e^{13.9} \approx 10^6$ runaway electrons per seed electron. Combining this we get a multiplication of 10^{12}, which is 5 orders of magnitude lower than the required number of electrons from an average RHESSI TGF produced at 15 km altitude. In addition, *Dwyer* [2008] made calculations on the initiation of RREAs from extensive air showers (EAS) and steady state background radiation, both mainly a product of cosmic rays. He found that neither of them is very likely to explain TGFs by its own. Thus, the high number of electrons required to produce a TGF cannot be explained by RREA multiplication alone. In response to this, two leading theories have been presented. *Dwyer* [2003] suggested that the feedback mechanism could provide further multiplication and thus explain the production of TGFs. Another possible solution has been presented by *Celestin and Pasko* [2011]. They show that seed electrons with energies on the order of 60 keV can be produced in the vicinity of the tips of lightning leaders by streamers and be further accelerated in the potential drops in front of lightning leader tips. They found that this process was capable of producing 10^{17} energetic electrons. In this paper, we will only examine the feedback mechanism as modeled by GEANT4.

During the initial avalanche, electrons traveling upward in the opposite direction of the electric field will produce many energetic bremsstrahlung photons. Some of these photons will either Compton backscatter or produce pairs of electrons and positrons. If the backscattered photons produce additional runaway electrons, through Compton scattering or photoelectric absorption, inside the strong electric field, they can initiate secondary avalanches. If pair production occurs and positron-electron pairs are produced, the positrons will quickly accelerate downward along the electric field, in the opposite direction of the electrons. If the positrons travel without annihilating, they may also initiate secondary avalanches through electron by positron elastic scattering (Bhabha scattering).

Due to the alignment of the electric field and the low probability of particle interaction, only positrons or photons can backscatter and initiate secondary avalanches. The two mechanisms responsible for feedback are called X-ray feedback and positron feedback, depending on the backscattered particle. In addition, secondary effects such as the products of positron annihilation or bremsstrahlung photons emitted from backscattering positrons, also have an effect [see *Dwyer*, 2007] but will not be distinguished from the primary feedback processes in this paper.

In *Dwyer* [2003], feedback multiplication was quantified by the feedback factor γ. The feedback factor describes the rate at which RREAs are multiplied. The relation is given as a common ratio in a geometric series and is derived in Appendix C. For $\gamma < 1$ and a number of avalanches $n \to \infty$, the total number of electrons converges to

$$N_n = N_{re}/(1-\gamma), \tag{10}$$

for $\gamma = 1$,

$$N_n = N_{re} n, \tag{11}$$

AGU Journal of Geophysical Research: Space Physics 10.1002/2014JA020504

and for $\gamma > 1$ and $n >> 1$, the sum can be expressed as

$$N_n = N_{re}\gamma^n. \tag{12}$$

The feedback time τ_{fb} is the average time for runaway electrons and the backward propagating positrons or photons to complete one round trip within the avalanche region [*Dwyer*, 2012]. The total number of electrons produced N_{tot} is then, for $\gamma > 1$, given as

$$N_{tot} = N_{RREA}\gamma^{t/\tau_{fb}} = N_0\gamma^{(t/\tau_{fb})}e^{(t/\tau(E))}, \tag{13}$$

where N_0 is the number of seed electrons, t is the time, and $\tau(E)$ is still the avalanche time [*Dwyer*, 2003]. If γ rises above 1, the electron multiplication process becomes unstable and the number of avalanches will increase exponentially.

2. The Monte Carlo Model

MC modeling has been widely used to test and constrain theoretical models. The RREA process has been studied in great detail [*Gurevich et al.*, 1992; *Lehtinen et al.*, 1999; *Babich et al.*, 2001; *Coleman and Dwyer*, 2006; *Celestin and Pasko*, 2010], the electron multiplication in streamer tip electric fields has also been studied by multiple models [*Celestin and Pasko*, 2010, 2011; *Chanrion and Neubert*, 2010]. However, studies that discuss the feedback process have solely been obtained from the model by *Dwyer* [2003].

The GEANT4 programming toolkit supplies a detailed library of physics processes concerning the interaction of particles with matter and is widely used in particle physics as well as studies in medical and space science [*Geant4 collaboration*, 2012b]. As GEANT4 is a well-established toolkit used for particle interactions, we suggest that it is an ideal candidate to study particle interactions in the atmosphere. Several studies concerning TGF production and propagation through the atmosphere have been compared to GEANT4. For example, *Carlson et al.* [2007] presented a new set of constraints on TGF production and *Østgaard et al.* [2008] used GEANT4 as a reference for comparison of bremsstrahlung emissions. In addition, *Smith et al.* [2010] used GEANT3 for reference of atmospheric absorption of TGF propagation. In this study, we will use the well-established GEANT4 toolkit to study the RREA and the relativistic feedback process.

The RREA process was first presented by *Gurevich et al.* [1992] and has since been studied in great detail. We will use results from these studies as benchmark to examine the accuracy of our simulations. Then, we will use GEANT4 to study the feedback process and the feedback factor to test and validate the results presented by *Dwyer* [2003, 2007, 2012], which to our knowledge has not been validated by independent studies before.

2.1. Physics Lists

GEANT4 has a very wide range of applications covering extremely energetic particle physics in the PeV range to low-energy physics in the hundreds of eV range. Depending on the energy regime in which simulations are performed, GEANT4 provides several models in the form of physics lists, which includes the physics processes that are required (see the physics reference manual for a detailed description [*Geant4 collaboration*, 2012a]). The RREA and the feedback process take place in the 10 keV to 100 MeV energy range. In this energy regime, several models have been validated. This study will compare two physics lists: (1) The standard model (chapter 8 in the Physics Reference Manual) or "the Low- and High-Energy Parameterization" (LHEP) list, which is developed by the Electromagnetic Standard Physics Working Group used for 1 keV to 10 PeV interactions; (2) The Livermore physics model (chapter 9 in the Physics Reference Manual) or "the Low Background Experiment" (LBE) list, which is developed by the Low Energy Electromagnetic Physics Working Group and used for 250 eV to 100 GeV (bremsstrahlung process included down to 10 eV) [*Geant4 collaboration*, 2013a, 2013b, 2012a]. In both lists, all important particle interactions that contribute to ionization of the atmosphere have been included. It also includes pair production, bremsstrahlung, elastic MÃller, and Bhabha scattering with free electrons and Compton scattering.

It should be noted that the previous studies that use GEANT4 have not discussed the use of physics lists. An important result of the present study is that the choice of physics lists has significant effects on the modeling results.

AGU Journal of Geophysical Research: Space Physics 10.1002/2014JA020504

2.2. Simulation Setup

We have modified an MC code developed by the GEANT4 collaboration to model the electron avalanches in air under the influence of a homogeneous electric field. The following geometric and atmospheric composition standards have been used; A cylindrical volume of height $L = 10$ km and a diameter $d = 3000$ km, air consisting of 78.08% nitrogen, 20.95% oxygen, and 0.97% argon at standard sea level pressure and density, $2.684 \cdot 10^{25}$ molecules $/m^3$. The electric field strength is chosen between 300 and 2500 kV/m, which is $\approx$0.1–0.75 E_{cb}. The electric field is extended vertically from a distance $z = 200$ m above the lower boundary of the cylinder to a distance determined from the amount of electron multiplication that occurs. We use the results by *Coleman and Dwyer* [2006] to make an assumption on the rate of multiplication and choose the vertical extension of the electric field to be between 3λ and 10λ according to equation (6). Unless otherwise stated we initiate each simulation with a continuous monoenergetic beam of 500 seed electrons of 1 MeV in the antiparallel direction of the electric field.

2.3. Selection Criteria

To study the RREA process we choose to include all particles that have a momentum along the initial trajectory of the avalanche (forward) $p > 0.0$. This also includes secondary particles produced by forward propagating photons and positrons. Each electron is then tracked and sampled with both time and location. We sample the electrons as they pass through 10 equally spaced screens inside and at the end of the electric field region. In an electric field extending from $z = 200$ m to $z = 400$ m, these screens are positioned at z =(220.0, 240.0, 260.0, 280.0, 300.0, 320.0, 340.0, 360.0, 380.0, and 400.0) m. We also sample the electrons within each $8 \cdot 10^{-11}$ s interval from start to stop of the simulation. The time step of the electrons is accurate to $1 \cdot 10^{-12}$ s.

The feedback mechanism was studied using a different selection method. We tag every electron with a number corresponding to the generation each electron belongs to. The primary generation tag (1) is given to all electrons that pass through the final screen of the electric field region and are identified to be a part of the initial avalanche (see the previous paragraph). As opposed to the selection of RREAs, when studying feedback we store the position, momentum, and kinetic energy of the electrons that are produced from backscattering photons and positrons. These electrons are then supplied as seed electrons, with the stored data as initial conditions, in the next simulation and their secondary particles will in turn be given the second generation tag (2), and so on. With this method we must run one simulation per generation of feedback we wish to study.

3. Results

3.1. RREA Results

The avalanche length must be calculated using only runaway electrons. We use two methods to determine the energy range of the electrons to be included. For the time-dependent selection, we sample all electrons within each $8 \cdot 10^{-11}$ s time interval, from start to stop of the simulation. To only include runaway electrons, we need to determine the lower energy threshold for electrons to be accelerated for each electric field strength. This energy threshold can be determined from the average stopping power (see Figure 1) that is opposed to the electric field. However, electrons are rarely in perfect alignment with the electric field and, thus, the scattering of the electrons must be taken into account. The computation of the actual runaway threshold is fully described by *Lehtinen et al.* [1999]. For an electric field strength of ~436 kV/m, the runaway threshold is $\varepsilon_{th} = 549$ keV, and for an electric field strength of ~3270 kV/m the runaway threshold is $\varepsilon_{th} = 24$ keV [see *Lehtinen et al.*, 1999, Table 2].

For location-dependent simulations, we use a different assumption. Due to collisions and interactions between the electrons and the atmosphere, the electrons with low energy and some in the intermediate energy range (from a few hundred keV to a few MeV) will lose energy and stop before they pass through the screens. The runaway electrons, however, will by definition continue to accelerate and pass through the screens.

The electron multiplication was studied using the standard simulation setup. Simulations were initiated by a monoenergetic beam of 500 seed electrons of 1 MeV. The electrons were then tracked continuously, both in $8 \cdot 10^{-11}$ s time intervals and as they pass through 10 equally spaced screens in the electric field region.

AGU Journal of Geophysical Research: Space Physics 10.1002/2014JA020504

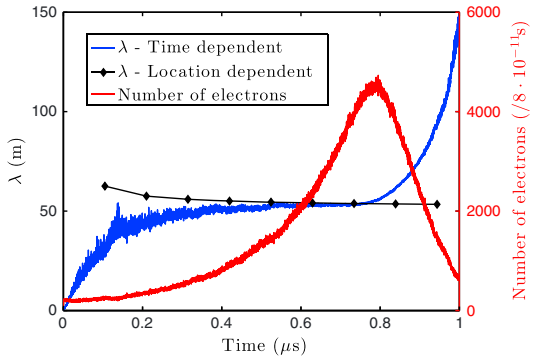

Figure 2. Electron multiplication with time (red line) and the corresponding avalanche lengths λ by time dependency (blue line) and location dependency (black line). The correlation between time and distance is given by the average speed of the developing avalanche of 0.89*c* *Coleman and Dwyer* [2006]. This case was simulated using the LBE physics list.

By rearranging equation (4) we can find the avalanche length as a function of the number of runaway electrons and their location, $N(z)$, or by time intervals, $N(t)$,

$$\lambda(z) = \frac{z}{\ln(N(z)/N_0)}, \qquad \tau(t) = \frac{t}{\ln(N(t)/N_0)} \tag{14}$$

where z and t are the distance and time and N_0 is the number of seed electrons. In Figure 2, we show the exponential increase of runaway electrons with time (red line) and the corresponding avalanche lengths from time-dependant (blue line) and location-dependant (black line) results. Although the selection is done in both time and position, we calculate the avalanche length by distance. For time-dependant simulations the avalanche length is determined by the average position of the electrons in the direction of the electric field. After a few avalanche lengths the RREAs reach a state of steady multiplication were $\lambda(z)$ does not vary with increasing time or distance.

We ran the simulations at intervals of electric field strength of 100 kV/m, between 300 kV/m and 2500 kV/m and then estimated the avalanche length $\lambda(E)$ with respect to the strength of the electric field. The results are shown in Figure 3 as red triangles for the LBE simulations and blue triangles for the LHEP results. The avalanche length obtained from LBE and the LHEP results, valid for 310 kV/m $< E <$ 2500 kV/m, can be fitted respectively by

$$\lambda(E)_{\mathrm{LBE}} = \frac{7400\,\mathrm{kV}}{E - 298.0\,\mathrm{kV/m}} \text{ and } \lambda(E)_{\mathrm{LHEP}} = \frac{9770\,\mathrm{kV}}{E - 285\,\mathrm{kV/m}}, \tag{15}$$

where E is the electric field strength. These functions are shown in Figure 3 (red and blue, respectively) as well as the function presented by *Coleman and Dwyer* [2006], (equation (6) (black line)).

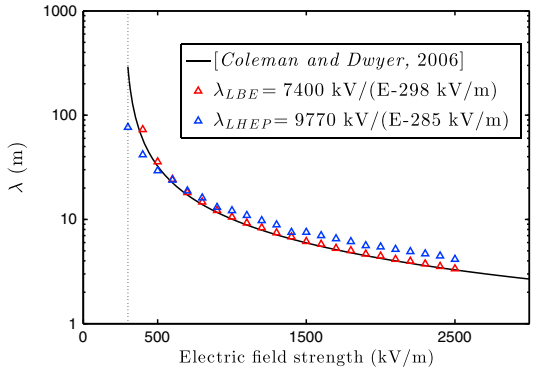

Figure 3. The avalanche length λ with respect to electric field strength. The LBE and LHEP results are marked as red and blue triangles, respectively. The continuous black line follows equation (6), which is the avalanche length determined by *Coleman and Dwyer* [2006]. In addition, the dotted black line marks the minimum electric field threshold E_{th} = 284 kV/m.

Comparing the results obtained from GEANT4 simulations we see that the avalanche lengths from the LBE results agree to within ±5% with the LHEP results at electric fields between 500 and 700 kV/m. At electric fields below 500 kV/m the LBE results tend to give much longer avalanche lengths than the LHEP results, with a maximum of approximately 60%. For stronger electric fields (> 600 kV/m) the difference is on average approximately 25% and the LBE results give shorter avalanche lengths than the LHEP results. By comparing the GEANT4 results to the results by *Coleman and Dwyer* [2006] (equation (6)), we also see that the LBE results which is on average only 5% above the results by Coleman and Dwyer, much closer than the

AGU Journal of Geophysical Research: Space Physics 10.1002/2014JA020504

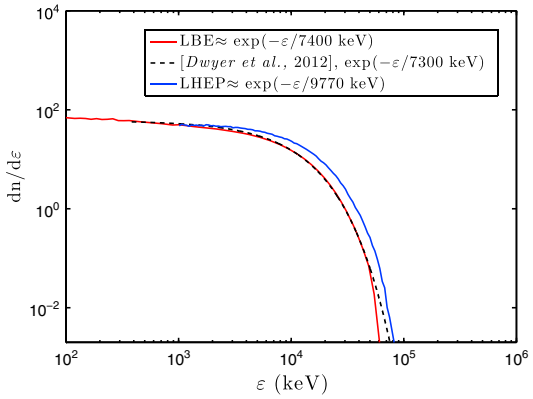

Figure 4. The electron energy distribution from simulations using the LBE physics list (red) and the LHEP physics list (blue). In addition, these results are compared to the exponential function exp($-\varepsilon$/7300) found by *Dwyer et al.* [2012] (dashed black). Note that there is a deviation at very high energies where GEANT4 results do not follow an exponential cutoff.

avalanche length obtained from LHEP simulations, which differ by ±35%. This shows that the explicit production of low-energy electrons and photons used by the LBE physics list provide results closer to the estimates by *Coleman and Dwyer* [2006] than implementing the continuous energy loss functions as by the LHEP physics list.

We also determined the avalanche time, $\tau(E)$, from LBE results,

$$\tau(E) = \frac{27.4\ \text{kV}\,\mu\text{s/m}}{E - 298\ \text{kV/m}} = \frac{\lambda(E)}{0.9c}, \quad (16)$$

which indicates that the average speed of the avalanche is $\approx 0.9c$ and is close to the estimate by *Coleman and Dwyer* [2006] of $0.89c$. This also corresponds with the average distance propagated by the time-dependant simulations. The electron energy distribution function (EEDF) of the runaway electrons was also studied using both the LBE and the LHEP physics lists. Electric fields were chosen at intervals of 50 kV/m between 350 and 500 kV/m and at intervals of 100 kV/m between 500 and 2500 kV/m. The EEDF was calculated using 400,000 electrons at each interval.

Several studies have indicated that the EEDF above a few hundred keV can be described by an exponential cutoff function [*Lehtinen et al.*, 1999; *Celestin and Pasko*, 2010; *Dwyer and Babich*, 2011]. In *Dwyer and Babich* [2011] this cutoff was determined to be best fit by the exponential function exp($-\varepsilon$/7300 keV). In Figure 4, we show the results obtained from the LBE (red line) and LHEP (blue line) physics lists. In addition, the analytical 7300 keV cutoff is indicated as the dashed blue line. The LBE distribution corresponds well with previous estimates and follows an $\approx$ 7400 keV cutoff. However, the LHEP results are again not in agreement and show a much harder cutoff at $\approx$ 9770 keV. Note that in both cases the energy spectrum at very high energies fall off quicker than the exponential function. This is due to data processor limitations, which prevent the distribution to reach a steady state at very high energies due to very large number of particles in the simulations. When the electric field strength is close to the electric field threshold, $\approx$ 300 kV/m < E < 350 kV/m, the distributions have a much softer spectrum. As for the avalanche lengths, the mean energy of the electron distribution is dependent on the energy range of the runaway electrons in the distribution. The two methods gave substantially different results with mean energy of the time-dependant method being approximately 10% lower than the location-dependant method.

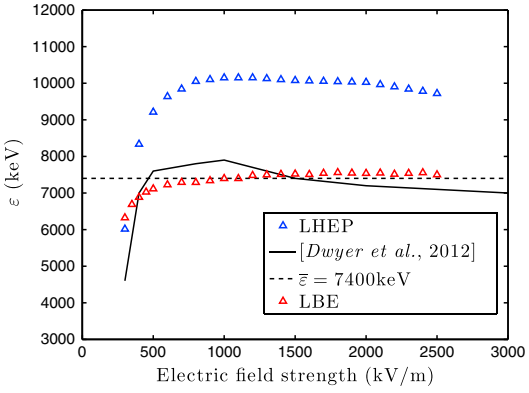

Figure 5. The mean energy of runaway electrons in an RREA with respect to electric field strength. The red and blue triangles again indicate the LBE results and the LHEP results, respectively. They are compared to the continuous black line, which represents the mean energies found by Dwyer [*Dwyer et al.*, 2012, Figure 3]. The dashed line represents, the average mean energy, $\bar{\varepsilon} = 7400$ keV found from LBE results.

AGU Journal of Geophysical Research: Space Physics 10.1002/2014JA020504

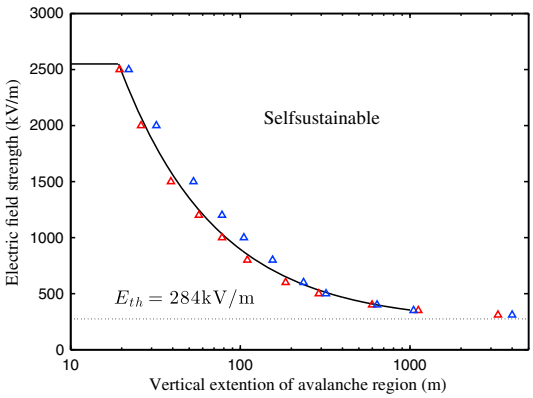

Figure 6. This figure shows the electric field strength versus the vertical extension of the avalanche region. At a given electric field strength, the vertical extent of the avalanche region has an upper limit where the multiplication process becomes self sustainable, and a complete or partial discharge will quickly occur. This limit was determined in *Dwyer* [2003] to be when the feedback factor γ is equal to 1 and is indicated by the continuous black line. The results obtained from LBE and LHEP simulations are indicated by the red and blue triangles, respectively.

We choose to implement the location-dependent selection method as it is similar to the selection method used by *Dwyer* [2004].

The mean energy of the RREA distributions with respect to the electric field strength can be seen in Figure 5. We compare the LBE and the LHEP results to the results presented in *Dwyer and Babich* [2011]. The average energy resulting from LBE simulations, 7400 keV, is in good agreement with the 7300 keV from Dwyers results. This mean energy also corresponds to the best fit to the EEDF and to the avalanche length given by equation (15). The mean energy of LHEP simulations is approximately 9700 keV, which is 33% larger than previous estimates. A difference is also seen for electric fields above $\approx$1200 kV/m, where LBE results are stable close to 7500 keV and LHEP results show a weak decrease from $\approx$10, 200 to 9650 keV. This decrease of mean energy at stronger electric fields is also seen in the results of *Dwyer et al.* [2012].

3.2. Feedback

The feedback factor quantifies the increase or decrease of RREA by the relation between the number of REs in an initial RREA and the sum of REs produced by secondary RREAs. The secondary RREAs are electron avalanches that have been initiated from backscattering photons and positrons from the initial RREA. This relation is derived in Appendix C. In our simulations we store the position, momentum, and kinetic energy of the electrons produced by backscattering photons and positrons from the initial RREA. These data are then used to initiate the secondary avalanches in a separate simulation and again store the third generation seed electrons. For every simulation we also track all electrons passing through a screen at the end of the avalanche region, thus finding the relation between each RREA and its secondaries. We then determine the feedback factor γ or the rate of feedback, using equations (10)–(12).

The feedback mechanism becomes unstable and increases the rate of RREA multiplication exponentially when the feedback factor rises above 1 [*Dwyer*, 2003]. In Figure 6, we show the threshold for the feedback multiplication to become unstable depending on the strength of the electric field and the vertical extension of the avalanche region at sea level density and pressure. The red and blue triangles show the results from the LBE and the LHEP simulations, respectively. For electric fields close to the electric field threshold ($<$ 500 kV/m) the LBE results show that 18% shorter avalanche regions than that in the case of LHEP are required for feedback to become unstable. At 500 kV/m the results are comparable with a difference of $\pm$5%. However, for fields stronger than 500 kV/m the difference quickly rises to 25%, which is considerable. For very strong fields close to the maximum field for feedback to become unstable (2550 kV/m from *Dwyer* [2003], for sea level density and pressure), the difference becomes slightly less pronounced, but still close to 20% longer avalanche regions are required. If we compare these results to those presented in *Dwyer* [2003] (black curve) we see that the LBE results are in good agreement with Dwyers results.

3.3. Photon to Electron Ratio

To study the ratio of the produced bremsstrahlung photons to the energetic electrons in a RREA, we use only the LBE physics list. Every simulation is initiated with a monoenergetic beam of 500 seed electrons of 1 MeV. At each interval of electric field strength, 400, 800, 1200, 1600, and 2000 kV/m, we let the avalanche develop

AGU Journal of Geophysical Research: Space Physics 10.1002/2014JA020504

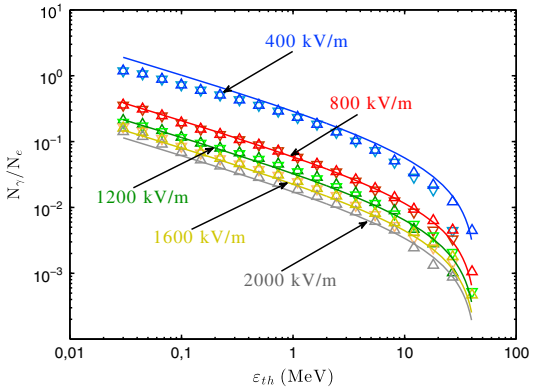

Figure 7. The ratio of bremsstrahlung photons to runaway electrons N_γ/N_e from GEANT4 simulations. The points show the ratio obtained for given electric field strengths, and the brightness indicates the simulated distance of the avalanche, where 5λ is bright and 7λ is dark. The curves follow the analytical expression $N_\gamma/N_e = \alpha(\varepsilon_{\text{th}}) \cdot \tau(E)$, where $\alpha(\varepsilon_{\text{th}})$ is given in equation (17) and $\tau(E)$ is given in equation (16).

over both five and seven avalanche lengths to examine the distributions of electrons and photons at the end of the avalanche regions. We then use equation (B6), with different choices for the energy threshold of integration (ε_{th}) for both electrons and photons to determine N_γ/N_e. Figure 7 shows the ratio N_γ/N_e as a function of the energy threshold of integration. The darker colors signify development over 5λ and the brighter colors over 7λ. A high-energy electron is less likely to transfer a large portion of its energy, through the bremsstrahlung process, to the produced photon. This corresponds to the drop in the photon to electron ratio with higher-energy thresholds. In addition, the ratio decreases with stronger electric fields because the electron multiplication expressed by the avalanche time $\tau(E)$ has a $1/E$ dependency. Another important feature is that the ratio is independent on the lifetime of the avalanche once steady state of the EEDF is reached. This is seen as the darker (5λ) points near perfectly overlap the brighter (7λ) points. However, this is not seen for very high energy thresholds of integration and this can be due to the relatively low number of electrons and photons in this energy range.

By rearranging equation (8) the bremsstrahlung production coefficient α can be expressed in terms of the ratio N_γ/N_e and the avalanche time $\tau(E)$ (see Appendix B for a full derivation). As the ratio N_γ/N_e and $\tau(E)$ are equally dependent on the electric field, α loses this dependency and is only dependent on the energy threshold ε_{th}. To determine α we then multiply the simulation results for N_γ/N_e by the avalanche time $\tau(E)$ for the respective electric fields. The bremsstrahlung coefficient $\alpha(\varepsilon_{\text{th}})$, with respect to the energy thresholds of integration ε_{th}, valid for 0.1 MeV $< \varepsilon_{\text{th}} <$ 60.0 MeV, is found empirically to follow:

$$\alpha(\varepsilon_{\text{th}}) = \frac{1.258\ \left[\text{MeV}^{1/2}\ \mu\text{s}^{-1}\right]}{\sqrt{\varepsilon_{\text{th}}}} - 0.1874\ [\mu\text{s}^{-1}] \qquad (17)$$

where ε_{th} is the energy threshold of integration in equation (B6) given in MeV and $\alpha(\varepsilon_{\text{th}})$ is given in μs^{-1}. The results are shown in Figure 8 where the colored triangles show the ratio N_γ/N_e obtained from simulation results multiplied by the avalanche length $\tau(E)$ and the solid black curve is $\alpha(\varepsilon_{\text{th}})$ from equation (17). To confirm the result we also plot the ratio expressed by $\alpha(\varepsilon_{\text{th}}) \cdot \tau(E)$ on top of the simulation results in Figure 7 and find that the results are in agreement.

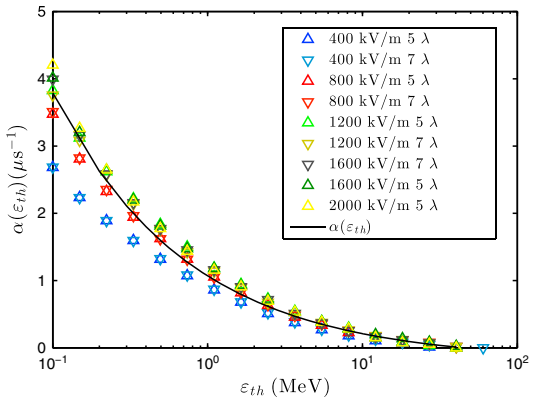

Figure 8. The bremsstrahlung coefficient $\alpha(\varepsilon_{\text{th}}) = (N_\gamma/N_e)/\tau(E)$ as a function of the energy threshold of integration ε_{th}. The colored triangles indicate the results from simulations for given energy boundaries, but for different electric field strengths and the continuous black line is the best fit function (equation (17)). In addition, for each electric field strength the brighter color indicates a simulated distance of 5λ and the darker color 7λ.

AGU Journal of Geophysical Research: Space Physics 10.1002/2014JA020504

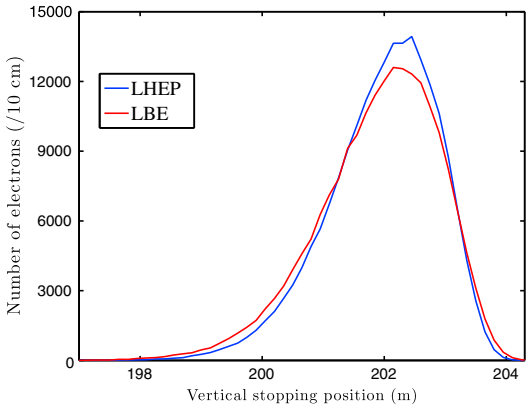

Figure 9. The stopping position of 50,000 electrons of 1 MeV per 10 cm without the influence of an electric field. The LBE results are indicated by the red color, and the LHEP results are indicated by the blue color. Note that the initial vertical position of the electrons is at 200 m.

For a lower energy threshold of integration equal to 1 MeV, the ratio N_γ/N_e is found to be 0.23 for an electric field strength of $E = 400$ kV/m. For stronger electric fields, between 800 and 2000 kV/m, we find that the ratio is roughly in the range 0.1–0.01. This indicate that if TGFs are produced in very strong electric fields, as a result of the feedback mechanism, the required number of electrons at the source is 1–2 order of magnitude higher than the number of photons. However, if TGFs are produced in weaker electric fields close to the lower electric field threshold (284 kV/m), the ratio of bremsstrahlung photons to electrons become closer to 1.

4. Discussion

4.1. Physics List Comparison

An important result obtained from the GEANT4 MC simulations is the significant difference found by using the LBE or LHEP physics list. Although both lists have been validated in the energy range we have studied, the results are substantially different. The main difference between these two physics lists is the implementation of the continuous and discrete energy losses of electrons and positrons due to ionization and bremsstrahlung. When using the LHEP list, the energy loss function is introduced for energies below 1 keV. However, while using the LBE list, the energy loss function is introduced below 250 eV for ionization and below 10 eV for bremsstrahlung. Above these thresholds the energy loss is simulated explicitly through the production of photons, electrons, and positrons. In addition, the cross sections in the LBE physics list make direct use of shell cross-section data [*Geant4 collaboration*, 2012a]. The cross sections in the LHEP physics list does not take the shell cross-section data into account. It is clear from these differences that the LBE physics list contains more accurate descriptions of low-energy interactions, in particular, between 250 eV and 1 keV.

To determine the effect of theses differences on the energy loss of the electrons, we initiated a continuous monoenergetic beam of 50,000 electrons of 1 MeV at a vertical position of 200 m without the influence of an electric field. We then found the vertical stopping position of each individual electron. The result is shown in Figure 9. On average, the electrons in the case of the LHEP simulations make it further than in the case of the LBE simulations. The mean stopping position of electrons is 10 cm (4%) further in the LHEP case as compared with the LBE case. We can infer from this that less energy is lost on average as a result of the continuous loss functions by the LHEP simulations as compared to the LBE simulations.

In section 3.1, our results show that the avalanche length on average is 25% longer for strong electric fields and 60% longer close to the electric field threshold. In addition, as less energy is lost through interactions with low energy particles when using the LHEP list, the mean energy of the RREA electron distribution becomes correspondingly larger (see Figure 5). The mean difference was shown to be $\approx$ 32% larger.

From the comparisons between our results and the previous results from independent MC models, we can conclude that it is likely that the LBE physics list is more accurate when studying RREAs and feedback. In fact, results obtained from simulations using the standard LHEP model greatly underestimate the energy loss and electron multiplication of RREAs.

4.2. RREA

The avalanche length or rate of runaway electron multiplication, the mean energy, and the electron energy distribution function (EEDF) are key features necessary to discuss in order to validate GEANT4 as a tool

AGU Journal of Geophysical Research: Space Physics 10.1002/2014JA020504

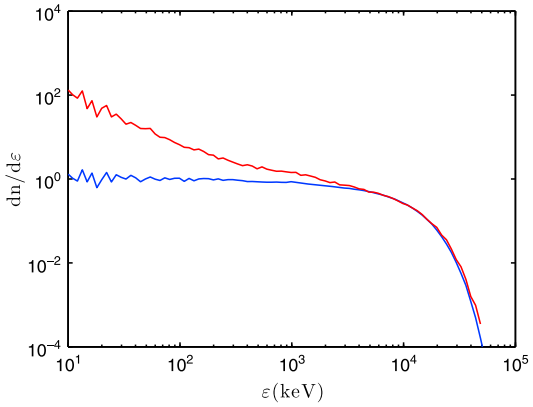

Figure 10. The energy distribution of RREAs simulated in an electric field of 400 kV/m. The red graph indicates the time-dependent simulation results, and the blue graph indicates the distance-dependent results.

to simulate RREAs. In section 3.1 we discuss the use of a location- or time-dependent selection method and find that the simulation results are different depending on which method we implement. In order to determine the extent of the difference between the two methods, we compare the corresponding normalized spectra obtained. This can be seen in Figure 10. At higher energies the time-dependent (red) and location-dependent (blue) results match perfectly. At lower energies, however, the location-dependent selection method includes only the fraction that managed to run away and pass through the screen at which position they are sampled. The time-dependent selection method acts as a camera, taking a snapshot of the system that then includes all low-energy electrons that are free at that particular moment.

For the purpose of studying the EEDF and the mean energy of RREAs we choose to define the runaway electrons as all electrons that are accelerated by the electric field. By this definition the location-dependent method directly samples all runaway electrons, as all the REs are accelerated through the final screen of the avalanche region. The time-dependent method, however, includes many low-energy electrons and some intermediate-energy electrons that will eventually stop due to interactions and collisions, which will result in a 10% lower mean energy even if the runaway energy threshold is taken into account.

Coleman and Dwyer [2006] found that the exponential growth of runaway electrons in a RREA could be well described by equation (6). This is also supported by a comparison with independent results from several authors [*Dwyer et al.*, 2012]. The results obtained from GEANT4 modeling, using the LBE physics list, are also in very good agreement with previous studies. The difference between our results and equation (6) is less than 5% for weak electric field strengths ($<$ 600 kV/m) and less than 3% for stronger electric fields (600–2500 kV/m).

In order to study the RREAs in more detail we also compared the mean energy and the EEDFs to existing results. The mean energy of electrons in a RREA can be expressed as the net energy gained over one avalanche length by the electric field and lost by the friction force of the atmosphere. In a homogeneous electric field at sea level pressure and density, the mean energy and the energy distribution of RREAs reach a steady state after a few avalanche lengths. The total mean energy in this steady state, averaging over all electric field strengths between 300 and 2500 kV/m, was found to be $\overline{\varepsilon}_{\mathrm{LBE}} \simeq 7400$ keV. This is in very good agreement with previous estimates of $\overline{\varepsilon} = 7300$ keV by *Dwyer et al.* [2012]. However, a detailed comparison shows that for weak, 300–600 kV/m, and strong, 1300–2500 kV/m, electric fields, the mean energy is slightly higher than previous results. While in the intermediate range, 600–1300 kV/m, the mean energy is slightly lower. In other words the total mean energy is in good agreement, but shows less variations with the strength of the electric field.

From results presented in *Dwyer and Babich* [2011], we expected the EEDF to follow an exponential cutoff $\exp(-\varepsilon/\overline{\varepsilon})$, where ε is the energy of the electrons and $\overline{\varepsilon}$ is the average mean energy of RREAs. As expressed in the previous paragraph we found the total mean energy to be $\overline{\varepsilon}_{\mathrm{LBE}} \simeq 7400$ keV. Using the location-dependent method of simulation, we calculated the cutoff above 500 keV and found that the EEDF was best fit by the exponential function $\exp(-\varepsilon/7440\ \mathrm{keV})$, which is close to the expected value. For energies above $\approx$ 50 MeV, the energy distribution falls off slightly faster and no longer follows the exponential cutoff. However, the limitations of data handling of extremely large number of particles make the number

AGU Journal of Geophysical Research: Space Physics 10.1002/2014JA020504

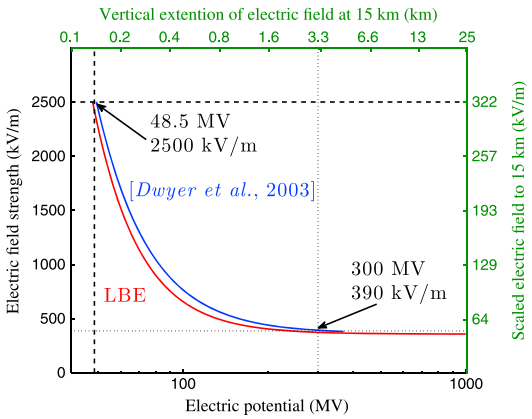

Figure 11. The feedback threshold expressed by the electric field strength and the corresponding electric potential. The LBE results (red) are in good agreement with the estimates from *Dwyer* [2003] (blue). The minimum potential required for feedback to become self sustainable is determined to be at 48.5 MV and at 2500 kV/m (dashed line). Very large thunderstorms are believed to produce electric potential differences on the order of 300 MV, which would require a minimum electric field strength of 390 kV/m (dotted line). The green *x* and *y* axes show the electric field strength and corresponding vertical extension scaled to 15 km altitude.

density of electrons with energies in the several tens of MeV range low. This may influence the spectrum and make it difficult to obtain a distribution that is in steady state at very high energies.

This shows that our model is well equipped to simulate RREAs in a homogeneous electric field with strength close to the conventional breakdown field, $E_{cb} = 3200$ kV/m. If the electric field strength becomes larger than the critical breakdown field, electrons with energies lower than the runaway threshold become important and the LBE physics list may then become insufficient. These results are therefore important in terms of validating GEANT4 MC simulations as an important tool to study RREAs. However, as we have shown, the implementation of the physics lists is crucial in order to obtain accurate results.

4.3. Feedback

An important subject of this paper is to test the effect of the feedback process on electron multiplication during RREA development in Earth's atmosphere. To do this we wish to find the conditions required for the feedback process to become self sustainable ($\gamma > 1$). The primary conditions to push the feedback factor, γ, above 1 were defined in *Dwyer* [2003] to be the strength of the electric field and its vertical extension. As shown in Figure 6, the results obtained with LBE simulations are in very good agreement with the conditions presented by *Dwyer* [2003], in particular, for weak electric fields close to the electric field threshold.

At the production altitude of TGFs ($\approx$ 15 km), the electric field must be scaled by the atmospheric density. However, the electric potential required to accelerate and multiply the REs remains constant. Figure 11 shows the feedback threshold expressed by the electric field strength and the corresponding electric potential. In addition, we show the electric field strength and the corresponding vertical extension scaled to 15 km altitude on the green *x* and *y* axes, respectively. *Dwyer* [2003] estimated that this potential must be on the order of 50 MV and increasing with weaker electric fields to several hundred Mega Volts. GEANT4 simulations confirm these results. We have estimated that an electric potential of 48.5 MV (19.4 m) at an electric field strength of 2500 kV/m to $\approx$ 300 MV (~770 m) at 390 kV/m is required.

Typical thunderstorms have electric potential differences of up to 100 MV [*Carlson et al.*, 2009]; however, it has been proposed that larger storms may produce potential differences in the order of 300 MV. Balloon soundings through thundercloud systems measured maximum potential differences in IC regions to be in the range of 40–130 MV [*Marshall and Stolzenburg*, 2001]. This is above the feedback potential thresholds found for electric field strengths of 400–2500 kV/m (270–48.5 MV). However, for the feedback mechanism to be self sustainable, these potential differences must be limited to local regions of the thundercloud in order to sustain the relatively strong electric fields. Marshall and Stolzenburg concluded that, although they measured maximum electric fields of only one third of the conventional breakdown threshold, such strong electric fields appear in relatively small regions and have very short lifetimes.

From GEANT4 simulations we can confirm the results presented by Dwyer and also conclude that it cannot be ruled out that the feedback mechanism play a role in the production of TGFs given the right conditions.

AGU Journal of Geophysical Research: Space Physics 10.1002/2014JA020504

4.4. Photon to Electron Ratio

The ratio of bremsstrahlung photons to electrons is important to determine the amount of electrons required to produce a TGF. In Figure 8, we show that $\alpha(\varepsilon_{th})$ depends weakly on the strength of the electric field and can be expressed as a function of the energy threshold of integration. Furthermore, we show (see also Appendix B) that the ratio of bremsstrahlung photons to runaway electrons for a given electric field strength, can be expressed by

$$\frac{N_\gamma}{N_e} = \alpha(\varepsilon_{th})\tau(E), \tag{18}$$

where $\tau(E)$ and $\alpha(\varepsilon_{th})$ are given in equations (16) and (17) and ε_{th} is the energy threshold of integration of electrons and photons.

This threshold can be determined by relating the force exerted on the electrons by the electric field to the friction force experienced by electrons with a given energy (Figure 1). The intersection between the two forces will give the average minimum energy required for an electron to be runaway. Using this energy as the energy threshold of integration will give an approximation of the expected photon to electron ratio. For an electric field of 400 kV/m, where the energy threshold of integration is estimated to be $\approx$ 549 keV by *Lehtinen et al.* [1999] and *Celestin and Pasko* [2010], the photon to electron ratio is roughly 0.8. When the electric fields become stronger, although the energy threshold of integration becomes lower, the ratio becomes closer to 0.1. These results are in good agreement with the general assumption of 1 to 0.1 photon to electron source ratio.

5. Conclusion

1. GEANT4 is widely used as a toolkit to validate modeling results. However, the use of different physics lists has not been discussed in previous studies concerning the production of TGFs. We have shown that the choice of physics list is crucial to obtain correct results.
2. We have obtained the first detailed results concerning the RREA process using GEANT4. The LBE physics list (Livermore model) provides results that are in very good agreement with previous studies. As results concerning RREAs are well established, our results are important to validate GEANT4 as a toolkit to study electron multiplication in the Earth's atmosphere.
3. This paper also presents the first independent study of the feedback mechanism presented in *Dwyer* [2003]. Our results confirm the results presented by *Dwyer* [2003] and constrain the conditions under which the feedback mechanism may play a role in the production of high-energy particles in thunderstorms.
4. The ratio of bremsstrahlung photons to runaway electrons N_γ/N_{re} in electric fields between 400 and 2000 kV/m was found to be between 1 and 0.1. This can be calculated using the analytical expression presented in equation (18), where the bremsstrahlung coefficient $\alpha(\varepsilon_{th})$ has been determined empirically from GEANT4 simulations and is given in equation (17).

Appendix A: The Energy Distribution of RREAs

To find the energy distribution of the RREA electrons, we start by restating the avalanche length of a RREA in an electric field of strength between 310 kV/m $< E <$ 2500 kV/m from equation (15)

$$\lambda = \frac{7400\ \text{keV}}{eE - F_d} \tag{A1}$$

where 7400 keV is the mean energy of the runaway electrons in a RREA determined from our Monte Carlo simulations. *Gurevich et al.* [1992] showed that the number of runaway electrons in one avalanche increases with time t and distance z and can be expressed by distance as

$$\frac{dN}{dz} = \frac{1}{\lambda}N, \tag{A2}$$

where N is the number of electrons at a given distance z from the start of the avalanche. We then integrate equation (A2) from the number of seed electrons at the start of an avalanche N_0 to the total number of electrons N_{RREA} at the end of the avalanche region L and get

$$\int_{N_0}^{N_{RREA}} \frac{dN}{N} = \int_0^L \frac{dz}{\lambda}. \tag{A3}$$

AGU Journal of Geophysical Research: Space Physics 10.1002/2014JA020504

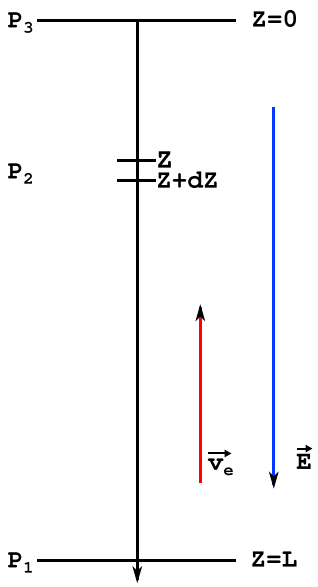

Figure A1. A schematic representation of a system where the electrons move with a velocity $\vec{v_e}$ in an electric field $\vec{E}$ and thus creating an avalanche in the region from $Z = 0$ to $Z = L$. Three points of interest are also marked in the figure as points P_1, P_2, and P_3.

The total number of particles produced in a RREA is then given by

$$N_{\mathrm{RREA}} = N_o \exp\left(\int_0^L \frac{dz}{\lambda}\right) = N_o \exp\left(\frac{L}{\lambda}\right). \quad \text{(A4)}$$

Figure A1 shows a schematic representation of the system used to derive the energy distribution. If we have a given number of seeding electrons N_0 at position P_1 at the start of the avalanche region $Z = L$ (Note that we have a positive direction along the electric field, and thus the avalanche develops in the negative direction). The number of runaway electrons at point P_2 at a distance Z from the start of the avalanche is then

$$N(Z) = N_0 \exp\left(\frac{L-Z}{\lambda}\right). \quad \text{(A5)}$$

The number of electrons moving a distance dZ from $Z + dZ$ to Z is given by deriving equation (A5):

$$-\frac{dN(Z)}{dZ} = -\frac{N_0}{\lambda}\exp\left(\frac{L-Z}{\lambda}\right). \quad \text{(A6)}$$

The negative sign is due to moving in the negative direction from $Z + dZ$ to Z. The change in the number of electrons with respect to distance is then

$$dN(Z) = N_0 \exp\left(\frac{L-Z}{\lambda}\right)\frac{dZ}{\lambda} \quad \text{(A7)}$$

The average kinetic energy gained by an electron moving a distance Z in an electric field E is given by

$$\varepsilon = Z(eE - F_d) \quad \text{(A8)}$$

where F_d is the friction force experienced by the electron and is $\approx$ 218 keV/m. Rearranging equation (A8) gives us

$$Z = \frac{\varepsilon}{eE - F_d}. \quad \text{(A9)}$$

We then assume that the avalanche length can be described as

$$\lambda = \frac{7400\ \mathrm{keV}}{eE - F_d}, \quad \text{(A10)}$$

where the average electron energy 7400 keV is obtained empirically from LBE simulations. Dividing equation (A9) with equation (A10)

$$\frac{Z}{\lambda} = \frac{\varepsilon}{7400\ \mathrm{keV}} \quad \text{(A11)}$$

and then by derivation we see that

$$\frac{dZ}{\lambda} = \frac{d\varepsilon}{7400\ \mathrm{keV}}. \quad \text{(A12)}$$

Inserting equations (A11) and (A12) in equation (A7), we change dependence from distance Z to electron energy ε

$$dN(\varepsilon) = N_0 \exp\left(\frac{L}{\lambda} - \frac{\varepsilon}{7400\ \mathrm{keV}}\right)\frac{d\varepsilon}{7400\ \mathrm{keV}} \quad \text{(A13)}$$

or in terms of N_{RREA}

$$dN(\varepsilon) = \frac{N_{\mathrm{RREA}}}{7400\ \mathrm{keV}} \exp\left(-\frac{\varepsilon}{7400\ \mathrm{keV}}\right) d\varepsilon. \quad \text{(A14)}$$

The energy distribution or the number of runaway electrons per unit energy is then

$$N_{\mathrm{re}} = \frac{dN(\varepsilon)}{d\varepsilon} = \frac{N_{\mathrm{RREA}}}{7400\ \mathrm{keV}} \exp\left(-\frac{\varepsilon}{7400\ \mathrm{keV}}\right). \quad \text{(A15)}$$

AGU Journal of Geophysical Research: Space Physics 10.1002/2014JA020504

Appendix B: The Bremsstrahlung Coefficient

The X-ray source spectrum f_γ can be expressed by

$$f_\gamma(\varepsilon_\gamma) = N_n \int f_{\mathrm{re}}(\varepsilon_{\mathrm{re}}) \frac{\mathrm{d}\sigma_\gamma}{\mathrm{d}\varepsilon_\gamma}(\varepsilon_{re}, \varepsilon_\gamma) v(\varepsilon_{\mathrm{re}}) \mathrm{d}\varepsilon_{\mathrm{re}}, \tag{B1}$$

where N_n is the neutral gas density, $f_{\mathrm{re}}(\varepsilon_{\mathrm{re}})$ is the electron fluence distribution, $\mathrm{d}\sigma_\gamma/\mathrm{d}\varepsilon_\gamma$ is the differential bremsstrahlung cross section and $v(\varepsilon_{\mathrm{re}})$ is the velocity of electrons with energy $\varepsilon_{\mathrm{re}}$.

In Appendix A, the EEDF was shown analytically to follow an exponential cutoff. If the avalanche has developed sufficiently and is in steady state, the resulting X-ray spectrum $f_\gamma(\varepsilon_\gamma)$ does not depend on time. The ratio of the number photons to the number of runaway electrons then depend on the runaway electron multiplication as a function of electric field strength E by $\tau(E)$, which is the avalanche time, and on the bremsstrahlung coefficient α integrated over all energies, and can be expressed by

$$\frac{N_\gamma(\varepsilon_{\mathrm{th}})}{N_{\mathrm{re}}(\varepsilon_{\mathrm{th}})} = \alpha(\varepsilon_{\mathrm{th}})\tau(E) = \frac{\int_{\varepsilon_{\mathrm{th}}}^{+\infty} f_\gamma(\varepsilon_\gamma)\mathrm{d}\varepsilon_\gamma}{\int_{\varepsilon_{\mathrm{th}}}^{+\infty} f_{\mathrm{re}}(\varepsilon_{\mathrm{re}})\mathrm{d}\varepsilon_{\mathrm{re}}}, \tag{B2}$$

$$= \frac{N\int_{\varepsilon_{\mathrm{th}}}^{+\infty}\int_{\varepsilon_{\mathrm{th}}}^{+\infty} f_{\mathrm{re}}(\varepsilon_{\mathrm{re}})\frac{\mathrm{d}\sigma_\gamma}{\mathrm{d}\varepsilon_\gamma}(\varepsilon_{\mathrm{re}}, \varepsilon_\gamma) v(\varepsilon_{\mathrm{re}})\mathrm{d}\varepsilon_{\mathrm{re}}\mathrm{d}\varepsilon_\gamma}{\int_{\varepsilon_{\mathrm{th}}}^{+\infty} f_{\mathrm{re}}(\varepsilon_{\mathrm{re}})\mathrm{d}\varepsilon_{\mathrm{re}}}, \tag{B3}$$

$$= \frac{N\int_{\varepsilon_{\mathrm{th}}}^{+\infty} f_{\mathrm{re}}(\varepsilon_{\mathrm{re}})v(\varepsilon_{\mathrm{re}})\int_{\varepsilon_{\mathrm{th}}}^{+\infty}\frac{d\sigma_\gamma}{\mathrm{d}\varepsilon_\gamma}(\varepsilon_{\mathrm{re}}, \varepsilon_\gamma)\mathrm{d}\varepsilon_{\mathrm{re}}\mathrm{d}\varepsilon_\gamma}{\int_{\varepsilon_{\mathrm{th}}}^{+\infty} f_{\mathrm{re}}(\varepsilon_{\mathrm{re}})\mathrm{d}\varepsilon_{\mathrm{re}}}, \tag{B4}$$

where $\varepsilon_{\mathrm{th}}$ is the lower energy threshold of integration of the electrons. We then let

$$\xi(\varepsilon_{\mathrm{re}}, \varepsilon_{\mathrm{th}}) = N_n v(\varepsilon_{\mathrm{re}}) \int_{\varepsilon_{\mathrm{th}}}^{+\infty} \frac{\mathrm{d}\sigma_\gamma}{\mathrm{d}\varepsilon_\gamma}(\varepsilon_{\mathrm{re}}, \varepsilon_\gamma)\mathrm{d}\varepsilon_\gamma, \tag{B5}$$

and finally express the ratio of the number of photons to the number of electrons by

$$\frac{N_\gamma(\varepsilon_{\mathrm{th}})}{N_{\mathrm{re}}(\varepsilon_{\mathrm{th}})} = \alpha(\varepsilon_{\mathrm{th}})\tau(E) = \frac{\int_{\varepsilon_{\mathrm{th}}}^{+\infty} f_{\mathrm{re}}(\varepsilon_{\mathrm{re}})\xi(\varepsilon_{\mathrm{re}}, \varepsilon_{\mathrm{th}})\mathrm{d}\varepsilon_{\mathrm{re}}}{\int_{\varepsilon_{\mathrm{th}}}^{+\infty} f_{\mathrm{re}}(\varepsilon_{\mathrm{re}})\mathrm{d}\varepsilon_{\mathrm{re}}}. \tag{B6}$$

Using equation (B6) and the avalanche multiplication $\tau(E)$ by equation (16), we can express the bremsstrahlung coefficient by

$$\alpha(\varepsilon_{\mathrm{th}}) = \frac{N_\gamma(\varepsilon_{\mathrm{th}})}{N_{\mathrm{re}}(\varepsilon_{\mathrm{th}})}\frac{1}{\tau(E)} = \frac{N_\gamma}{N_e}\frac{E - 298\,\mathrm{kV/m}}{27.4\,\mathrm{kV\,\mu s/m}}, \tag{B7}$$

where E is the strength of the electric field.

Appendix C: The Feedback Factor

If N_n is the total number of electrons produced after n number of secondary avalanche multiplications, the feedback factor γ is given as the relation between the total number of electrons in the nth and nth $-$ 1 avalanche

$$\gamma = \frac{N_n}{N_{n-1}}. \tag{C1}$$

We can then express the total number of electrons at the end of the avalanche as the sum of a geometric series using the number of electrons produced in the initial RREA N_{re} and the feedback factor γ

$$N_n = N_{\mathrm{re}} + N_{\mathrm{re}}\gamma + N_{\mathrm{re}}\gamma^2 + \ldots + N_{\mathrm{re}}\gamma^{n-1}, \qquad n = 1, 2, 3, \ldots \tag{C2}$$

$$\gamma N_n = N_{\mathrm{re}}\gamma + N_{\mathrm{re}}\gamma^2 + \ldots + N_{\mathrm{re}}\gamma^{n-1} + N_{\mathrm{re}}\gamma^n. \tag{C3}$$

AGU Journal of Geophysical Research: Space Physics 10.1002/2014JA020504

We now get the sum of the nth partial sum by subtracting these two equations,

$$(1-\gamma)N_n = N_{\mathrm{re}}(1-\gamma^n), \tag{C4}$$

and for $\gamma \neq 1$ we get

$$N_n = \frac{N_{\mathrm{re}}(1-\gamma^n)}{1-\gamma}. \tag{C5}$$

If $\gamma < 1$ and $n \to \infty$, the total number of electrons converges to

$$N_n = \lim_{n\to\infty} \frac{N_{\mathrm{re}}(1-\gamma^n)}{(1-\gamma)} = \frac{N_{\mathrm{re}}}{1-\gamma}. \tag{C6}$$

If $\gamma = 1$, the sum can be calculated by using l'Hôpital's rule. We then get

$$N_n = \lim_{\gamma\to 1} \frac{N_{\mathrm{re}}(1-\gamma^n)}{(1-\gamma)} \left[\frac{0}{0}\right] = \lim_{\gamma\to 1} \frac{\frac{\mathrm{d}}{\mathrm{d}\gamma} N_{\mathrm{re}}(1-\gamma^n)}{\frac{\mathrm{d}}{\mathrm{d}\gamma}(1-\gamma)} = N_{\mathrm{re}} n, \tag{C7}$$

which is obvious. If $\gamma \geq 1$ and $n \to \infty$, the sum diverges to infinity since $\lim_{n\to\infty} \gamma^n = \infty$. If $\gamma > 1$ for large n, the sum can be expressed as

$$N_n = N_{\mathrm{re}} \gamma^n. \tag{C8}$$

Acknowledgments

This study was supported by the European Research Council under the European Union's Seventh Framework Programme (FP7/2007-2013)/ERC grant agreement 320839 and the Research Council of Norway under contracts 208028/F50, 216872/F50, and 223252/F50 (CoE). S. Celestin's research is supported by the French Space Agency (CNES) through a Chair of Excellence and the satellite mission TARANIS. The results in this paper are produced by simulations using GEANT4. GEANT4 version 9.6 is available for download at the official GEANT4 support web page (http://geant4.cern.ch/support/source_archive.shtml). The scripts used to set up and run the simulations can be obtained by contacting Alexander Broberg Skeltved by e-mail (Alexander.Skeltved@ift.uib.no).

Alan Rodger thanks the reviewers for their assistance in evaluating this paper.

References

Babich, L., E. Donskoy, I. Kutsyk, A. Kudryavtsev, R. Roussel-Dupre, B. Shamraev, and E. Symbalisty (2001), Comparison of relativistic runaway electron avalanche rates obtained from Monte Carlo simulations and kinetic equation solution, *IEEE Trans. Plasma Sci.*, *29*(3), 430–438, doi:10.1109/27.928940.

Briggs, M. S., et al. (2010), First results on terrestrial gamma ray flashes from the Fermi Gamma-ray Burst Monitor, *J. Geophys. Res.*, *115*, A07323, doi:10.1029/2009JA015242.

Carlson, B. E., N. G. Lehtinen, and U. S. Inan (2007), Constraints on terrestrial gamma ray flash production from satellite observation, *Geophys. Res. Lett.*, *34*, L08809, doi:10.1029/2006GL029229.

Carlson, B. E., N. G. Lehtinen, and U. S. Inan (2008), Runaway relativistic electron avalanche seeding in the Earth's atmosphere, *J. Geophys. Res.*, *113*, A10307, doi:10.1029/2008JA013210.

Carlson, B. E., N. G. Lehtinen, and U. S. Inan (2009), Terrestrial gamma ray flash production by lightning current pulses, *J. Geophys. Res.*, *114*, A00E08, doi:10.1029/2009JA014531.

Carlson, B. E., N. G. Lehtinen, and U. S. Inan (2010), Terrestrial gamma ray flash production by active lightning leader channels, *J. Geophys. Res.*, *115*, A10324, doi:10.1029/2010JA015647.

Celestin, S., and V. P. Pasko (2010), Soft collisions in relativistic runaway electron avalanches, *J. Phys. D: Appl. Phys.*, *43*(31), 315,206, doi:10.1088/0022-3727/43/31/315206.

Celestin, S., and V. P. Pasko (2011), Energy and fluxes of thermal runaway electrons produced by exponential growth of streamers during the stepping of lightning leaders and in transient luminous events, *J. Geophys. Res.*, *116*, A03315, doi:10.1029/2010JA016260.

Chanrion, O., and T. Neubert (2010), Production of runaway electrons by negative streamer discharges, *J. Geophys. Res.*, *115*, A00E32, doi:10.1029/2009JA014774.

Coleman, L. M., and J. R. Dwyer (2006), Propagation speed of runaway electron avalanches, *Geophys. Res. Lett.*, *33*, L11810, doi:10.1029/2006GL025863.

Dwyer, J. R. (2003), A fundamental limit on electric fields in air, *Geophys. Res. Lett.*, *30*(20), 2055, doi:10.1029/2003GL017781.

Dwyer, J. R. (2004), Implications of X-ray emission from lightning, *Geophys. Res. Lett.*, *31*, L12102, doi:10.1029/2004GL019795.

Dwyer, J. R. (2007), Relativistic breakdown in planetary atmospheres, *Phys.Plasmas*, *14*(4), 042,901, doi:10.1063/1.2709652.

Dwyer, J. R. (2008), Source mechanisms of terrestrial gamma-ray flashes, *J. Geophys. Res.*, *113*, D10103, doi:10.1029/2007JD009248.

Dwyer, J. R. (2012), The relativistic feedback discharge model of terrestrial gamma ray flashes, *J. Geophys. Res.*, *117*, A02308, doi:10.1029/2011JA017160.

Dwyer, J. R., and L. P. Babich (2011), Low-energy electron production by relativistic runaway electron avalanches in air, *J. Geophys. Res.*, *116*, A09301, doi:10.1029/2011JA016494.

Dwyer, J. R., and D. M. Smith (2005), A comparison between Monte Carlo simulations of runaway breakdown and terrestrial gamma-ray flash observations, *Geophys. Res. Lett.*, *32*, L22804, doi:10.1029/2005GL023848.

Dwyer, J. R., D. M. Smith, and S. A. Cummer (2012), High-energy atmospheric physics: Terrestrial gamma-ray flashes and related phenomena, *Space Sci. Rev.*, *173*, 133–196, doi:10.1007/s11214-012-9894-0.

Fishman, G. J., et al. (1994), Discovery of intense gamma-ray flashes of atmospheric origin, *Science*, *264*(5163), 1313–1316, doi:10.1126/science.264.5163.1313.

Geant4 collaboration, C. (2012a), *Physics Reference Manual Version 9.6.0*.

Geant4 collaboration, C. (2012b), *Geant4 User's Guide for Application Developers Version 9.6.0*.

Geant4 collaboration, C. (2013a), *Low Energy Electromagnetic Physics Working Group*.

Geant4 collaboration, C. (2013b), *Electromagnetic Standard Physics Working Group*.

Gjesteland, T., N. Østgaard, P. H. Connell, J. Stadsnes, and G. J. Fishman (2010), Effects of dead time losses on terrestrial gamma ray flash measurements with the Burst and Transient Source Experiment, *J. Geophys. Res.*, *115*, A00E21, doi:10.1029/2009JA014578.

Gurevich, A. V., G. M. Milikh, and R. Roussel-Dupré (1992), Runaway electron mechanism of air breakdown and preconditioning during a thunderstorm, *Phys. Lett. A*, *165*(5–6), 463–468, doi:10.1016/0375-9601(92)90348-P.

Paper II

7.2 Evaluation of monte carlo tools for high energy atmospheric physics

Casper Rutjes, David Sarria, Alexander Broberg Skeltved, Alejandro Luque, Gabriel Diniz, Nikolai Østgaard and Ute Ebert

Geoscientific Model Development, 9, doi:10.5194/gmd-9-3961-2016 (2016)

Geosci. Model Dev., 9, 3961–3974, 2016
www.geosci-model-dev.net/9/3961/2016/
doi:10.5194/gmd-9-3961-2016

Geoscientific Model Development
Open Access
EGU

Evaluation of Monte Carlo tools for high energy atmospheric physics

Casper Rutjes[1], David Sarria[2], Alexander Broberg Skeltved[3], Alejandro Luque[4], Gabriel Diniz[5,6], Nikolai Østgaard[3], and Ute Ebert[1,7]

[1]Centrum Wiskunde & Informatica (CWI), Amsterdam, the Netherlands
[2]Astroparticules et Cosmologie, University Paris VII Diderot, CNRS, Paris, France
[3]Birkeland Centre for Space Science, Department of Physics and Technology, University of Bergen, Bergen, Norway
[4]Instituto de Astrofísica de Andalucía (IAA-CSIC), P.O. Box 3004, Granada, Spain
[5]Instituto Nacional de Pesquisas Espaciais (INPE), São José dos Campos, São Paulo, Brazil
[6]Instituto de Física, Universidade de Brasília, Brasília (UnB), Distrito Federal, Brazil
[7]Eindhoven University of Technology, Eindhoven, the Netherlands

Correspondence to: Casper Rutjes (casper.rutjes@cwi.nl)

Received: 8 June 2016 – Published in Geosci. Model Dev. Discuss.: 20 June 2016
Revised: 9 September 2016 – Accepted: 7 October 2016 – Published: 8 November 2016

Abstract. The emerging field of high energy atmospheric physics (HEAP) includes terrestrial gamma-ray flashes, electron–positron beams and gamma-ray glows from thunderstorms. Similar emissions of high energy particles occur in pulsed high voltage discharges. Understanding these phenomena requires appropriate models for the interaction of electrons, positrons and photons of up to 40 MeV energy with atmospheric air. In this paper, we benchmark the performance of the Monte Carlo codes Geant4, EGS5 and FLUKA developed in other fields of physics and of the custom-made codes GRRR and MC-PEPTITA against each other within the parameter regime relevant for high energy atmospheric physics. We focus on basic tests, namely on the evolution of monoenergetic and directed beams of electrons, positrons and photons with kinetic energies between 100 keV and 40 MeV through homogeneous air in the absence of electric and magnetic fields, using a low energy cutoff of 50 keV. We discuss important differences between the results of the different codes and provide plausible explanations. We also test the computational performance of the codes. The Supplement contains all results, providing a first benchmark for present and future custom-made codes that are more flexible in including electrodynamic interactions.

1 Introduction

1.1 Phenomena in high energy atmospheric physics

Thunderstorms have been observed to produce terrestrial gamma-ray flashes (TGFs) (Fishman et al., 1994) and electron–positron beams (Dwyer et al., 2008b; Briggs et al., 2011). Signals lasting longer than TGFs such as x- and gamma-ray glows or thunderstorm ground enhancements (TGEs) have also been observed near thunderclouds, from balloons, planes, or high mountains (McCarthy and Parks, 1985; Eack et al., 1996; Tsuchiya et al., 2007; Adachi et al., 2008; Chilingarian et al., 2010, 2011).

Two possible theories are currently under discussion, as reviewed by Dwyer et al. (2012), to create these phenomena by runaway electrons (Wilson, 1924), which may further grow in the form of so-called relativistic runaway electron avalanches (RREA), introduced by Gurevich et al. (1992).

The first theory has been called the cold runaway theory (Gurevich, 1961) where thermal electrons are accelerated into the runaway regime within the strong electric fields of a transient discharge. Theoretical literature first focussed on the phase of the streamer discharge (Moss et al., 2006; Li et al., 2009; Chanrion and Neubert, 2010), and later on leader discharges (Celestin and Pasko, 2011; Celestin et al., 2012; Chanrion et al., 2014; Köhn and Ebert, 2015). Cold runaway is certainly at work in high energy emissions

from nanosecond pulsed discharges (Stankevich and Kalinin, 1967; Kostyrya et al., 2006; Tarasenko et al., 2008; Shao et al., 2011) and during the formation of long sparks (Noggle et al., 1968; Dwyer et al., 2008a; Rep'ev and Repin, 2008; Cooray et al., 2009; Kochkin et al., 2012, 2015, 2016) in high voltage and pulsed plasma technology.

The second theory is the relativistic feedback discharge model by Dwyer (2003). It is based on sustaining the RREA multiplication of the relativistic electrons in sufficiently high electric fields within a thunderstorm, by feedback of photons and positrons creating new avalanches (Babich et al., 2005; Dwyer, 2007, 2012). The first electrons are typically supplied by cosmic particles from the sun or from other galactic or extragalactic sources. High energy seed electrons might also origin from lightning leaders, from radioactive decay or from some mixed form of electron sources.

An extreme case both of cold or RREA would be a relativistic runaway electron front where the density of runaway electrons is high enough to provide electric screening behind the ionization front (Luque, 2014).

We remark as well that a sufficiently energetic cosmic particle can create an extensive air shower with very high electron density in the shower core even in the absence of any electric fields; such densities were used by Dubinova et al. (2015) to explain lightning inception, and these air showers were also used to measure electric fields in thunderstorms (Schellart et al., 2015; Trinh et al., 2016). Radioactive decay is another source of high energy particles in the atmosphere.

All these phenomena require tracing the propagation of energetic electrons, photons and also positrons through air, as well as modeling their interaction with air molecules and the subsequent scattering and energy loss or even total loss of the primary particles, together with the generation of secondary particles.

1.2 The multiple scales in energy and length

There are two basic problems for simulating these high energy phenomena in our atmosphere, related to the wide range of scales in energy and length.

First, the models have to bridge energy scales from tens of MeV down to thermal energies of tens of meV ($300\,\mathrm{K} \rightarrow 0.03\,\mathrm{eV}$), i.e., over 9 orders of magnitude. At the upper edge of this energy range, models developed by the high energy physics community (e.g., for CERN) exist where it should be noted that they were originally developed for even higher particle energies, and for the interaction of energetic particles with metals rather than with air – though radiation medicine now also develops models for the penetration of energetic radiation into biological tissue (Andreo, 1991; Sempau et al., 2001; Carrier et al., 2004), which consists mostly of similarly light molecules as air, but in the liquid rather than the gaseous state. In the low energy regime, models by the low temperature plasma physics community should be used, with cross sections listed, e.g., on the community web page (Pancheshnyi et al., 2012).

Second, in particular for cold runaway models, there are two widely separated spatial scales: the source region with high and time-dependent self-consistent electrodynamic fields where electrons are accelerated, and the wide propagation distances from the source to detectors in space or on the ground where electric fields can be neglected.

Here, we focus on the second problem, namely the beam propagation towards detectors where the final products are characterized by energy spectra and arrival times, and the source properties must be reconstructed from this data, e.g., in the work by Østgaard et al. (2008). Accurately modeling the transport from the source to the very remote detector is, together with some knowledge of the source, thus very important to deduce production altitude, beaming angle or light curves of TGFs and associated electron beams from space data (Dwyer and Smith, 2005; Carlson et al., 2007; Hazelton et al., 2009; Dwyer et al., 2008b; Sarria et al., 2016).

1.3 Content and order of the present study

To model particle beams in air far from the source, some researchers use general purpose Monte Carlo (MC) codes developed by large collaborations like Geant4 (used by Carlson et al., 2011 and by Skeltved et al., 2014) or FLUKA (used by Dubinova et al., 2015). On the other hand, to model, e.g., the radiation sources with their external or even self-consistent time-dependent electric fields, other researchers may develop custom-made codes in small groups or as individuals, where the cross sections and numerical methods may come from already validated theory (e.g., Sarria et al., 2015; Kohn et al., 2014).

While they are necessary for the understanding of the full physical phenomena, custom-made codes are difficult to validate, especially if they are not made available by open access. Differences between one code and another may be explained by at least the following four factors:

- the choice of the included physics, as a compromise between correctness and feasibility;
- cross sections that can come from theory, measurements or both (in most cases, the cross section data have a certain uncertainty);
- numerical and coded implementation, e.g., numerical integrations, interpolations, roundoff errors and bugs;
- the performance, as faster codes can run more particles in the same time, which results in more accurate statistics.

Even if it is possible in principle to determine the differences between the physical models and between the numerical methods, it may be very complicated (if not impossible)

– to estimate the uncertainties associated with a certain choice of physical models,

– to estimate the uncertainty propagation and accumulation of all input through the full multiscale models, and

– to review all source codes (if available) to find any mistakes and possible numerical problems.

In general, it is found that software is underrepresented in high energy physics literature in spite of its significant contribution to the advancement of the field (Basaglia et al., 2007).

Therefore, we strive here to provide a comparison standard for the particle codes, as simple and informative as possible, by only considering their physical outputs. We have chosen standard tests for the core parts of all codes: the evolution of monoenergetic and monodirectional beams of photons, electrons and positrons through homogeneous air and without electric or magnetic fields. We elaborate our standard tests in the methodology (Sect. 4).

The targeted energy interval for high energy atmospheric physics in this study is from tens of keV to tens of MeV, bounded above by the observed maximal energy in a TGF (Briggs et al., 2010; Marisaldi et al., 2014). Typically, a low energy cutoff is chosen for two reasons:

1. The codes developed for accelerator or cosmic-ray applications use typical energies well above 1 MeV, larger than the rest mass of electrons and positrons. For these energies relativistic approximations are accurate, ionization potentials are negligible, and electron impact ionization is essentially a free–free elastic collision (i.e., similar to a collision of two free electrons). These approximations limit the validity of the codes at lower energies.

2. The mean free path of particles decreases and the number of particles increases with decreasing energy. Simulating with or without a low energy cutoff can make a difference of minutes to months of simulation time. Therefore, a low energy cutoff is wanted for computational reasons.

The different implementations of the low energy cutoff, as reviewed in Sect. 3, cause significant differences in the results (see Sect. 5). These differences increase when electric fields are added (see Sect. 6) and puts an extra restriction on the value of low energy cutoff (Skeltved et al., 2014).

This paper is organized as follows: Sects. 2 and 3 review the particle interactions and the codes included in this study. Section 4 describes the methodology we used to compare the codes. Section 5 contains a discussion of important differences between the results of the tested codes, and in Sect. 6 the implications of adding electric fields are discussed. Finally, we conclude and give a list of recommendations for high energy atmospheric physics simulations in Sect. 7.

2 Overview of interactions and approximations

In high energy atmospheric physics (HEAP), it is usually assumed that the density of the considered high energy particles is too low for them to directly interact which each other; therefore, they only interact with the background medium, which are the air molecules here. In addition, for some self-consistent codes like GRRR (see Sect. 3.4), charged particles can interact non-locally due to the electric fields they produce. But for the present study these interactions are turned off, resulting in a linear problem. This means that the number of particles at the end of the beam is proportional to the particle number in the initial beam, and that different beams simply add up according to the superposition principle. Below, we summarize the interactions considered for electrons, positrons and photons in HEAP. In these interactions, the target molecule M and its resulting state are explicitly given, but for the MC model of the high energy particles, these molecules (or ions) act as a random background.

2.1 Electrons and positrons

Electrons and positrons above 50 keV (which is the low energy cutoff in our study) behave almost identically; they scatter elastically on molecules M, they ionize them and they create bremsstrahlung on collisions with molecules:

$$e^{\pm} + M \rightarrow \begin{cases} e^{\pm} + M, & \text{elastic (Rutherford)}, \\ e^{\pm} + e^{-} + M^{+}, & \text{ionization}, \\ e^{\pm} + \gamma + M, & \text{bremsstrahlung}, \end{cases} \quad (1)$$

with cross sections that only slightly dependent on the incoming particle type.

In addition, when positrons come to rest, they annihilate as follows:

$$e^{+} + M \rightarrow 2\gamma + M^{+}, \quad \text{annihilation}, \quad (2)$$

and produce two photons of 511 keV. The standard implementation is that, when a positron drops below the low energy cutoff, it comes to rest immediately (in space and time). In reality, the positron will come to rest over some distance and time, forming positronium (e.g., an $e^{+}e^{-}$ bound state) before annihilation. The positronium has a lifetime depending on the spins of the positron and electron (Karshenboim, 2004), forming a singlet or triplet state with lifetimes of 124 ps or 139 ns (in vacuum), respectively. If the triplet state is formed in a medium like air, the lifetime permits "pick-off" annihilation where an opposite spin electron from the medium will annihilate in singlet orientation before the triplet-oriented electron can collapse and annihilate with the positron, thus again resulting in two photons (instead of three). Thus, besides a small time delay, the magnitude of 511 keV line in the photon spectrum is not changed. None of the codes with the settings used in this benchmark include positronium.

In the eV regime, the interactions are getting more complex, as molecular excitations and dissociations need to be taken into account explicitly.

2.1.1 Friction (or stopping power) for electrons and positrons

Usually, the energy transfer in an ionization collision of electrons and positrons with molecules is of the order of 10 eV; hence, it causes only a small energy loss for a particle with energy above the keV range. By introducing a so-called low energy cutoff $\varepsilon_{\mathrm{cut}}$, high and low energy particles and interactions can be decoupled. In this approximation, interactions producing secondary particles below the low energy cutoff are approximated as friction, while interactions with secondary particles above the cutoff are included explicitly.

Let ε_1 be the energy of the primary particle and ε_2 the energy of the secondary particle. The cross section $\sigma_k(\varepsilon_1)$ (in units of area) gives the probability of the primary particle to undergo an interaction labeled k. The differential cross section $\mathrm{d}\sigma_k(\varepsilon_1, \varepsilon_2)/\mathrm{d}\varepsilon_2$ (in units of area per energy) gives the probability of a primary particle to produce a secondary particle within the infinitesimal energy interval $[\epsilon_2, \epsilon_2 + \mathrm{d}\epsilon_2]$ for the interaction k.

The secondary energy ε_2 can take values between the minimum $\varepsilon_{\mathrm{min}}$ (of the order of eV and the primary is not sensitive for the precise value) and the maximum $\varepsilon_{\mathrm{max}}$ (of the order ε_1), depending on the interaction. For ionization $\varepsilon_{\mathrm{max}} = \varepsilon_1/2$ as the primary by convention is defined to be the final particle with the highest energy. For bremsstrahlung, we have $\varepsilon_{\mathrm{max}} = \varepsilon_1$.

Now the energy range of the secondary particles is decomposed into two parts: the first part from $\varepsilon_{\mathrm{min}}$ to $\varepsilon_{\mathrm{cut}}$ is implemented as a friction, and the second part from $\varepsilon_{\mathrm{cut}}$ to $\varepsilon_{\mathrm{max}}$ is implemented by discrete collisions.

The friction F_k of interaction k is defined as

$$F_k(\varepsilon_{\mathrm{cut}}, \varepsilon_1) = N \int_{\varepsilon_{\mathrm{min}}}^{\varepsilon_{\mathrm{cut}}} \left(\varepsilon_{\mathrm{loss}}(\varepsilon_2) \frac{\mathrm{d}\sigma_k(\varepsilon_1, \varepsilon_2)}{\mathrm{d}\varepsilon_2} \right) \mathrm{d}\varepsilon_2, \tag{3}$$

where N is the number density of molecular collisions targets M, and $\varepsilon_{\mathrm{loss}}$ the energy loss of the primary which is of the order of ε_2 plus the ionization energy. The resulting friction on the primary is given by the sum of all considered interactions,

$$F(\varepsilon_{\mathrm{cut}}, \varepsilon_1) = \sum_k F_k(\varepsilon_{\mathrm{cut}}, \varepsilon_1). \tag{4}$$

For electrons and positrons in the energy regime important for HEAP, the resulting friction is almost completely determined by the ionization part, as illustrated in Fig. 1. Especially if only the friction with $\varepsilon_{\mathrm{cut}} = 50\,\mathrm{keV}$ is considered (solid line), there the energy loss due to bremsstrahlung is more than 2 orders of magnitude smaller than the energy loss due to ionization.

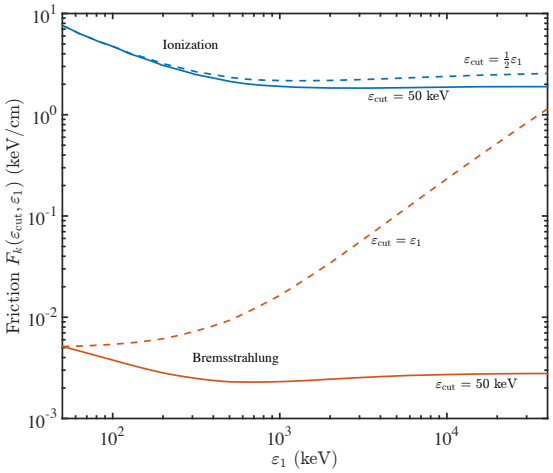

Figure 1. Friction $F_k(\varepsilon_{\mathrm{cut}}, \varepsilon_1)$ for electrons per interaction (bremsstrahlung in red and ionization in blue) for two different low energy cutoffs, $\varepsilon_{\mathrm{cut}} = 50\,\mathrm{keV}$ (solid line) and $\varepsilon_{\mathrm{cut}} = \varepsilon_{\mathrm{max}}$ (dashed line). The resulting friction is the sum of the two contributions, which in the energy regime of HEAP is dominated by the ionization (please note the log scale). The data are from Cullen et al. (1997) and Perkins et al. (1991) for an air density of $1.293 \times 10^{-3}\,\mathrm{g\,cm^{-3}}$ corresponding to 1 bar and 273 K as used in this study.

We remark that the friction is also frequently called the stopping power for historical reasons, though it has the dimension of friction (energy/length) rather than of power (energy/time).

2.1.2 Straggling

In a simple implementation of the low energy cutoff, the primary particle suffers a uniform (and deterministic) friction $F(\varepsilon_{\mathrm{cut}}, \varepsilon_1)$, as given in Eq. (4). This means that now only the energy of the primary particle is altered, but not its direction. A greater concern is that the accuracy of the assumed uniform energy loss is a matter of length scale. If the scale is much smaller than $\varepsilon_1/F(\varepsilon_{\mathrm{cut}}, \varepsilon_1)$, only a few interactions have taken place. On such a small length scale, the real energy loss distribution (if one had considered all interactions explicitly) among the population would have a large spread. This effect is called straggling, and it was first studied by Bethe and Heitler (1934).

One way to mimic the real energy distribution is by implementing a stochastic friction, as is done in FLUKA and Geant4L. Basically, the energy loss of the primary particle is as if it would be modeled by real low energy collisions below the cutoff, but without creating the secondary particles and without altering the direction of the momentum. The different implementation of the low energy cutoff (i.e., different implementations of the friction) is one of the significant dif-

ferences we see in the studied programs, as discussed in the results (Sect. 5).

2.1.3 Continuous slowing down approximation

Using the friction Eq. (3) over the whole range of secondary particle energies, hence with $\varepsilon_{\text{cut}} = \varepsilon_{\text{max}}$, the expectation value of the maximal penetration depth of a primary particle into a medium can be calculated in the so-called continuous slowing down approximation (CSDA). Integrating the friction over distance ℓ up to the point where the particle has lost all its primary energy ε_1,

$$\int_{\ell(\varepsilon_1)}^{\ell(0)} F(\varepsilon_{\text{max}}, \varepsilon(\ell))\ \mathrm{d}\ell = \int_{\varepsilon_1}^{0} F_{\text{tot}}(\varepsilon_{\text{max}}, \varepsilon) \frac{\mathrm{d}\ell}{\mathrm{d}\varepsilon}\ \mathrm{d}\varepsilon = \varepsilon_1, \quad (5)$$

defines one CSDA range through

$$\text{CSDA}(\varepsilon_1) = \ell(\varepsilon_1) - \ell(0). \quad (6)$$

One CSDA range is thus the maximal length that primaries can penetrate a material. Due to feedback from secondaries (e.g., electron → photon → electron) the complete avalanche can survive longer. As we describe in the methodology (Sect. 4), we choose half a CSDA range as the optimal detector distance to compare the differences in outputs of the codes as comprehensively as possible.

2.2 Photon interactions

The typical photon interactions are

$$\gamma + M \rightarrow \begin{cases} \gamma + M, & \text{elastic (Rayleigh),} \\ e^- + M^+, & \text{ionization (by absorption),} \\ \gamma + e^- + M^+, & \text{ionization (by Compton),} \\ e^+ + e^- + M, & \text{pair production.} \end{cases} \quad (7)$$

Photons have no charge, and therefore they lose energy much less gradually than electrons and positrons. In a typical inelastic interaction of a photon, the energy loss is significant.

Photon attenuation

The most important interaction for low energies (below 30 keV) is photoabsorption, and for the highest energies (above 40 MeV) it is pair production; in both cases, the photon completely disappears. In between, where Compton scattering is most important, the energy loss per interaction is still significant; the expectation value for the energy loss of the primary photon grows from 5 % (at 30 keV) to above 90 % (at 1 MeV). The continuous slowing down approximation is thus not appropriate for photons, as photons do not continuously lose small amounts of energy, in contrast to electrons and positrons, but they lose a substantial fraction of their energy after some free path. Consecutively, for most energies (certainly above 1 MeV and below 30 keV) the photon intensity I can be approximated by an exponential decay or attenuation,

$$I(\ell) = I(0) \exp(-\ell/\mu), \quad (8)$$

where $\mu(\varepsilon)$ is the attenuation coefficient depending on energy (and material).

In this work, we need to estimate an appropriate detector distance (the exponential decay does not appear explicitly in any model), and we use two e-folding lengths (i.e., the inverse of half the attenuation coefficient) as the optimal detector distance to compare the output differences, as described further in the methodology (Sect. 4).

Table 1. Codes used in this benchmark, their validity range (usable energy interval) and relative performance (normalized to the fastest code), possible inclusion of electric and magnetic fields (***E*** and ***B***) and self-consistent fields due to space charge. It should be noted that the synchronous particle tracking in GRRR, for the possible inclusion electric fields due to space charge, and the simulation without low energy cutoff approximation in MCPEP, limits their performance. For more descriptions, see Sect. 3.

Code	Validity range (eV)	Relative perform.	***E*** & ***B***	Space charge
EGS5	$[10^4, 10^{11}]$[a]	4.02	N & N	N
FLUKA	$[10^4, 10^{11}]$	1.03	N[c] & N[c]	N
Geant4L	$[10^2, 10^{12}]$[b]	1.17	Y[d] & Y	N
Geant4D	$[10^2, 10^{12}]$[b]	1.00	Y[d] & Y	N
GRRR	$[10^4, 10^7]$	12.4	Y[d] & Y	Y
MCPEP	$[10, 10^8]$	102	N & Y	N

[a] 10 keV is the lowest energy advised in the manual, but in this study we found that this is too low; see Sect. 5.3. [b] 250 eV minimum for electrons and positrons and 10 eV minimum for photons. [c] Not out of the box, but there are add-ons or umbrella codes that provide this feature, e.g., CORSIKA (Heck et al., 1998). [d] The magnitude of the electric field will be limited by the choice of the low energy cutoff.

3 Overview of codes

In Table 1, we have summarized the codes used in this benchmark. In this chapter, we give more detailed descriptions.

3.1 EGS5

EGS5 (Electron-Gamma Shower version 5, developed by Hirayama et al., 2005) is a general purpose software package for the Monte Carlo simulation of the coupled transport of electrons, positrons and photons in an arbitrary geometry. It is the next version after EGS4 that was released by Nelson et al. (1985) with a history that dates back to the 1960s. The user controls an EGS5 simulation by means of an input text file for settings and a written FORTRAN user code, to which

the rest of the FORTRAN source files are appended and compiled as one. In the user code, several subroutine calls create, establish and initiate the cascade. Two important subroutines, HOWFAR and AUSBGAB, which should be written inside the user code, are used to specify the geometry and the output of the results. EGS5 can simulate particles from a few keV up to several hundred GeV, depending on the material. There is a limited option for including magnetic fields, and no option to include electric fields. All interactions of Eqs. (1), (2) and (7) are implemented, in this work with a low energy cutoff of 50 keV. In the user manual of Hirayama et al. (2005), a minimum low energy cutoff of 10 keV is advised, but we noticed that for the bremsstrahlung cross sections relativistic limits are applied, which results in a production of photons that is too low (see Sect. 5.3). Friction is implemented uniformly, without straggling effect (that is to say without fluctuations in the energy loss). The input file and user code, used in this work, can be found in the Supplement. Please see the documentation of Hirayama et al. (2005) for a detailed overview of the implemented physics.

3.2 FLUKA

FLUKA (developed by Ferrari et al., 2005, copyright to INFN and CERN 1989–2011), is a general purpose tool for calculations of particle transport and interactions with matter. FLUKA is able to simulate the interaction and propagation in matter of roughly 60 different particles, including photons from 100 eV and electrons and positrons from 1 keV to thousands of TeV, neutrinos, muons of any energy, hadrons of energies up to 20 TeV (up to 10 PeV by linking FLUKA with the DPMJET code) and all the corresponding antiparticles and neutrons down to thermal energies. FLUKA includes recent data sets, published by Böhlen et al. (2014). The program can handle magnetic and electric fields, although not self-consistently (i.e., the charged particles do not produce magnetic or electric fields). The program, written in FORTRAN, reads in so-called user cards, in which the user defines the geometry, materials and detectors. The user card, used in this work, can be found in the Supplement. All interactions of Eqs. (1), (2) and (7) are implemented in this work with a low energy cutoff of 50 keV. Friction in FLUKA is modeled with universal fluctuations, mimicking the straggling effect, meaning that the primary particle loses its energy as if it would undergo random collisions. But the direction of its momentum is not changed and no secondary particles are produced. Please see the documentation of the FLUKA manual at http://www.fluka.org for a detailed overview of the implemented physics.

3.3 Geant4

Geant4 is an open-source toolkit to simulate the passage of particles through matter, developed by a wide international collaboration led by the CERN. It is coded in C++, following an object-oriented philosophy. It can simulate the transport of almost all known particles and can include electric and magnetic fields (Agostinelli et al., 2003). We use the version 10.2 released in December 2015. In Geant4, the user can choose between six main models for the treatment of electrons, positrons and photons, with different performances and accuracies. One can also specify the implementation of the friction, in order to take into account energy losses below the low energy cutoff. For this study, we are using two Geant4 configurations that are detailed below. All Geant4 codes are available in the Supplement. References and details for these models are presented in the Geant4 physics reference manual available at http://geant4.web.cern.ch.

3.3.1 Geant4D

Geant4D uses the default model, but in addition we deactivated the fluctuations of the continuous energy loss, i.e., the energy losses are applied uniformly without straggling effect. This choice is for benchmark purposes, in order to identify the effect of straggling.

3.3.2 Geant4L

Geant4L uses the Livermore model, which uses cross sections from the EPDL and EEDL databases, provided by the Lawrence Livermore National Laboratory. The detailed implementation is provided in Cullen et al. (1997) and Perkins et al. (1991). The universal fluctuation model is activated to include the straggling effect in the implementation of friction.

3.4 The GRanada Relativistic Runaway (GRRR) code

Developed by A. Luque at the Astrophysics Institute of Andalusia (IAA-CSIC), the GRanada Relativistic Runaway (GRRR) code was designed to investigate the self-consistent interaction between electrons in the limit of very intense RREAs. This investigation, presented in Luque (2014), concluded that due to the interaction between electrons in the avalanche RREAs saturate into a steady-state propagating relativistic runaway ionization front (RRIF). As the GRRR code was implemented with that specific goal in mind, its scope is narrower than the general purpose codes (EGS5, FLUKA, Geant4) analyzed in this paper. It only follows the evolution of high energy electrons, and includes a limited set of interactions between these electrons and the embedding medium. Electron ionization and Rutherford scattering are modeled discretely and, in this work, down to a low energy cutoff of 50 keV. The friction for these interactions is uniform and without straggling effect. Bremsstrahlung collisions with nuclei are modeled deterministically by friction; in other words, as continuous radiative losses. The Supplement of Luque (2014) contains further details about the physical model underlying the GRRR code. In the Supplement of this work, the input files are given for the presented bench-

mark tests. The full source code for GRRR is available at https://github.com/aluque/grrr. However, presently the code is mostly undocumented so we advise potential users to contact the author.

3.5 MC-PEPTITA

The Monte Carlo model for photon, electron and positron tracking in terrestrial atmosphere (MC-PEPTITA) by Sarria et al. (2015) is a Fortran 90 code that simulates the propagations of TGF and associated electron–positron beams within the Earth environment from the production altitude at 10 to 20 km to satellite altitude. To simulate the quasi-exponential atmospheric density profile and the Earth's magnetic field, it uses the NRLMSISE-00 and IGRF-11 models (Cullen et al., 1997; Perkins et al., 1991). It is optimized to run in this environment, whereas some other codes (e.g., Geant4) can only handle layers of constant density. Concerning the interactions between particles and matter, it mainly uses the EPDL and EEDL cross section sets (Cullen et al., 1997; Perkins et al., 1991), except for inelastic scattering of electrons and positrons where the GOS model is used. The interactions are simulated similarly to PENELOPE (Salvat et al., 2011), with equivalent numerical methods. MC-PEPTITA does not include any continuous energy losses: the particles are followed discretely down to the lowest possible energies allowed by the models used, with the exception of bremsstrahlung where the minimal energy is set to 100 eV.

4 Methodology

We focus on the evolution of monoenergetic and directed beams of electrons, positrons and photons with kinetic energies between 100 keV and 40 MeV through homogeneous air in the absence of electric and magnetic fields, using a low energy cutoff of 50 keV providing a first benchmark, in the case when the fields are turned off. Assuming sufficiently low densities of high energy particles, arbitrary particle beams can be decomposed into such monoenergetic and directed beams.

The electron, positron and photon beams propagate through air, consisting of 78.085 % nitrogen, 20.95 % oxygen and 0.965 % argon. We use a constant and homogenous air density of $1.293 \times 10^{-3}\,\mathrm{g\,cm^{-3}}$ which corresponds to 1 bar and 0 °C. For all programs, we choose a low energy cutoff of 50 keV, below which all particles are removed. For most programs, this low energy cutoff is also the threshold to treat collisions discretely or continuously, with two exceptions: MC-PEPTITA handles all collisions explicitly, and GRRR uses continuous radiative loss (bremsstrahlung). During the simulation electrons, positrons or photons above the low energy cutoff can be created (except for GRRR, which only models electrons), and are then followed as well until they also drop below the low energy cutoff. If considered in the program, positrons dropping below the low energy cutoff can produce photons by annihilation above the low energy cutoff.

We use ideal flat surface detectors, perpendicular to the primary particle beam. On a detector, the type, kinetic energy, position and arrival time of the arriving particles are recorded. After detection, the particles are removed from the program, thus we do not measure backscattered particles that have already been detected. Depending on the program, other secondary particles are created with a very low probability (e.g., neutrons by photonuclear interactions), but we do not record them in the output. First, we study the particle number of all particles as function of propagation distance (attenuation). Second, for one specific distance, (depending on particle type and initial energy) we proceed to a detailed analysis of energetic, spatial and temporal distribution. Complementarily, we also benchmark the performance (i.e., the simulation completion time) of the programs used in this study.

4.1 The number of particles vs. distance (attenuation)

We study the particle number of all particles as a function of beam propagation distance, up to one CSDA range for electrons and positrons and 4 times the inverse of the attenuation coefficient (four e-folding lengths) for photons. This range is divided in several distances (roughly 20) or data points. For each distance (or data point), we perform a new simulation. Each simulation has 10 000 particles in the initial beam for beams of electrons, positrons and photons with energies of 0.1, 0.4, 1, 10 and 40 MeV. The particle numbers are therefore derived under the assumption that the detectors are impenetrable. This means that backscattering is excluded, and that the particle number therefore is lower than in a passing avalanche in air only.

We added a $\pm 1/\sqrt{n_i}$ relative error expected from the Monte Carlo methods (n_i being the number of counts in the ith bin). In this way, we performed roughly 1800 simulations, namely circa 300 simulations per program: for 3 particle types, 5 initial energies and, on average, 20 distances per beam. GRRR only considers electrons while the energy loss due to production of photons is implemented as a continuous energy loss. The relevant results are given and discussed in Sect. 5. In addition, all the data of this part are visualized and available in the Supplement.

4.2 Spectral analysis

We performed detailed simulations with 1 million particles per beam for one specific distance per beam. For electrons and positrons, the detection distance was chosen as half of the CSDA range. This gives most information in one plot, since the primary particles are still alive, while there is a significant number of secondary particles produced. For photons, the inverse of half the attenuation coefficient (two e-folding lengths) is chosen as the distance for the detailed study. At the detector, we analyze the kinetic energy, the ra-

dial distance from the symmetry axis and the time of arrival. The spectra are binned using the Freedman–Diaconis rule in the log domain and rescaled to numbers per primary. As for the attenuation study, we added a $\pm 1/\sqrt{n_i}$ relative error expected from the Monte Carlo methods (n_i being the number of counts in the ith bin). We performed roughly 90 different simulations (ca. 15 simulations per program: 3 particles and 5 initial energies). The relevant results are given and discussed in Sect. 5. In addition, all the data of this part are visualized and available in the Supplement.

4.3 Performance benchmark

As a complement, we also tested how much time the codes needed to complete the simulations. We did not try to do an in-depth performance benchmark of the codes, but we think this is an interesting piece of information for someone who is seeking for a code to be used in the HEAP context. Since the programs are written in different languages (Fortran, C++ and Python) and may be run on different machines with different architectures, we normalized the completion time with respect to a reference computer configuration.

The simulation starting with 1 million 1 MeV electrons is used as the test case because it is feasible for all the evaluated codes, and it takes a completion time that is neither too short nor too long. More details are given in the Supplement. The normalized results are discussed in Sect. 5.5.

5 Results

Most tests show similar outputs for the different codes within deviations of ± 10 % (see the Supplement). Here, we focus on important differences between the results of the codes, and we provide several plausible explanations.

5.1 Straggling

For electrons and positrons below 1 MeV, the data clearly show the effect of straggling, as discussed in Sect. 2.1.1. For example, in the 400 keV electron beam shown in Fig. 2, EGS5, Geant4D and GRRR do not include straggling; therefore, the maximal electron energy is too small and the drop of the energy spectrum towards this maximal energy is too steep. Geant4L, MCPEP and FLUKA show the correct spectrum, but for different reasons. MCPEP simulates without a low energy cutoff (and thus without friction). Geant4L and FLUKA use a stochastic implementation of the friction called universal fluctuations. Basically, the friction is not applied uniformly to all particles of the same energy equally, but a distribution of energy losses in time mimics the random nature of the collisions. Only the direction change is considered negligible.

The same effect is also seen for electron and positron beams with energy above 10 MeV, in the scenario where bremsstrahlung is treated as continuous. GRRR shows an unphysical drop in the electron spectrum at high energies, as illustrated in Fig. 3. The reason is that the energy loss by bremsstrahlung is mostly above the low energy cutoff (see Fig. 1), meaning that the energy loss of the electrons and positrons is mostly due to discrete hard collisions and thus ill approximated by uniform-averaged friction. Nevertheless, we found that the total integrated energy is similar. This approximation is also used by others in the community like Celestin et al. (2012) and Chanrion et al. (2014).

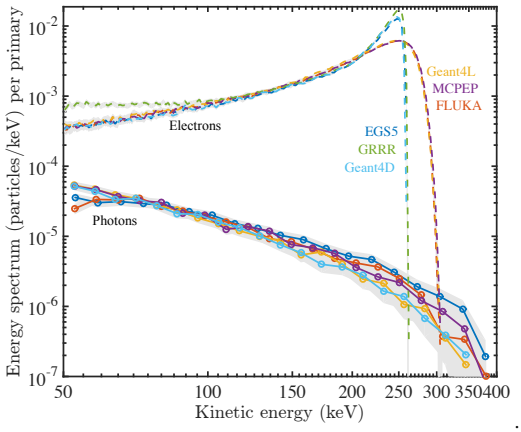

Figure 2. Products of a beam of 400 keV electrons after a propagation distance of 0.5 times their CSDA range which is 1.9 m in air at 1 bar and 273 K. The electrons have now a maximal energy of 250 to 300 keV depending on the code, but the total integrated energy is equivalent. The difference in electron distribution is due to straggling by ionization; see Sect. 5.1

5.2 Opening angle

High energy photons penetrate the medium much deeper than electrons and positrons, and therefore small differences in opening angles after Compton collisions are more important. In inelastic collisions photons always lose a significant amount of energy, as discussed in Sect. 2.2, and therefore they get a significant opening angle.

MCPEP simulates all collisions explicitly (others use a friction, which does not change the primary direction). The energy spectra agree between these codes, but Fig. 4 illustrates that the radial and temporal spectra vary: MCPEP shows a wider photon beam and substantially later photon arrival times.

5.3 Bremsstrahlung

We saw that EGS5 uses an ultra-relativistic approximation in the treatment of bremsstrahlung and thereby we question the validity at lower energies, as discussed in Sect. 3.1. For the primary electron, in the energy regime important for

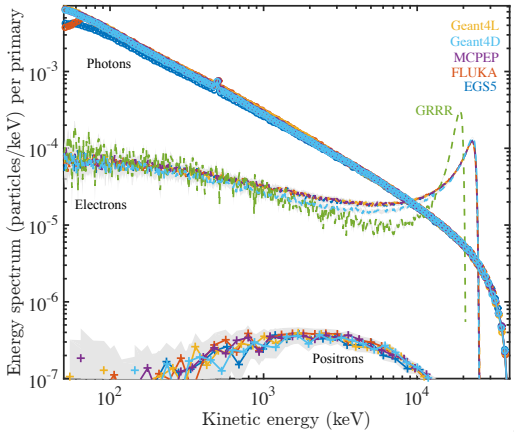

Figure 3. The same as in Fig. 2, but now for 40 MeV electrons. The propagation distance of 0.5 times their CSDA range is now 63.8 m (1 bar and 273 K). Now, not only electrons and photons but also positrons have been produced. The difference in electron distribution is due to straggling by bremsstrahlung; see Sect. 5.1

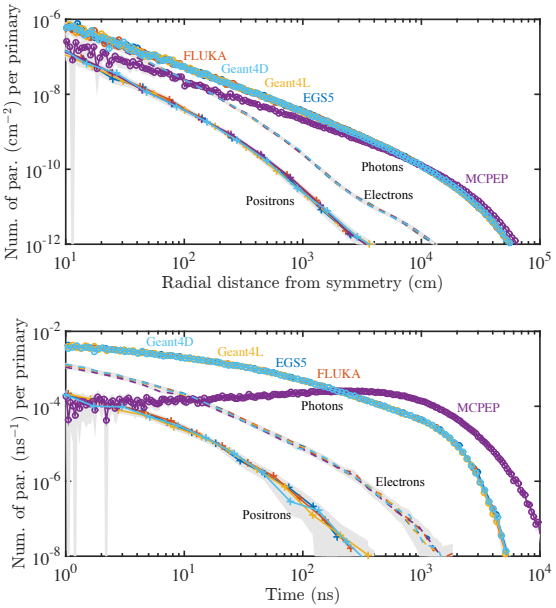

Figure 4. Products of a beam of 10 MeV photons at a distance of 1/(0.5 μ) which corresponds to 756 m (1 bar and 273 K). Particle number per primary is a function of the radial distance from the symmetry axis (above) and arrival time (below).

HEAP, bremsstrahlung is negligible compared to ionization (see Fig. 1), and we thus do not see a difference there, but in the production of photons there is a significant difference, as can be seen in Fig. 5.

5.4 Other differences

Other differences we have found are listed below.

- For the electron and positron beams, we see a dip in the number of photons in the energy spectrum of FLUKA below 70 keV. Figure 3 shows an example.

- For the electron beams ≤ 1 MeV (but not in the positrons or photon beams) we see a difference in the longest arrival times (> 100 ns) for photons between the programs FLUKA and EGS5 compared to Geant4D and Geant4L. GRRR does not model photons, and MCPEP is completely different because of the opening angle (see Sect. 5.2).

- GRRR shows a slightly higher count (less than 15 % higher) than the other codes for the number of electrons in the avalanche as function of distance. Figure 5 shows an example. In the energy spectrum, we see that these electrons are in the low energy tail of the spectrum (see, for example, Fig. 2).

- For the electron and positron beams, we see a difference in the shortest arrival times (< 1 ns) for electrons and positrons between the programs FLUKA, EGS5 and MCPEP compared to Geant4D, Geant4L and GRRR.

5.5 Performance

The performances in terms of completion time of the codes are presented in Table 1. On one hand, we see a clear difference of performance between MC-PEPTITA (simulations with a low energy cutoff as low as possible) and the rest. As said in the introduction, the low energy cutoff is generally introduced to speed up the simulation. Moreover, MC-PEPTITA was not optimized to run with a constant density and without magnetic field, and is then making a significant amount of useless (but time-consuming) calculations for this benchmark case. On the other hand, the choice to simulate all particles synchronously (to include self-consistent electric fields) slows the simulations down significantly, as seen for GRRR.

Concerning codes developed by wider collaborations, Geant4 and FLUKA show similar and best performances, but EGS5 is about 4 times slower. We can also note that in Geant4, the use of the energy straggling costs about 20 % more computation time than turning it off.

6 The effect of electric fields

In this study, we have provided benchmarks in the absence of electric fields, applicable to custom codes when the fields are turned off. The programs reviewed in this study are at least

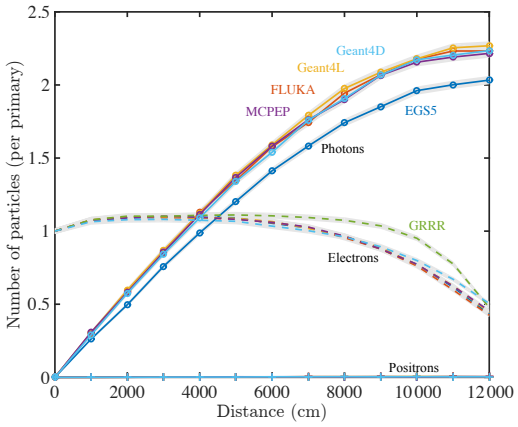

Figure 5. Products of a beam of 40 MeV electrons, as detected by 12 detectors at 10 to 120 m distance in 1 bar and 273 K. The detectors are impenetrable to hinder backscattering; therefore, a new simulation is run for every detector distance.

able to simulate the simplest case of particle beam evolution in air, in the wide distance from the particle source to detectors in space and on ground. However, as discussed in the introduction, the particles are initially accelerated by electric fields in the thunderstorm, either by weaker fields in larger regions in the relativistic feedback regime, or by strong and very localized self-consistent electric fields in the cold runaway regime. We here give a short outlook on the range of validity of the presented models in these cases. In general, it can be expected that electric fields will magnify all differences in choice and implementation of cross sections to a certain extent, because particles not just lose energy and drop eventually below the energy cutoff, but charged particles can also be re-accelerated and reappear in the ensemble.

To be specific, we recall the definition of the three characteristic electric fields and electron energy regimes of the problem (giving field values for air at standard temperature and pressure (STP)). For electrons with energies in the eV regime, the classical breakdown field is $E_k \approx 32\,\mathrm{kV\,cm^{-1}}$. For higher fields, electron avalanches are formed, but their energies typically do not exceed the range of several eV, as their friction increases with energy. The electron friction increases up to an electron energy of approximately 200 eV where the critical electric field $E_c \approx 260\,\mathrm{kV\,cm^{-1}}$ is required to balance friction, as long as the approximation of the electron ensemble by classical friction is valid. For electron energies above 200 eV, the friction decreases to a minimum that is balanced by an electric field of $E_b \approx 2.8\,\mathrm{kV\,cm^{-1}}$, called the break-even field, at an electron energy of about 1 MeV.

Clearly two limitations to using a particle model with a low energy cutoff are immediately visible. First, if the electric field is above the critical electric field of $260\,\mathrm{kV\,cm^{-1}}$ ($E > E_c$) in a sufficiently large volume, the two populations of electrons with energies below and above 200 eV are strongly coupled and essentially all electrons can be accelerated into the runaway regime to 1 MeV and beyond. Second, if the electric field is below the critical field, but above the classical breakdown field ($E_k < E < E_c$), the population of electrons in the eV regime (the so-called thermal electrons) can grow strongly, and eventually tunnel into the runaway regime; we will come back to this effect below.

On the other hand, for electric field strengths below the break-even field ($E < E_b$), all electrons, regardless of initial energy, will eventually stop as the friction force of air is stronger than the accelerating force of the electric field.

Finally, when the electric field is above the break-even limit and below the classical breakdown field ($E_b < E < E_c$), the use of the energy cutoff of 50 keV (or even lower) can have strong implications: for an electron energy of 50 keV, friction and electric acceleration force balance each other when the field is $7.8\,\mathrm{kV\,cm^{-1}}$. So in classical approximation one would estimate that at lower fields the inclusion of the cutoff is justified. However, this classical approximation neglects the stochastics of the actual process. Due to the randomness of free paths and scattering events, electrons actually can tunnel into energy regimes that they could not reach in the classical approximation, an effect similar to the straggling effect discussed earlier.

Skeltved et al. (2014) have observed this effect: for all fields between 4 and $25\,\mathrm{kV\,cm^{-1}}$, they found that energy spectrum and mean energy of runaway electrons depended on the low energy cutoff, even when it was chosen between 250 eV and 1 keV. They also found – not surprisingly – that the differences become most apparent when the electric field force approaches the friction force corresponding to the low energy cutoff.

A related observation was made by Li et al. (2009) when they found electron runaway from a negative streamer even though the maximal electric field at the leader tip was well below the critical field E_c.

Future studies on how to choose the low energy cutoff for given fields are desirable to optimize computations between efficiency and accuracy.

7 Conclusions

The goal of this work is to provide standard tests for comparing the core part of Monte Carlo simulations tools available for HEAP. We focused on the propagation of electrons, positrons and photons through air, in the absence of electric and magnetic fields. We compare the output at half the CSDA range for electrons and positrons, and at two e-folding lengths (the inverse of half the attenuation coefficient) for photons. We have run these tests for 0.1, 0.4, 1.0, 10 and 40 MeV initial energy for the several codes (Geant4, EGS5, FLUKA, GRRR and MC-PEPTITA) used by the co-authors. The outputs show equivalent results, but there are impor-

tant differences one can identify. Especially the different implementations of the friction are causing observable effects. First, we see that straggling is important in the energy regime of HEAP and should be included in the simulations. Secondly, the opening angle of photon beams are very sensitive to the low energy cutoff. Thirdly, we noticed that EGS5 has an ultra-relativistic approximation for bremsstrahlung which is not appropriate in the energy regime of HEAP. Last but not least, there is a big difference in completion time between programs, mainly depending on the low energy cutoff and the synchronous implementation of the code. Adding electric fields will only increase these differences further and limit the value of the low energy cutoff. All results are published in the Supplement, and they can then be used by anyone to benchmark their custom-made codes, with the fields switched off. The next step is to provide benchmarks including fields and finding the optimal low energy cutoff for simulations in HEAP.

8 Recommendations

For future studies, we recommend the following steps.

- Check custom-made codes (where possible) against well-established general purpose codes; we provide benchmarks in the energy regime of HEAP, in the case of zero field.
- Make your custom-made code available to other researchers.
- For electrons and positrons below 1 MeV, straggling should be included.
- For electrons and positrons above 10 MeV, radiative loss should not be implemented with uniform friction.
- Photon production (due to bremsstrahlung) by electrons and positrons in the energy regime of HEAP is underestimated by EGS5.

9 Code and/or data availability

Figures of all output are available in the Supplement. All raw data, ca. 2 GB in compressed form, can be downloaded on request. In addition, the input files for reproducing the tests done in this benchmark are given for EGS5, FLUKA, Geant and GRRR, including links to the main source files. MC-PEPTITA simulations can be requested, contact David Sarria (david.sarria.89@gmail.com). MC-PEPTITA program was developed under a contract of Centre National D'Edtudes Spatiales (CNES) and Direction Générale de l'Armement (DGA), whose permissions are required in order to get access to the source code. Details of the performance tests are also available in the Supplement.

The Supplement related to this article is available online at doi:10.5194/gmd-9-3961-2016-supplement.

Author contributions. Casper Rutjes and David Sarria designed the tests with contributions of Alexander Broberg Skeltved, Alejandro Luque and Gabriel Diniz. Casper Rutjes, David Sarria, Alejandro Luque and Gabriel Diniz carried them out and discussed the differences. Casper Rutjes, David Sarria, Alexander Broberg Skeltved and Ute Ebert prepared the manuscript with contributions from all co-authors.

Acknowledgements. Working visits between the European partners were supported by the ESF research training network TEA-IS (Thunderstorm Effects on the Atmosphere-Ionosphere System). Casper Rutjes is funded by the Foundation for Fundamental Research on Matter (FOM), which is part of the Netherlands Organisation for Scientific Research (NWO). Alexander Broberg Skeltved is supported by the European Research Council under the European Union's Seventh Framework Programme (FP7/2007-2013)/ERC grant agreement 320839 and the Research Council of Norway under contracts 208028/F50, 216872/F50, and 223252/F50 (CoE). Alejandro Luque was supported by the European Research Council (ERC) under the European Union's H2020 programme/ERC grant agreement 681257 and by the Spanish Ministry of Economy and Competitiveness, MINECO under projects ESP2013-48032-C5-5-R and FIS2014-61774-EXP that include EU funding through the FEDER program. Gabriel Diniz is financial supported by the Brazilian agencies CAPES and CNPq.

Edited by: P. Jöckel
Reviewed by: A. Chilingarian and one anonymous referee

References

Adachi, T., Takahashi, Y., Ohya, H., Tsuchiya, F., Yamashita, K., Yamamoto, M., and Hashiguchi, H.: Monitoring of Lightning Activity in Southeast Asia: Scientific Objectives and Strategies, Kyoto Working Papers on Area Studies: G-COE Series, 2008.

Agostinelli, S., Allison, J., Amako, K., et al.: GEANT4: A simulation toolkit, Nucl. Instrum. Methods, A506, 250–303, doi:10.1016/S0168-9002(03)01368-8, 2003.

Andreo, P.: Monte Carlo techniques in medical radiation physics, Phys. Med. Biol., 36, 861, doi:10.1088/0031-9155/36/7/001, 1991.

Babich, L., Donskoy, E., Kutsyk, I., and Roussel-Dupré, R.: The feedback mechanism of runaway air breakdown, Geophys. Res. Lett., 32, L09809, doi:10.1029/2004GL021744, 2005.

Basaglia, T., Bell, Z., Dressendorfer, P., Larkin, A., and Pia, M.: Writing software or writing scientific articles?, in: Nuclear Science Symposium Conference Record, 2007, NSS'07, IEEE, Vol. 1, 219–226, IEEE, 2007.

Bethe, H. and Heitler, W.: On the stopping of fast particles and on the creation of positive electrons, P. Roy. Soc. Lond. A, 146, 83–112, 1934.

Böhlen, T., Cerutti, F., Chin, M., Fassò, A., Ferrari, A., Ortega, P., Mairani, A., Sala, P., Smirnov, G., and Vlachoudis, V.: The FLUKA code: developments and challenges for high energy and medical applications, Nuclear Data Sheets, 120, 211–214, 2014.

Briggs, M. S., Fishman, G. J., Connaughton, V., Bhat, P. N., Paciesas, W. S., Preece, R. D., Wilson-Hodge, C., Chaplin, V. L., Kippen, R. M., von Kienlin, A., Meegan, C. A., Bissaldi, E., Dwyer, J. R., Smith, D. M., Holzworth, R. H., Grove, J. E., and Chekhtman, A.: First results on terrestrial gamma ray flashes from the Fermi Gamma-ray Burst Monitor, J. Geophys. Res.-Space, 115, A07323, doi:10.1029/2009JA015242, 2010.

Briggs, M. S., Connaughton, V., Wilson-Hodge, C., Preece, R. D., Fishman, G. J., Kippen, R. M., Bhat, P. N., Paciesas, W. S., Chaplin, V. L., Meegan, C. A., von Kienlin, A., Greiner, J., Dwyer, J. R., and Smith, D. M.: Electron-positron beams from terrestrial lightning observed with Fermi GBM, Geophys. Res. Lett., 38, L02808, doi:10.1029/2010GL046259, 2011.

Carlson, B. E., Lehtinen, N. G., and Inan, U. S.: Constraints on terrestrial gamma ray flash production from satellite observation, Geophys. Res. Lett., 34, L08809, doi:10.1029/2006GL029229, 2007.

Carlson, B. E., Gjesteland, T., and Østgaard, N.: Terrestrial gamma-ray flash electron beam geometry, fluence, and detection frequency, J. Geophys. Res.-Space, 116, A11217, doi:10.1029/2011JA016812, 2011.

Carrier, J.-F., Archambault, L., Beaulieu, L., and Roy, R.: Validation of GEANT4, an object-oriented Monte Carlo toolkit, for simulations in medical physics, Medical Phys., 31, 484–492, 2004.

Celestin, S. and Pasko, V. P.: Energy and fluxes of thermal runaway electrons produced by exponential growth of streamers during the stepping of lightning leaders and in transient luminous events, J. Geophys Res.-Space, 116, A03315, doi:10.1029/2010JA016260, 2011.

Celestin, S., Xu, W., and Pasko, V. P.: Terrestrial gamma ray flashes with energies up to 100 MeV produced by nonequilibrium acceleration of electrons in lightning, J. Geophys. Res.-Space, 117, A05315, doi:10.1029/2012JA017535, 2012.

Chanrion, O. and Neubert, T.: Production of runaway electrons by negative streamer discharges, J. Geophys. Res.-Space, 115, doi:10.1029/2009JA014774, 2010.

Chanrion, O., Bonaventura, Z., Çinar, D., Bourdon, A., and Neubert, T.: Runaway electrons from a "beam-bulk" model of streamer: application to TGFs, Environ. Res. Lett., 9, 055003, doi:10.1088/1748-9326/9/5/055003, 2014.

Chilingarian, A., Daryan, A., Arakelyan, K., Hovhannisyan, A., Mailyan, B., Melkumyan, L., Hovsepyan, G., Chilingaryan, S., Reymers, A., and Vanyan, L.: Ground-based observations of thunderstorm-correlated fluxes of high-energy electrons, gamma rays, and neutrons, Phys. Rev. D, 82, 043009, doi:10.1103/PhysRevD.82.043009, 2010.

Chilingarian, A., Hovsepyan, G., and Hovhannisyan, A.: Particle bursts from thunderclouds: Natural particle accelerators above our heads, Phys. Rev. D, 83, 062001, doi:10.1103/PhysRevD.83.062001, 2011.

Cooray, V., Arevalo, L., Rahman, M., Dwyer, J., and Rassoul, H.: On the possible origin of X-rays in long laboratory sparks, J. Atmos. Sol.-Terr. Phys., 71, 1890–1898, 2009.

Cullen, D. E., Hubbell, J. H., and Kissel, L.: EPDL97: the Evaluated Photon Data Library, '97 Version, 1997.

Dubinova, A., Rutjes, C., Ebert, U., Buitink, S., Scholten, O., and Trinh, G. T. N.: Prediction of lightning inception by large ice particles and extensive air showers, Phys. Rev. Lett., 115, 015002, doi:10.1103/PhysRevLett.115.015002, 2015.

Dwyer, J.: A fundamental limit on electric fields in air, Geophys. Res. Lett., 30, doi:10.1029/2003GL017781, 2003.

Dwyer, J., Saleh, Z., Rassoul, H., Concha, D., Rahman, M., Cooray, V., Jerauld, J., Uman, M., and Rakov, V.: A study of X-ray emission from laboratory sparks in air at atmospheric pressure, J. Geophys. Res.-Atmos., 113, D23207, doi:10.1029/2008JD010315, 2008a.

Dwyer, J. R.: Relativistic breakdown in planetary atmospheres, Physics of Plasmas (1994–present), 14, 042901, doi:10.1063/1.2709652, 2007.

Dwyer, J. R.: The relativistic feedback discharge model of terrestrial gamma ray flashes, J. Geophys. Res.-Space, 117, doi:10.1029/2011JA017160, 2012.

Dwyer, J. R. and Smith, D. M.: A comparison between Monte Carlo simulations of runaway breakdown and terrestrial gamma-ray flash observations, Geophys. Res. Lett., 32, L22804, doi:10.1029/2005GL023848, 2005.

Dwyer, J. R., Grefenstette, B. W., and Smith, D. M.: High-energy electron beams launched into space by thunderstorms, Geophys. Res. Lett., 35, doi:10.1029/2007GL032430, 2008b.

Dwyer, J. R., Smith, D. M., and Cummer, S. A.: High-Energy Atmospheric Physics: Terrestrial Gamma-Ray Flashes and Related Phenomena, Soc. Sci. Res., 173, 133–196, doi:10.1007/s11214-012-9894-0, 2012.

Eack, K. B., Beasley, W. H., Rust, W. D., Marshall, T. C., and Stolzenburg, M.: Initial results from simultaneous observation of X-rays and electric fields in a thunderstorm, J. Geophys. Res.-Atmos., 101, 29637–29640, 1996.

Ferrari, A., Sala, P. R., Fasso, A., and Ranft, J.: FLUKA: A multi-particle transport code (Program version 2005), Tech. rep., available at: http://inspirehep.net/record/701721/files/slac-r-773.pdf (last access: 7 November 2016), 2005.

Fishman, G. J., Bhat, P., Mallozzi, R., Horack, J., Koshut, T., Kouveliotou, C., Pendleton, G., Meegan, C., Wilson, R., Paciesas, W., et al.: Discovery of intense gamma-ray flashes of atmospheric origin, Science, 264, 1313–1316, 1994.

Gurevich, A.: On the theory of runaway electrons, Sov. Phys. JETP, 12, 904–912, 1961.

Gurevich, A., Milikh, G., and Roussel-Dupre, R.: Runaway electron mechanism of air breakdown and preconditioning during a thunderstorm, Phys. Lett. A, 165, 463–468, 1992.

Hazelton, B. J., Grefenstette, B. W., Smith, D. M., Dwyer, J. R., Shao, X.-M., Cummer, S. A., Chronis, T., Lay, E. H., and Holzworth, R. H.: Spectral dependence of terrestrial gamma-ray flashes on source distance, Geophys. Res. Lett., 36, L01108, doi:10.1029/2008GL035906, 2009.

Heck, D., Knapp, J., Capdevielle, J., Schatz, G., and Thouw, T.: CORSIKA: A Monte Carlo code to simulate extensive air showers, Vol. 6019, FZKA, available at: http://inspirehep.net/record/469835/files/FZKA6019.pdf (last access: 7 November 2016), 1998.

Hirayama, H., Namito, Y., Nelson, W. R., Bielajew, A. F., Wilderman, S. J., and Michigan, U.: The EGS5 code system, Tech. rep., USA, Department of Energy, 2005.

Karshenboim, S. G.: Precision study of positronium: Testing bound state QED theory, Int. J. Modern Phys. A, 19, 3879–3896, 2004.

Kochkin, P., Nguyen, C., Van Deursen, A., and Ebert, U.: Experimental study of hard x-rays emitted from metre-scale positive discharges in air, J. Phys. D, 45, 425202, doi:10.1088/0022-3727/45/42/425202, 2012.

Kochkin, P., Van Deursen, A., and Ebert, U.: Experimental study on hard x-rays emitted from metre-scale negative discharges in air, J. Phys. D, 48, 025205, doi:10.1088/0022-3727/48/2/025205, 2015.

Kochkin, P., Köhn, C., Ebert, U., and van Deursen, L.: Analyzing x-ray emissions from meter-scale negative discharges in ambient air, Plasma Sources Science and Technology, 25, 044002, doi:10.1088/0963-0252/25/4/044002, 2016.

Köhn, C. and Ebert, U.: Calculation of beams of positrons, neutrons, and protons associated with terrestrial gamma ray flashes, J. Geophys. Res.-Atmos., 120, 1620–1635, 2015.

Kohn, C., Ebert, U., and Mangiarotti, A.: The importance of electron–electron bremsstrahlung for terrestrial gamma-ray flashes, electron beams and electron–positron beams, J. Phys. D, 47, 252001, doi:10.1088/0022-3727/47/25/252001, 2014.

Kostyrya, I., Tarasenko, V., Tkachev, A., and Yakovlenko, S.: X-ray radiation due to nanosecond volume discharges in air under atmospheric pressure, Tech. Phys., 51, 356–361, 2006.

Li, C., Ebert, U., and Hundsdorfer, W.: 3D hybrid computations for streamer discharges and production of runaway electrons, J. Phys. D, 42, 202003, doi:10.1088/0022-3727/42/20/202003, 2009.

Luque, A.: Relativistic Runaway Ionization Fronts, Phys. Rev. Lett., 112, 045003, doi:10.1103/PhysRevLett.112.045003, 2014.

Marisaldi, M., Fuschino, F., Pittori, C., Verrecchia, F., Giommi, P., Tavani, M., Dietrich, S., Price, C., Argan, A., Labanti, C., Galli, M., Longo, F., Del Monte, E., Barbiellini, G., Giuliani, A., Bulgarelli, A., Gianotti, F., Trifoglio, M., and Trois, A.: The first AGILE low-energy (< 30 MeV) Terrestrial Gamma-ray Flashes catalog, Geophys. Res. Abstr., EGU2014-A-11326, EGU General Assembly 2014, Vienna, Austria, 2014.

McCarthy, M. and Parks, G.: Further observations of X-rays inside thunderstorms, Geophys. Res. Lett., 12, 393–396, 1985.

Moss, G. D., Pasko, V. P., Liu, N., and Veronis, G.: Monte Carlo model for analysis of thermal runaway electrons in streamer tips in transient luminous events and streamer zones of lightning leaders, J. Geophys. Res.-Space, 111, A02307, doi:10.1029/2005JA011350, 2006.

Nelson, W. R., Hirayama, H., and Rogers, D. W.: EGS4 code system, Tech. rep., Stanford Linear Accelerator Center, Menlo Park, CA, USA, 1985.

Noggle, R., Krider, E., and Wayland, J.: A search for X rays from helium and air discharges at atmospheric pressure, J. Appl. Phys., 39, 4746–4748, 1968.

Østgaard, N., Gjesteland, T., Stadsnes, J., Connell, P., and Carlson, B.: Production altitude and time delays of the terrestrial gamma flashes: Revisiting the Burst and Transient Source Experiment spectra, J. Geophys. Res.-Space, 113, A02307, doi:10.1029/2007JA012618, 2008.

Pancheshnyi, S., Biagi, S., Bordage, M., Hagelaar, G., Morgan, W., Phelps, A., and Pitchford, L.: The LXCat project: Electron scattering cross sections and swarm parameters for low temperature plasma modeling, Chem. Phys., 398, 148–153, 2012.

Perkins, S. T., Cullen, D. E., and Seltzer, S. M.: Tables and graphs of electron-interaction cross sections from 10 eV to 100 GeV derived from the LLNL Evaluated Electron Data Library (EEDL), $Z = 1$ to 100, Tech. rep., available at: http://www.osti.gov/scitech/biblio/10121050 (last access: 7 November 2016), 1991.

Rep'ev, A. and Repin, P.: Spatiotemporal parameters of the X-ray radiation from a diffuse atmospheric-pressure discharge, Tech. Phys., 53, 73–80, 2008.

Salvat, F., Fernández-Varea, J. M., and Sempau, J.: PENELOPE-2011: A Code System for Monte Carlo Simulation of Electron and Photon Transport, NUCLEAR ENERGY AGENCY, Organisation for Economic Co-operation and Development, Universitat de Barcelona Spain, 2011.

Sarria, D., Blelly, P.-L., and Forme, F.: MC-PEPTITA: a Monte Carlo model for Photon, Electron and Positron Tracking In Terrestrial Atmosphere. Application for a Terrestrial Gamma-ray Flash, J. Geophys. Res.-Space, 120, 3970–3986, doi:10.1002/2014JA020695, 2015.

Sarria, D., Blelly, P.-L., Briggs, M. S., and Forme, F.: Studying the time histogram of a terrestrial electron beam detected from the opposite hemisphere of its associated TGF, J. Geophys. Res.-Space, 121, 4698–4704, doi:10.1002/2015JA021881, 2016.

Schellart, P., Trinh, T., Buitink, S., Corstanje, A., Enriquez, J., Falcke, H., Hörandel, J., Nelles, A., Rachen, J., Rossetto, L., Scholten, O., ter Veen, S., Thoudam, S., Ebert, U., Koehn, C., Rutjes, C., Alexov, A., Anderson, J. M., Avruch, I. M., Bentum, M. J., Bernardi, G., Best, P., Bonafede, A., Breitling, F., Broderick, J. W., Brüggen, M., Butcher, H. R., Ciardi, B., de Geus, E., de Vos, M., Duscha, S., Eislöffel, J., Fallows, R. A., Frieswijk, W., Garrett, M. A., Grießmeier, J., Gunst, A. W., Heald, G., Hessels, J. W. T., Hoeft, M., Holties, H. A., Juette, E., Kondratiev, V. I., Kuniyoshi, M., Kuper, G., Mann, G., McFadden, R., McKay-Bukowski, D., McKean, J. P., Mevius, M., Moldon, J., Norden, M. J., Orru, E., Paas, H., Pandey-Pommier, M., Pizzo, R., Polatidis, A. G., Reich, W., Röttgering, H., Scaife, A. M. M., Schwarz, D. J., Serylak, M., Smirnov, O., Steinmetz, M., Swinbank, J., Tagger, M., Tasse, C., Toribio, M. C., van Weeren, R. J., Vermeulen, R., Vocks, C., Wise, M. W., Wucknitz, O., and Zarka, P.: Probing atmospheric electric fields in thunderstorms through radio emission from cosmic-ray-induced air showers, Phys. Rev. Lett., 114, 165001, doi:10.1103/PhysRevLett.114.165001, 2015.

Sempau, J., Sanchez-Reyes, A., Salvat, F., ben Tahar, H. O., Jiang, S., and Fernández-Varea, J.: Monte Carlo simulation of electron beams from an accelerator head using PENELOPE, Phys. Med. Biol., 46, 1163, doi:10.1088/0031-9155/46/4/318, 2001.

Shao, T., Zhang, C., Niu, Z., Yan, P., Tarasenko, V. F., Baksht, E. K., Burahenko, A. G., and Shut'ko, Y. V.: Diffuse discharge, runaway electron, and x-ray in atmospheric pressure air in an inhomogeneous electrical field in repetitive pulsed modes, Appl. Phys. Lett., 98, 021503, doi:10.1063/1.3540504, 2011.

Skeltved, A. B., Østgaard, N., Carlson, B., Gjesteland, T., and Celestin, S.: Modeling the relativistic runaway electron avalanche and the feedback mechanism with GEANT4, J. Geophys. Res.-Space, 119, 9174–9191, doi:10.1002/2014JA020504, 2014.

Stankevich, Y. L. and Kalinin, V.: Fast electrons and x radiation during the initial stages of an impulse spark discharge in air, Dokl. Akad. Nauk SSSR, 177, 72–73, 1967.

Tarasenko, V. F., Baksht, E. K., Burachenko, A. G., Kostyrya, I. D., Lomaev, M. I., and Rybka, D. V.: Generation of supershort

Paper III

7.3 Constraints to do realistic modeling of the electric field ahead of the tip of a lightning leader

Alexander Broberg Skeltved, Nikolai Østgaard, Andrew Mezentsev, Nikolai Lehtinen and Brant Carlson

Journal of Geophysical Research: Atmospheres 122, doi:10.1002/2016JD026206, (2017)

AGU PUBLICATIONS

JGR

Journal of Geophysical Research: Atmospheres

RESEARCH ARTICLE
10.1002/2016JD026206

Key Points:
- To define realistic constraints on the electric field created by lightning leaders
- To give an estimate of the effect that the leader field has on multiplication and acceleration of energetic electrons
- To discuss if the leader field scenario can explain the production of TGFs

Correspondence to:
A. B. Skeltved,
Alexander.Skeltved@uib.no

Citation:
Skeltved, A. B., N. Østgaard, A. Mezentsev, N. Lehtinen, and B. Carlson (2017), Constraints to do realistic modeling of the electric field ahead of the tip of a lightning leader, *J. Geophys. Res. Atmos.*, *122*, doi:10.1002/2016JD026206.

Received 8 NOV 2016
Accepted 7 JUL 2017
Accepted article online 21 JUL 2017

Constraints to do realistic modeling of the electric field ahead of the tip of a lightning leader

Alexander Broberg Skeltved[1], Nikolai Østgaard[1], Andrew Mezentsev[1], Nikolai Lehtinen[1], and Brant Carlson[1,2]

[1]Birkeland Centre for Space Science, Institute of Physics and Technology, University of Bergen, Bergen, Norway, [2]Physics and Astronomy, Carthage College, Kenosha, Wisconsin, USA

Abstract Several computer models exist to explain the observation of terrestrial gamma-ray flashes (TGFs). Some of these models estimate the electric field ahead of lightning leaders and its effects on electron acceleration and multiplication. In this paper, we derive a new set of constraints to do more realistic modeling. We determine initial conditions based on in situ measurements of electric field and vertical separation between the main charge layers of thunderclouds. A maximum electric field strength of 50 kV/cm at sea level is introduced as the upper constraint for the leader electric field. The threshold for electron avalanches to develop of 2.86 kV/cm at sea level is introduced as the lower value. With these constraints, we determine a region where acceleration and multiplication of electrons occur. The maximum potential difference in this region is found to be ~52 MV, and the corresponding number of avalanche multiplication lengths is ~3.5. We then quantify the effect of the ambient electric field compared to the leader field at the upper altitude of the negative tip. Finally, we argue that only leaders with the highest potential difference between its tips (~600 MV) can be candidates for the production of TGFs. However, with the assumptions we have used, these cannot explain the observed maximum energies of at least 40 MeV. Open questions with regard to the temporal development of the streamer zone and its effect on the shape of the electric field remain.

1. Introduction

Terrestrial gamma-ray flashes (TGFs) are short, intense, very energetic bursts of bremsstrahlung photons that are produced by relativistic electrons. Two leading scenarios have been presented to explain how free electrons can be accelerated to relativistic energies and multiplied in the thundercloud electric fields.

1. *Wilson* [1925] presented the idea that high-energy electrons, such as cosmic ray secondaries, in the presence of a strong electric field can be accelerated to overcome the friction force in air. These electrons then become runaway electrons. It is well established that the ambient field in thunderclouds can be sufficiently strong for this to occur. *Gurevich et al.* [1992] later proposed that runaway electrons can undergo further multiplication, primarily through the Møller scattering process, producing Relativistic Runaway Electron Avalanches (RREAs). In addition to high-energy electrons, also, positrons and high-energy photons will be created and some will backscatter and create seed particles for new RREAs [*Dwyer*, 2003, 2012; *Skeltved et al.*, 2014]. This multiplication of RREAs is called the feedback mechanism. Thus, this scenario is explained by the ability of the ambient field to accelerate electrons enough to overcome the friction force of air over the vertical distance between the main charge layers in thunderclouds.
2. *Moss et al.* [2006] proposed that acceleration and multiplication of electrons can occur in the strong inhomogeneous electric field created ahead of a lightning leader. They also suggested that seed electrons in this scenario are thermal electrons accelerated in streamer tips during the very early stage of streamer development. Modeling results suggest that the electric fields in streamer tips are indeed sufficient to accelerate electrons to average energies of ~65 keV [*Celestin and Pasko*, 2011]. Several studies have reported modeling results of this scenario and concluded that it may be sufficient to explain the number of electrons and gamma rays that has been observed [*Carlson et al.*, 2010; *Celestin and Pasko*, 2011; *Xu et al.*, 2012; *Köhn and Ebert*, 2015]. The effect of feedback in the leader field has also been discussed [*Dwyer*, 2007; *Carlson*, 2009] and was shown to depend on the geometry and the charge density in the tip of the leader. Results from *Köhn et al.* [2017] indicate that the effect of feedback could be important depending on the strength and shape of the leader electric field.

AGU Journal of Geophysical Research: Atmospheres 10.1002/2016JD026206

Table 1. A Comparison of the Two Scenarios and the Role of the Important Mechanisms[a]

Scenarios	Runaway Electrons	RREAs	Feedback
(1) Ambient field	Any, including thermal	Yes	Yes
(2) Leader field	Thermal	Yes	Yes (< ambient)

[a]Note that the primary difference is the electric field configuration, which is uniform in scenario 1 and highly nonuniform in scenario 2. In addition, although feedback has been shown to be present in both models, the effect is likely larger for scenario 1 than for scenario 2.

Notice that there are two primary differences between the scenarios. The runaway electrons of scenario 1 can be supplied from any source of above ~10 keV, whereas scenario 2 relies on the acceleration of thermal electrons. The electric field is relatively uniform and extended to kilometer scale in scenario 1 but highly nonuniform and localized to hundred meter scale in scenario 2. In both scenarios, however, extreme thundercloud conditions have been assumed to fully account for the observations [*Dwyer*, 2003; *Xu et al.*, 2012; *Köhn and Ebert*, 2015; *Celestin et al.*, 2012]. Table 1 summarizes the similarities and differences between the two scenarios. In reality, when both the ambient field and local enhancements exist, the question is as follows: what is their relative importance for TGF production?

The purpose of this paper is to establish realistic constraints to derive the effects of the leader electric field on the acceleration and multiplication of high-energy electrons. We first discuss observable properties of TGFs then present a description of relevant properties of positive intracloud leader (+IC). We go on to present the initial conditions of existing models and how these models estimate the leader electric field. It will then be shown that the strength and shape of the estimated electric fields depend largely on the method used to calculate them. This result will be shown to have important implications for the region where acceleration and multiplication of high-energy electrons can occur. We then present the assumption that the positive end of the channel branches and develops horizontally in the negative charge region. The system of branched channels can then be approximated as a partly conducting plane relative to the negative end of the channel. Effectively, this explains how the potential difference between a point just ahead of the leader and the ambient potential can be increased, but not more than doubled. Finally, we use the new constraints to make estimates of the maximum energy and multiplication rate of high-energy electrons.

2. Properties of TGFs and of Their Source Electrons

An extensive overview of TGF properties and related phenomena is found in *Dwyer et al.* [2012]. In this section we summarize the parameters that are important from the perspective of the production mechanisms.

TGFs are submillisecond bursts of photons with maximum energies of up to at least 40 MeV [*Smith et al.*, 2005; *Briggs et al.*, 2010; *Marisaldi et al.*, 2010]. Comparisons between modeling results and the average photon energy spectrum obtained from satellite measurements have indicated that TGFs originate from inside thundercloud regions in the Earth's atmosphere at altitudes below 21 km [*Dwyer and Smith*, 2005; *Carlson et al.*, 2007; *Østgaard et al.*, 2008; *Gjesteland et al.*, 2010]. Measurements of radio waves produced by lightning and their association with TGFs have indicated that the typical production altitude is actually between 10 km and 15 km altitude [*Cummer et al.*, 2005, 2011, 2015; *Gjesteland et al.*, 2015; *Shao et al.*, 2010; *Lu et al.*, 2010]. The energy distribution of the photons has been explained by an attenuated bremsstrahlung spectrum indicating that the source are high-energy electrons [*Lehtinen et al.*, 1996]. *Skeltved et al.* [2014] also found that the ratio of high-energy (>100 keV) electrons to photons is between 1 and 10. Finally, better search algorithms [*Østgaard et al.*, 2012, 2015] and new detector configurations [*Marisaldi et al.*, 2015] have shown that TGFs are more common than previously thought.

To reach the numbers and energies that have been inferred from measurements, high-energy (>10 keV) electrons must be present in a region with a strong electric field. Such electrons are thought to be thermal electrons that have been accelerated in the strong electric field near the tips of streamers [*Moss et al.*, 2006] or the product of cosmic ray secondary particles [*Wilson*, 1925]. Note that thermal electrons refer to the seed electrons that have been accelerated from energies in the eV range to become runaway electrons in the tens of keV range; this process can also be referred to as thermal acceleration. Further multiplication is dominated

AGU Journal of Geophysical Research: Atmospheres 10.1002/2016JD026206

by elastic Møller scattering of electrons in electric fields stronger than the RREA threshold, E_{RREA}=2.86 kV/cm at sea level [*Coleman and Dwyer*, 2006]. The RREA threshold is slightly above the minimum stopping power of air, since the electrons do not go in exactly a straight line. This multiplication process is the RREA mechanism and can be described by the following equation [*Gurevich et al.*, 1992; *Gurevich and Zybin*, 2001]:

$$N_{RREA} = N_o \cdot e^{L/\lambda(E)} \tag{1}$$

where N_{RREA} is the total number of electrons from the multiplication of N_o seed electrons, L is the length of the multiplication region, and $\lambda(E)$ is the avalanche (*e*-folding) length in a homogeneous electric field, E. The derivation of equation (1) can be found in *Gurevich et al.* [1992] and *Skeltved et al.* [2014]. For electric field strengths between the conventional breakdown threshold, E_{th} = 32 kV/cm, and the RREA threshold E_{RREA}, the avalanche length is given by the following two functions

$$\lambda(E) \approx \frac{7.3 \times 10^3 \text{kV}}{E - 2.75 \text{kV/cm}} \tag{2}$$

in the range 32kV/cm > E > 3kV/cm and

$$\lambda(E) \approx \frac{5.1 \times 10^3 \text{kV}}{E - 2.85 \text{kV/cm}} \tag{3}$$

in the range 3 kV/cm > E > 2.86 kV/cm. These functions are based on modeling results [*Dwyer*, 2003; *Coleman and Dwyer*, 2006] and have been validated by *Dwyer* [2012] and *Skeltved et al.* [2014]. The total number of avalanche lengths N_λ in a uniform electric field E, over a distance L, is then

$$N_\lambda = \frac{L}{\lambda(E)}. \tag{4}$$

In a strongly nonuniform electric field, such as that ahead of a lightning leader (see section 3), the electric field, $E(l)$, depends on the distance, l. The total number of avalanche lengths then becomes

$$N_\lambda = \int_{l_1}^{l_2} \frac{dl}{\lambda(E(l))}, \tag{5}$$

where $\lambda(E(l))$ is defined by equations (2) and (3).

In order to produce the observed bremsstrahlung spectrum of TGFs, the energy distribution of the RREAs must reach a steady state with maximum energies greater than that of TGFs, which is up to at least 40 MeV [*Marisaldi et al.*, 2010].

3. The +IC Leader and the Effects of Its Electric Field

When a lightning leader develops in the ambient electric field of a thundercloud, it creates its own strong electric field ahead of its tip. To understand how this may be important for the production of TGFs, a short description of positive intracloud (+IC) leaders will be given.

The thundercloud can be approximated by three vertically stacked charge layers [*Williams*, 1989]. A weak lower positive charge layer, a strong main negative (MN) charge layer, and a slightly weaker upper positive (UP) charge layer. The MN charge layer is thin, with a higher charge density [*Marshall and Stolzenburg*, 2001; *Rakov and Uman*, 2003] and is centered where the temperature is between −10° and −25°C, typically from 4 km to 6 km altitude [*Rakov and Uman*, 2003, p. 75]. The UP charge layer is less dense, but more vertically extended, and is typically centered at altitudes between 10 km and 14 km [*Rakov and Uman*, 2003, p. 76]. The maximum altitude of thunderclouds is determined by the height of the tropopause that, depending on altitude and season, can reach 17 km [e.g., *Pan and Munchak*, 2011].

The amount of charge in the charge layers and the separation between them determines the strength of the ambient electric field. *Marshall and Rust* [1991], *Marshall and Stolzenburg* [1996, 2001], and *Stolzenburg et al.* [2007] have presented electric field soundings through a range of thunderstorms. From their measurements it can be seen that the mean strength of the ambient electric field between the main charge regions is

AGU Journal of Geophysical Research: Atmospheres 10.1002/2016JD026206

roughly between 0.2 kV/cm and 0.5 kV/cm. These values are consistent with other studies [*Rakov and Uman*, 2003; *Coleman*, 2003]. In *Marshall and Stolzenburg* [2001], cloud tops where measured to be from 9 to 12.5 km and the gap between the main charge regions extended between 2 and 5 km vertically. The negative charge layer was located between 5 km and 7 km altitude. These values are close to the typical values from *Rakov and Uman* [2003]. Although the peak strength of the ambient electric field can reach values stronger than the RREA threshold, the mean values are typically weaker [*Stolzenburg et al.*, 2007]. Thus, for altitudes closer to 14 km the mean ambient field can be expected to be less than the RREA threshold $E_{\mathrm{RREA}}(14) = 0.48$ kV/cm. By integrating the electric field over the vertical extension, the potential difference between the charge layers can be found. *Marshall and Stolzenburg* [2001] investigated the potential differences, also using electric field soundings through thunderstorms. The largest potential difference they found was around 130 MV and occurred between 6.5 and 9.9 km altitude.

IC leaders are initiated when the electric field exceeds the conventional breakdown threshold, $E_{\mathrm{th}} = 32$ kV/cm at sea level. Typically, this can occur in a localized region just above the MN charge region. The IC leader is characterized as a highly conductive plasma channel that develops to a vertical length, L, of a few kilometers and has a radius, r, of approximately 1 cm [*Cooray*, 2015, p. 250], sea level equivalent. IC leaders are bidirectional, with charge of opposite polarity concentrated at the two ends of the channel. As the channel develops in the ambient electric field of the cloud, the amount of charge in each end increases. However, the total charge on the leader remains zero [*Kasemir*, 1960]. After initiation, the leader develops until it spans the gap between the two charge layers. The channel is then discharged, sometimes in several consecutive discharge processes, where also branching of the channels in the charge regions can occur. The IC lightning, as described here, is believed to be the most common type of lightning flash [*Rakov and Uman*, 2003, p. 321].

TGFs have been associated with radio signals generated by lightning discharges [*Inan et al.*, 1996]. In particular, a close relationship between TGFs and +IC lightning, which develop in a stepped manner transporting electrons from the MN charge layer toward the UP charge layer, has been reported [*Cummer et al.*, 2005; *Stanley et al.*, 2006; *Shao et al.*, 2010; *Lu et al.*, 2010; *Cummer et al.*, 2011; *Østgaard et al.*, 2013; *Cummer et al.*, 2015].

If one approximates the leader channel as perfectly conducting, the induced charge will distribute itself at the surface of the channel to exactly oppose the ambient electric field E_o. The electric potential is then uniform through the center of the leader and accumulates ahead of the tips. In reality there will be a small potential drop along the channel due to the finite conductivity. This is not taken into account in this study. The potential difference, ΔU_{tip}, between the tip of a perfectly conducting channel and the ambient potential, is equal to the potential difference from the center of the channel to the tips [*Bazelyan and Raizer*, 2000, p. 54], which is given as

$$\Delta U_{\mathrm{tip}} = \frac{1}{2}\int_{h_o}^{h_1} E_o(h)\mathrm{d}h = \frac{E_o^{av}\cdot L}{2}, \tag{6}$$

where h_o and h_1 are the lower an upper altitudes of the channel and $E_o(h)$ is the ambient electric field at altitude h. This approximation is consistent with previous studies [*Celestin and Pasko*, 2011; *Xu et al.*, 2012, 2015; *Celestin et al.*, 2015; *Mallios et al.*, 2013; *Pasko*, 2013; *Köhn and Ebert*, 2015].

In the region ahead of the tips, where the electric field is above the conventional breakdown threshold E_{th}, streamers are continuously initiated. Streamers are small plasma channels of low conductivity that carry a high density of electrons at their tip and leave behind ions and free electrons in their wake. At the positive end of the leader, positive streamers are created by electron avalanches directed toward the streamer tips (due to the polarity of the electric field). The positive channel therefore develops continuously at a speed of roughly $\sim 10^6$ m/s. At the negatively charged leader tip, the negative streamers are created by electron avalanches propagating outward, leading to a stepped development that is an order of magnitude slower (on average $\sim 10^5$ m/s). During the outward expansion of the streamers, a leader stem typically forms at a distance of between several tens [*Rakov and Uman*, 2003] to hundreds [*Cummer et al.*, 2015] of meters ahead of the channel. The formation of the leader stem is still poorly understood. The leader stem is also bidirectional, with a positive channel that develops toward the main leader tip and a negative end that develops in the opposite direction. Both are preceded by smaller streamer zones of their own. When the positive secondary channel attaches to the main channel, a discharge wave redistributes the charge on the leader channel such that the tip of the former leader stem becomes the new leader tip [*Bazelyan and Raizer*, 2000, pp. 197–198]. How fast the potential is increased on the new tip is not known.

AGU Journal of Geophysical Research: Atmospheres 10.1002/2016JD026206

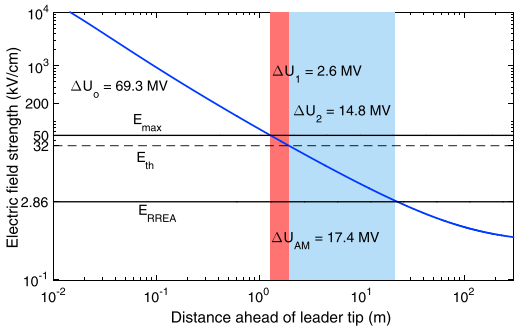

Figure 1. The electric field of a capped channel of 4 km length, 1 cm radius immersed in an ambient field of 0.5 kV/cm. The solid black lines indicate the maximum field at the leader tip, $E_{max} = 50$ kV/cm, and the RREA threshold, $E_{RREA} = 2.86$ kV/cm. The dashed line indicates the conventional breakdown threshold, $E_{th} = 32$ kV/cm, sea level equivalent. The colored areas cover the AM region, red for $E_{max} > E \geq E_{th}$ and blue for $E_{th} > E \geq E_{RREA}$ (equations (2) and (3)). ΔU_0, ΔU_1, and ΔU_2 denote the potential differences in the very high field region $E > E_{max}$ and the AM regions, respectively.

Modeling results have indicated that the electric field at the tip of streamers can reach values of ~10 E_{th}, which thereby is one of the unique circumstances when low-energy electrons can be accelerated to runaway energies [*Moss et al.*, 2006]. *Celestin and Pasko* [2011] estimated that roughly one out of a hundred low-energy electrons can be accelerated to an average energy of 65 keV. *Moss et al.* [2006] also proposed that further acceleration can occur in the weaker but more extended leader electric field. The presence of streamers and thus of charged particles increases the conductivity in the streamer zone significantly and thereby limits the strength of leader electric field. As is explained in *Bazelyan and Raizer* [2000, p. 68], the electric field cannot exceed the ionization threshold by much, because any excess charge will quickly reduce the field and stabilize it closer to the conventional breakdown threshold E_{th}. They also discussed laboratory experiments that have shown the maximum field, E_{max}, at the tip of a leader channel with radius ~1 cm to be roughly $1.5 \cdot E_{th} \sim 50$kV/cm. The maximum electric field that can exist ahead of a lightning leader is therefore likely to depend on how quickly the potential on the new tip increases [*Celestin and Pasko*, 2011] and on how fast screening due to ionization occurs. It is generally believed that after the initial stage of potential transfer, called the corona flash stage, the electric field in the streamer zone stabilizes close to the field required to sustain negative streamer development, which is ~12.5 kV/cm at sea level [*Moss et al.*, 2006].

3.1. Introducing Electric Field Constraints

Similar to previous models, we consider a static picture of the leader, when all the potential has been transferred to the new tip [*Celestin and Pasko*, 2011; *Celestin et al.*, 2012, 2015; *Xu et al.*, 2012, 2015; *Köhn and Ebert*, 2015]. To create a self-consistent model that includes the effects of a developing streamer zone on the electric field is beyond the scope of this study. However, to avoid unrealistically strong electric fields, we limit the maximum electric field strength to an upper limit of $E_{max} = 50$ kV/cm, at sea level density and pressure. Note that the screening of the electric field inside the streamer zone may also increase the electric field at the edge and thereby further complicate the system. This effect has not been considered. This limit is in accordance with the arguments presented in the previous section and with *Bazelyan and Raizer* [2000, p. 68], *Celestin and Pasko* [2011], and *Celestin et al.* [2015]. Furthermore, we assume that the seed electrons are accelerated from eV energies to keV energies in the tips of streamers [*Celestin and Pasko*, 2011]. The initial position of these seed electrons, after acceleration, is then assumed to be at the position that corresponds to the upper boundary of the electric field, E_{max}. In order for RREAs to be sustained, the electric field strength must also exceed the RREA threshold, $E_{RREA} = 2.86$ kV/cm at sea level [*Gurevich et al.*, 1992; *Dwyer*, 2003], below which even the high-energy particles (>1 MeV) will quickly stop. Thus, the region ahead of the leader tip where the electric field falls from E_{max} to E_{RREA} will be called the Acceleration and Multiplication (AM) region hereafter. In Figure 1, we present the sum of the electric field created by the leader and the ambient electric field (see section 4 for description of the leader electric field). The horizontal solid and dashed lines indicate the electric field thresholds, and the AM region is shown as the red and blue areas, where the red area indicates electric fields between $E_{max} > E > E_{th}$ and the blue area indicate the electric fields between $E_{th} > E > E_{RREA}$ (equations (2) and (3)). If the electric field created by the leader is $E(l)$ (see description in section 4), and the ambient electric field is E_o at the upper altitude of the leader, the potential difference ΔU in a region ahead of the leader can then be calculated by

$$\Delta U = \int_{l_1}^{l_2} E(l)\mathrm{d}l + E_o \cdot (l_2 - l_1) . \quad (7)$$

where l_1 and l_2 are the distances to the boundaries of the region.

AGU Journal of Geophysical Research: Atmospheres 10.1002/2016JD026206

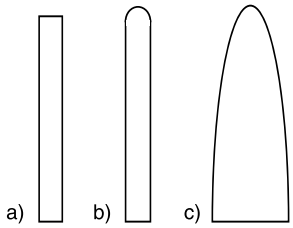

Figure 2. The geometries used to approximate the leader channel. (a) A long flat-ended channel. (b) A channel with caps. (c) An ellipsoid. Note that the sketch is not to scale and only the upper half of the channel is depicted.

4. Existing Computer Models

In the preceding sections we have described how the strong electric field created by +IC leaders may produce TGFs. We will now describe the estimated electric fields and their corresponding potential differences and present the initial conditions that have been used in earlier studies. In this context, there are four important issues to consider: (1) the geometry of the leader channel (shape of the tip, vertical length, and radius); (2) the ambient electric field, which combined with the length also defines the potential difference between the tips of the leader channel; (3) the upper altitude of the leader, *h*; and (4) how close to the leader tip the seed electrons can be initiated.

To approximate the leader channel, it is common to consider a perfectly conducting object immersed in an ambient electric field. In existing studies this is usually either a long thin wire with flat ends [*Celestin and Pasko*, 2011; *Xu et al.*, 2012; *Celestin et al.*, 2012; *Xu et al.*, 2015; *Mallios et al.*, 2013; *Pasko*, 2013; *Celestin et al.*, 2015] or an ellipsoid with a curvature radius of 1 cm at the tip [*Köhn and Ebert*, 2015]. In order to avoid confusion between a physical wire and the leader channel that may act similar to a wire, we will use the term channel throughout this paper. The ellipsoid has the advantage of having an analytical solution [*Landau and Lifshitz*, 1960, pp. 20–27] and also the disadvantage of a geometry less similar to a natural leader channel. For the flat-ended channel the numerical method of moments has been used [*Balanis*, 2012, pp. 679–691]. See Appendix A for the general method of solving for the charge distribution on a cylindrical symmetric conducting object. Using this charge distribution, one can calculate the electric field, *E*, created by the leader at an arbitrary point in space:

$$E(\mathbf{r}) = \frac{1}{4\pi\epsilon_0}\int_S \frac{\sigma(\mathbf{r}')\mathrm{d}s}{|\mathbf{r},\mathbf{r}'|^2}, \tag{8}$$

where σ is the calculated charge density, integration is over the conductor surface, and $\mathbf{r}$ is a point on the axis ahead of the channel tip. In this paper, we use the stable "surface" method of moments. In this approach, one chooses both the observation points and source points on the surface [*Harrington*, 1993, pp. 28–33], when estimating the charge distribution, as opposed to having observation points on the center axis of the channel [*Balanis*, 2012, pp. 679–691]. In Appendix A, section A2, we describe both methods. Contrary to the latter [*Balanis*, 2012], the first approach [*Harrington*, 1993] gives a stable solution for element sizes smaller than the radius of the channel. The stability of the two methods is discussed in Appendix A, section A3. The results presented in this paper will be calculated for a channel with capped tips. The caps will be half spheres with radii equal to the radius of the channel in order to make the geometry at the channel tip more realistic. Note that we also use the stable method of moments to solve for the flat-ended channel in section 5.1. The geometries at the tips of the channels are illustrated in Figure 2.

Celestin and Pasko [2011] used an ambient electric field of 0.2 kV/cm and a length of 1 km, giving a potential difference at the tip, between the leader and the ambient potential, of $\Delta U_{\mathrm{tip}} = 10$ MV (equation (6)). The model by *Celestin and Pasko* [2011] is capable of simulating the acceleration of electrons to runaway energies but does not include a full-scope simulation of the production of TGFs. *Xu et al.* [2012, 2015] used a 4 km lightning leader immersed in an ambient field of 0.5 kV/cm, which corresponds to a total potential difference over the vertical length of the leader of 200 MV and a potential difference at the tip $\Delta U_{\mathrm{tip}} = 100$ MV. They initiate the electrons at 30 cm from the tip, where we calculate the electric field to be 263.3 kV/cm based on the leader parameters from *Xu et al.* [2012] but using the stable method of moments. The maximum field corresponds to roughly 8 times the conventional breakdown threshold and 5 times the maximum field strength described in *Bazelyan and Raizer* [2000, p. 68], at sea level. *Köhn and Ebert* [2015] used the same parameters as *Xu et al.* [2012] but calculated the electric field using the analytical solution of an ellipsoid. They also initiated the electrons at 30 cm from the leader tip, which corresponds to a stronger electric field of $E_{\mathrm{max}} = 283.0$ kV/cm due to the geometry. In addition, they perform their simulations at 16 km altitude, which lead to a significantly higher maximum field to breakdown threshold ratio $E_{\mathrm{max}}/E_{\mathrm{th}}(16) \approx 74$, which is rather extreme. In this electric field,

AGU Journal of Geophysical Research: Atmospheres 10.1002/2016JD026206

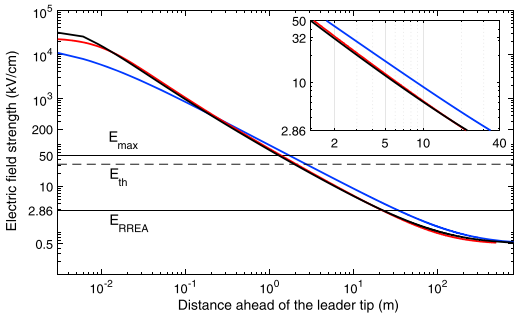

Figure 3. A comparison of the electric field calculated along the center axis ahead of a perfectly conducting channel of 4 km length and 1 cm radius immersed in an ambient electric field of 0.5 kV/cm. The capped cylinder is indicated by the black line, the flat-ended channel is red, and the ellipsoid is blue. The stable method of moments has been used for the red and black curve. The solid horizontal lines correspond to the threshold field strengths E_{max} and E_{RREA}, and the dashed line is the conventional breakdown threshold E_{th}. In the smaller panel, we have zoomed in on the AM region, the range between E_{max} and E_{RREA}. Note that although the field is directed toward the leader tip, the field strength is presented as positive to make the figure more presentable.

they are able to simulate the acceleration of electrons from 0.1 eV to tens of MeV. Note also that an ambient electric field of 0.5 kV/cm at 16 km altitude corresponds to $\sim 1.45 \cdot E_{RREA}$, which is also much larger than typical measurements suggest. *Celestin et al.* [2015] considered five cases with potential differences between the leader tips that range from 10 MV to 600 MV, which is 5 MV to 300 MV from the center to the tip. The length of the channels was assumed to be from 1 km to 6 km, and they used the same constraints on the electric field that we present in this paper. In the case presented by *Celestin et al.* [2012], they used a leader length of 3.5 km and an ambient electric field of 2.0 kV/cm, which gives a total potential difference over the vertical length of the leader of 700 MV and $\Delta U_{tip} = 350$ MV ahead of its tip. They initiated the seed electrons as close as 15 cm from the leader tip, where we calculate the electric field to be 2152.4 kV/cm (using the stable method of moments), which is roughly 60 times conventional breakdown threshold at sea level. Note that in *Celestin et al.* [2012], they acknowledged that the assumed electric fields are rather extreme.

5. Results

5.1. Dependence of the Electric Field on the Channel Shape

Different methods have been used to estimate the electric field ahead of the leader channel. In Figure 3 we show the electric field calculated for the conducting ellipsoid, the flat-ended channel, and the capped channel with a length of 4 km. The electric field is calculated by using the stable method of moments for the flat-ended and capped channels, and the analytical method is used for the ellipsoid. The flat-ended channel and capped channel have a radius of 1 cm both along the channel and at the spherical caps. The ellipsoid has a fixed curvature radius of 1 cm at the tip. The ambient field strength is chosen to be 0.5 kV/cm, which corresponds to a total potential difference over the entire channel of 200 MV and 100 MV from its center (equation (6)). In addition, the two horizontal lines indicate $E_{max} = 50$ kV/cm and $E_{RREA} = 2.86$ kV/cm (sea level), and the dashed line indicates the conventional breakdown threshold, $E_{th} = 32$ kV/cm, sea level equivalent. In the smaller panel, we zoom in on the AM region between E_{max} and E_{RREA}.

From this comparison, we can see that the geometry has an important effect on how the electric field changes with distance from the tip of the leader. The ellipsoid has a much larger radius at the center of the channel. This results in a weaker maximum electric field compared to the flat-ended channel and capped channel geometry and also a more extended region where the field is above the RREA threshold. The tip of the capped channel is the most pointed and produces the strongest electric field, which is within roughly 1 cm of the tip. Most importantly, we have calculated the electric potential in the AM region to be roughly 26.6 MV for the ellipsoidal channel and 17.4 MV for the flat-ended and capped channels, respectively. However, the ellipsoid has an unrealistic radius at the center of the channel of 6.3 m and we will argue that the resulting shape of the electric field may also be unrealistic. The difference between the flat-ended channel and capped channel is negligible in the range of the AM region.

5.2. Potential Differences and Number of Avalanche Lengths in the AM Region

The initial conditions that are used in this paper are within the range observed for typical $^{+}$IC lightning and TGFs. These values are presented in Table 2, which gives the potential difference between the leader and the ambient potential at the tips, ΔU_{tip}. These are given by assumptions of different lengths, L, altitudes for

AGU Journal of Geophysical Research: Atmospheres 10.1002/2016JD026206

Table 2. The Upper Altitude, h, the Vertical Length, L, the Ambient Electric Field Strength, E_o, the Ratio of the Ambient Electric Field to the RREA Threshold at the Upper Altitude, $E_o/E_{RREA}(h)$, and the Corresponding Potential Difference From the Center to the Tips of the Leader ΔU_{tip} (equation (7))[a]

	h (km)	L (km)	E_o (kV/cm)	E_o/E_{RREA} (h)	ΔU (MV)
Rakov and Uman [2003]	11	6	0.2/0.4	0.26/0.53	120/240
Rakov and Uman [2003]	12	5	0.2/0.4	0.31/0.62	100/200
Marshall and Stolzenburg [2001]	9.9	3.4	0.38	0.42	65
Lu et al. [2010] and *Shao et al.* [2010]	14	5.5	0.3	0.64	165

[a]The values are derived from the references in the first column.

the upper leader tip, h, and ambient field strengths, E_o (calculated using equation (6)). The initial conditions are within the range of in situ measurements presented by *Marshall and Stolzenburg* [2001] and *Stolzenburg et al.* [2007]. Note that in the fourth row, we give the range of altitudes for $^+$IC leaders associated with the production of TGFs in *Shao et al.* [2010] and *Lu et al.* [2010]. Here we use the maximum vertical separation and an ambient electric field of 0.3 kV/cm, which is roughly 60% or the RREA threshold and consistent with *Marshall and Stolzenburg* [2001]. Although the vertical length of the leader and ambient electric field strengths only depend on the total charge in the charge layers and the vertical separation between them, the threshold field strengths (E_{max}, E_{th}, and E_{RREA}) scale with density and pressure. To accurately scale the threshold field strengths from sea level to the upper altitude of the leader, we use the atmospheric density profile from the MSIS database (http://omniweb.gsfc.nasa.gov/vitmo/msis_vitmo.html); the scaling can be described by

$$E(h) = E(0)\frac{n(h)}{n(0)}, \tag{9}$$

where $n(h)$ is the density at the upper altitude, h, of the leader channel.

For each of these cases, we estimate the sum of the ambient electric field and the leader electric field and determine the following parameters: (1) the threshold field strengths, $E_{max} = 50$ kV/cm, $E_{th} = 32$ kV/cm, and $E_{RREA} = 2.86$ kV/cm, at sea level density and pressure, scaled to the upper altitude of the leader channel (equation (9)); (2) the distances from the tip of the leader channel to where the electric field drops below the threshold field strengths; here l_{max} is the distance to E_{max}, l_{th} to E_{th}, and l_{RREA} to E_{RREA}; and (3) the potential differences that correspond to the regions between these values, where ΔU_o for $0 < l < l_{max}$, ΔU_1 for $l_{max} < l < l_{th}$, and ΔU_2 for $l_{th} < l < l_{RREA}$ (equation (7)).

From these values we determine (1) the potential difference in the AM region, $\Delta U_{AM} = \Delta U_1 + \Delta U_2$; (2) the total potential difference from the tip of the leader to the end of the AM region, $\Delta U_{tot} = \Delta U_o + \Delta U_{AM}$; and (3) the total number of avalanche lengths N_λ in the region from l_{th} to l_{RREA} (equation (5)).

The results are shown in Figure 4. In Figure 4 (top), we present the potential differences in the AM region ΔU_{AM}. In Figure 4 (middle), we present the ratio $\Delta U_{AM}/\Delta U_{tot}$, and in Figure 4 (bottom), we show the number of avalanche lengths in the AM region N_λ. These are plotted as a function of the potential difference from the tip of the leader to the end of the AM region, ΔU_{tot} (equation (6)).

Such potential calculations assume an isolated straight channel, but in natural lightning this may not be the case. Therefore, we also introduce the effect of horizontal development and branching of the leader channel in the negative charge region. The lightning leader is typically initiated close to the main negative charge region where the charge density is higher and therefore the electric field is stronger. While the negative end of the leader is directed away from the negative charge region, the positive end develops within the negative charge region. If the positive channel develops horizontally and branches within the negative charge region, the channel may be approximated as a perfectly (or partly) conducting surface and thus acts as a mirror channel to the negative end. Using the method of images, one can show that the resulting electric field can be calculated as if the channel is twice the actual vertical extension. The potential difference over the entire length of the leader then becomes correspondingly larger. This process was also introduced in *Mallios et al.* [2013]. To consider this potential difference to be doubled is an extreme assumption and can be considered to be the upper limit. The actual potential difference ahead of the negative end of the leader will be less than doubled as the branched channels at the positive end of the leader never form a perfectly

AGU Journal of Geophysical Research: Atmospheres 10.1002/2016JD026206

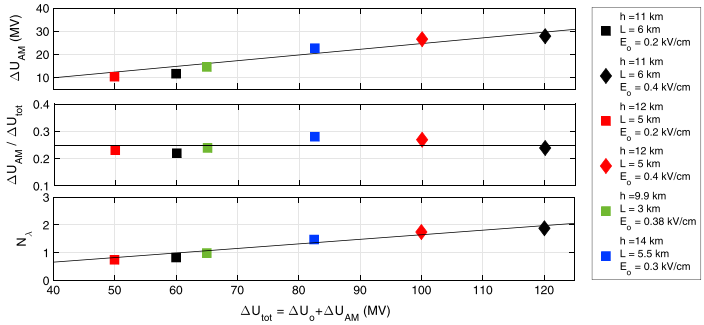

Figure 4. Results for each of the initial conditions given in Table 2. (top) The potential difference in the AM region ΔU_{AM}. (middle) The ratio between the potential differences in the AM region and the sum of the potential difference in the high-field region and the AM region, $\Delta U_{AM}/\Delta U_{tot}$. (bottom) The number of avalanche lengths, N_λ, in the AM region. The results are plotted as a function of ΔU_{tot}. The black lines in Figure 4 (top and bottom) correspond to the best fit linear function of the data points. The slope of the function in Figure 4 (top) coincides with the mean value of the data points in Figure 4 (middle), which is also plotted as a black line.

conducting plane. The results in Figure 5 show the effect of taking into account horizontal development of the positive end of the leader.

6. Discussion

6.1. The Relative Importance of the Ambient Electric Field

From balloon soundings one can see that the ambient electric field is less dependent on density and altitude but is related to the amount of charge in the charge regions [*Stolzenburg et al.*, 2007]. Thus, the effect of the ambient electric field becomes more important with increasing altitude and must be taken into account. To illustrate the significance of the ambient electric field, we estimate the ratio of the ambient potential difference in the AM region, ΔU_{amb}, versus the total potential difference in the AM region, ΔU_{AM}, that is, the second (right side) and first (left side) terms of equation (7), respectively. The results are plotted in Figure 6, for leader lengths of 3 km and 6 km and an ambient electric field strength of 0.4 kV/cm. This field strength constitutes between 30% and 99% of the RREA threshold (lower *x* axis) at assumed upper altitudes of the leader (upper *x* axis) from 7 km to 15 km. With these results, we find that for a given length, the relative importance of

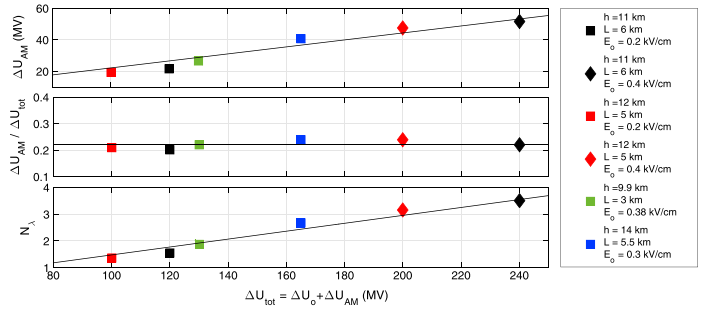

Figure 5. Results for each of the initial conditions given in Table 2 when taking into account the effect of horizontal development of the positive end of the leader. (top) The potential difference in the AM region ΔU_{AM}. (middle) The ratio between the potential differences in the AM region and the sum of the potential difference in the high-field region and the AM region, $\Delta U_{AM}/\Delta U_{tot}$. (bottom) The number of avalanche lengths, N_λ, in the AM region. The results are plotted as a function of ΔU_{tot}. The black lines correspond to the best fit linear functions in Figure 5 (top and bottom). The black lines in Figure 5 (top and bottom) correspond to the best fit linear function of the data points. The slope of the function in Figure 5 (top) coincides with the mean value of the data points in Figure 5 (middle), which is also plotted as a black line.

AGU Journal of Geophysical Research: Atmospheres 10.1002/2016JD026206

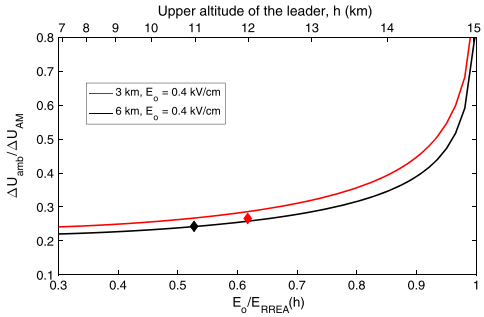

Figure 6. The ratio of $\Delta U_{amb}/\Delta U_{AM}$ as a function of $E_o/E_{RREA}(h)$, where h is the upper altitude of the leader shown on the upper x axis, for leader lengths of 3 km and 6 km in an ambient electric field of $E_o = 0.4$ kV/cm. The data points correspond to the first (black) and second (red) rows of Table 2, for an ambient electric field of 0.4 kV/cm. Note that we use the same symbol and colors as for the values plotted in Figure 4.

the ambient electric field only depends on the ratio $E_o/E_{RREA}(h)$. However, with increasing length of the leader, the ratio, $\Delta U_{amb}/\Delta U_{AM}$, decreases as the leader electric field becomes more important, which is expected. For ratios of $E_o/E_{RREA}(h)$ below 0.7, the relative importance of the ambient electric field is near constant. It is also interesting that at altitudes where the ambient electric field strength constitutes more than roughly 96% of the RREA threshold, the ambient electric field contributes more than the leader electric field to the potential difference in the AM region. Such fields can exist in local regions of a few hundred meters scale in the thundercloud, however, not over the full length of developed leader channels [*Stolzenburg et al.*, 2007]. It is clear that the role of the ambient electric field becomes increasingly important at higher altitudes.

6.2. Potential Differences and Number of Avalanche Lengths in the AM Region

In Monte Carlo models, the threshold field strengths are given from the density used in the simulations. However, the estimated electric field only depends on the geometry of the leader channel and the assumed ambient electric field (equation (6)). This is critical when choosing how close to the leader tip the seed electrons can be initiated. Some models have made the strong assumption that the seed electrons can be initiated in the very high field region, denoted ΔU_o in Figure 1. At the distance of initiation, we have calculated the electric field to be roughly 8 times (at 30 cm) in *Xu et al.* [2012], 74 times (30 cm) in *Köhn and Ebert* [2015], and 60 times (15 cm) in *Celestin et al.* [2012], stronger than the conventional breakdown threshold. The potential difference in the AM region ΔU_{AM} was then 26.9 MV, 83.4 MV, and 145.0 MV, respectively. If we use the definition of the AM region as presented in this paper, and take into account scaling of the threshold field strengths, the corresponding potential differences become 17.7 MV, 26.6 MV, and 62.0 MV. *Köhn and Ebert* [2015] argue that high-energy electrons will be accelerated faster than the streamer zone can develop and that the effects of the streamer zone therefore can be neglected. This is only true if all the charges arrive at the tip of the channel instantaneously. To fully understand the maximum strength of the leader electric field and the initial position of the seed electrons, a better knowledge of the initial development of the streamer zone is necessary.

Figures 4 (top) and 5 (top) show that the potential difference in the AM region ΔU_{AM} ranges from ~10 MV to 52 MV, depending on whether horizontal branching of the leader is taken into account. These results also show that the potential ΔU_{AM} has a linear dependence on the total potential U_{tot} of the leader. In Figures 4 (middle) and 5 (middle), one can see that ΔU_{AM} is nearly constant at 24% and 22% of ΔU_{tot} in the two figures, respectively. While this ratio is expected to increase for very small potentials as the high-field region disappears, the nearly constant behavior covers the range of potentials roughly above 15 MV. This is in agreement with Figure 6, which shows the relative importance of the ambient field strength, for the given ratios of $E_o/E_{RREA}(h)$ (see Table 2). The potential difference ΔU_{AM} is directly related to the maximum energy that the accelerated electrons can achieve. Thus, a 52 MV potential difference can accelerate electrons to a maximum energy of 52 MeV, which can produce a much lower flux of photons that are equally energetic. However, due to the friction force experienced by the electrons, the energy of most of the electrons is expected to be less. This can be approximated by a fraction corresponding to the minimum friction force over the length of the AM region, that is $F_e = 2.0$ keV/cm at sea level [*Moss et al.*, 2006]. That gives a loss to friction of ~14 MeV over the AM region, which is $l_{max} - l_{RREA} \approx 270$ m at 11 km altitude. From these results, we can conclude that most of the electrons are expected to have energies below 38 MeV. Correspondingly, the photon energy distribution produced by these electrons will have energies weaker than that of the electrons. A rough estimate of the average energy gain can be derived from equation (2) [*Dwyer*, 2003; *Dwyer et al.*, 2012; *Skeltved et al.*, 2014]. An average energy of 7.3 MeV, or less, of avalanche length can then be expected. That corresponds to roughly 25 MeV. Thus, the candidates considered in this paper are of insufficient energy to explain the observed

AGU Journal of Geophysical Research: Atmospheres 10.1002/2016JD026206

maximum energies of TGFs of at least 40 MeV [*Marisaldi et al.*, 2010]. Note that this result depends on the assumed initial position of the electrons (boundaries of the AM region).

To explain the photon intensity and energy distribution of TGFs, an electron energy distribution with an exponential cutoff at between 7.0 MeV and 7.3 MeV has been inferred [*Dwyer and Babich*, 2011; *Xu et al.*, 2012; *Skeltved et al.*, 2014]. This spectrum is typical for a fully developed RREA and is called the RREA spectrum. *Celestin et al.* [2015] used the same electric field constraints that have been implemented in this study but used sea level density and pressure. They showed that to reach a fully developed RREA spectrum, the potential difference from the center of the leader to its tip ΔU_{tip} must be approximately 300 MV. In *Dwyer and Babich* [2011], simulations in a homogeneous electric field showed that a steady state electron distribution can be obtained at less than 5 avalanche lengths. We have estimated the number of avalanche lengths N_λ in the AM region (see Figures 4 (bottom) and 5 (bottom)). The values ranges from 0.7 to 3.5 depending on whether horizontal branching in the MN charge region is taken into account. The maximum potential difference between the lower and upper tips of the leaders considered in this study is 240 MV, which is less than that used by *Celestin et al.* [2015] and may be insufficient to produce a fully developed RREA spectrum. Thus, with our assumptions about E_{max}, E_o, length and upper altitude, and when horizontal branching of the leader is taken into account, only the maximum value of our results can be considered a candidate to obtain a fully developed RREA spectrum.

6.3. Can the Electric Field Ahead of Lightning Leaders Produce TGFs?

We have introduced new constraints and evaluated the leader electric field for assumptions derived from in situ measurements. From these results we will argue that if the energy loss due to friction is taken into account, these conditions are insufficient to explain a high flux of bremsstrahlung photons with energies of up to ~40 MeV, which is the observed maximum energy of TGFs [*Marisaldi et al.*, 2010]. By comparing our results to the results by *Celestin et al.* [2015], we find that only the maximum value of our results can be considered a candidate to obtain a fully developed RREA spectrum; this correspond to ~3.5 avalanche lengths in the AM region. To explain the maximum energies of TGFs, only leaders with potential differences between its tips of more than 500 MV can be considered. Note that this requires the assumption that horizontal branching of the leader channel in the MN charge region occurs. As far as we know, such large potential differences has not been observed.

Although we will argue that the maximum constraint on the electric field is realistic, Figures 4 (middle) and 5 (middle) show that with this constraint, only $\sim 24 \pm 3\%$ (Figure 4) and $22 \pm 2\%$ (Figure 5) of the total potential difference from the tip of the leader to the end of the AM region ΔU_{tot} is within the AM region. Thus, 75%–80% is excluded. This may change if screening of the electric field, due to the effects of ionization during the leader step, is taken into account. If a larger fraction of ΔU_{tot} is within the AM region, the maximum energies of the electrons, and hence the bremsstrahlung photons, can become correspondingly larger.

Furthermore, most observed TGFs have energies below 40 MeV [*Smith et al.*, 2005; *Briggs et al.*, 2010; *Marisaldi et al.*, 2010] and some are within the energy range of the candidates considered in this paper. However, with our assumptions, these candidates cannot explain a fully developed RREA spectrum.

7. Conclusion

In this paper, we have modeled the electric field ahead of the leader tip and evaluated how it can accelerate and multiply high-energy electrons. We have used initial conditions that are consistent with electric field measurements of thunderclouds and estimates of the production altitudes of TGFs. Finally, we have argued that the potential difference ahead of a lightning leader can be increased by a factor of up to 2 due to horizontal development and branching of the positive end of the leader.

1. We have argued that the maximum electric field strength that can exist in the region ahead of the leader tip depends on how quickly the potential increases at that tip. As the timescale of the increase of the potential is not well understood, we set an upper limit to $E_{max} = 1.5 \cdot E_{th} \sim 50$ kV/cm. The lower limit is the electric field threshold required to sustain RREAs, $E_{RREA} = 2.86$ kV/cm, at sea level. Comparisons with existing models have shown that these constraints have important effects on the potential difference, and therefore the number of avalanche lengths, in the AM region.
2. By relating the boundary conditions of the AM region to the threshold field strengths, we have shown that scaling the maximum field and RREA threshold is important. It determines how close to the leader tip seed

AGU Journal of Geophysical Research: Atmospheres 10.1002/2016JD026206

electrons can be initiated and the extent of the AM region. This scaling is important to correctly estimate the potential difference in the AM region.

3. We have shown that the relative importance of the ambient field to the leader field, on their respective contributions to the potential drop in the AM region ($\Delta U_{amb}/\Delta U_{AM}$), is nearly constant for ratios below ~0.7 but increases significantly at higher altitudes. For a ratio of more than 0.96, the relative importance of the ambient electric field is higher than that of the leader electric field. We also show that the ratio depends slightly on the length of the leader (given the same ambient electric field). Although the relative importance of the ambient electric field, compared to the leader electric field, increases significantly, thermal acceleration of low-energy electrons to become seed electrons is still necessary to explain the production of TGFs.
4. Given our assumptions of E_{max} and E_o, we find that the maximum potential difference in the AM region is roughly 52 MV corresponding to a maximum number of avalanche lengths of roughly $N_\lambda = 3.5$. This is obtained for a potential difference between the leader and the ambient potential at the leader tip ~240 MV (480 MV over the entire vertical length of the leader) and assumes horizontal branching of the channel in the MN charge region. These values are insufficient to explain the maximum photon energy associated with observed TGFs and close to the minimum required to produce a fully developed RREA spectrum.

Appendix A: Method of Moments for an Electrostatic Problem

A1. Basic Terms

The Poisson equation $\nabla^2\phi = -\rho/\epsilon_0$ may be represented as

$$\int G(\mathbf{r},\mathbf{r}')\rho(\mathbf{r}')\,\mathrm{d}^3\mathbf{r}' = \phi(\mathbf{r}), \qquad G(\mathbf{r},\mathbf{r}') = \frac{1}{4\pi\epsilon_0|\mathbf{r}-\mathbf{r}'|} \tag{A1}$$

In some problems, such as a conductor placed in an external field, this equation has to be solved for ρ with given ϕ and thus is a Fredholm integral equation of the first kind. It may be written symbolically as

$$\hat{\mathrm{G}}\rho = \phi \tag{A2}$$

where $\hat{\mathrm{G}}$ is a linear operator and ρ and ϕ are functions.

The methods of moments is a method of solving (A1) or (A2) by discretization; i.e., $\hat{\mathrm{G}}$ is represented as a matrix while ρ and ϕ as vectors. We approximate the unknown function as a linear combination of *basis (expansion) functions* u_i:

$$\rho(\mathbf{r}) \approx \sum_i \rho_i u_i(\mathbf{r}) \tag{A3}$$

and try to satisfy (A2) with a discrete number of conditions

$$\phi_j = (w_j, \phi)$$

where w_j are the *testing (weighting) functions* and the scalar product is defined as

$$(f,g) \equiv \int f(\mathbf{r})g(\mathbf{r})\,\mathrm{d}\mathbf{r}$$

Substituting the discretized ρ, we get a system of linear equations

$$\sum_i G_{ji}\rho_i = \phi_j \tag{A4}$$

where $G_{ji} \equiv (w_j, \hat{\mathrm{G}}u_i)$, which may be solved if matrix G_{ji} is invertible.

A2. Surface and "Axis" Discretization Algorithms

Let us consider a cylindrically symmetric conducting object in the cylindrical system of coordinates $\mathbf{r} = \{r_\perp, \theta, z\}$. The object surface is described parametrically

$$z = Z(\tau), \qquad r_\perp = R(\tau), \qquad \tau_{min} < \tau < \tau_{max}$$

AGU Journal of Geophysical Research: Atmospheres 10.1002/2016JD026206

In the problem solved in this paper, the external field is uniform and axial, $\phi = -E_0 z$, and therefore, due to symmetry, neither ρ nor ϕ depend on the azimuthal angle θ. Moreover, the charge is concentrated on the surface:

$$\rho(\mathbf{r}) = \int_{\tau_{\min}}^{\tau_{\max}} \lambda(\tau) S(\mathbf{r}, \tau)\, \mathrm{d}\tau, \qquad S(\mathbf{r}, \tau) = \frac{\delta\left[r_\perp - R(\tau)\right]}{2\pi R(\tau)} \delta[z - Z(\tau)]$$

where λ is the linear charge density (in τ) and S describes the surface shape in terms of Dirac delta functions.

The basis (expansion) functions $u_i(\mathbf{r})$, $i = 1 \ldots N$ are represented in terms of basis functions $u_i^\tau(\tau)$ in τ:

$$u_i(\mathbf{r}) = \int_{\tau_{\min}}^{\tau_{\max}} u_i^\tau(\tau) S(\mathbf{r}, \tau)\, \mathrm{d}\tau$$

We take $u_i^\tau(\tau) = 1/\Delta\tau_i$ when $\tau \in (\tau_i, \tau_{i+1})$ and zero otherwise ("pulse" functions), with $\Delta\tau_i = \tau_{i+1} - \tau_i$, $\tau_1 = \tau_{\min}$, $\tau_{N+1} = \tau_{\max}$.

Although $u_j(\mathbf{r})$ are the same in the surface and axis methods, the choice of the testing (weighting) functions w_j is different. In the surface method we take $w_j \equiv u_j$. Thus, we evaluate the potential at the surface:

$$(u_j, \phi) = \frac{1}{\Delta\tau_i} \int_{\tau_i}^{\tau_{i+1}} \phi\left[R(\tau), Z(\tau)\right]\, \mathrm{d}\tau$$

In the axis method of *Balanis* [2012], however, $w_j \neq u_j$ as the potential is evaluated on the axis in the center of the jth surface element:

$$(w_j, \phi) = \phi\left(0, Z_j\right)$$

where Z_j is an average value of $Z(\tau)$ in $\tau \in (\tau_j, \tau_{j+1})$, i.e., $w_j(\mathbf{r}) = \delta(\mathbf{r}_\perp)\delta(z - Z_j)$.

The discretized operator $\hat{\mathrm{G}}$ in the surface method is

$$G_{ji} = (u_j, \hat{\mathrm{G}} u_i) = \int \frac{u_j(\mathbf{r}) u_i(\mathbf{r}')}{4\pi\epsilon_0 |\mathbf{r} - \mathbf{r}'|}\, \mathrm{d}\mathbf{r}\, \mathrm{d}\mathbf{r}' = \int \mathrm{d}\tau_1 \int \mathrm{d}\tau_2\, u_j^\tau(\tau_1) u_i^\tau(\tau_2) G(\tau_1, \tau_2)$$

where

$$G(\tau_1, \tau_2) = \int \frac{S(\mathbf{r}, \tau_1) S(\mathbf{r}', \tau_2)}{4\pi\epsilon_0 |\mathbf{r} - \mathbf{r}'|}\, \mathrm{d}\mathbf{r}\, \mathrm{d}\mathbf{r}' = \int_0^{2\pi} \frac{1}{4\pi\epsilon_0 \sqrt{\left[Z(\tau_1) - Z(\tau_2)\right]^2 + \left[R(\tau_1) - R(\tau_2)\cos\chi\right]^2 + \left[R(\tau_2)\sin\chi\right]^2}} \frac{\mathrm{d}\chi}{2\pi}$$

which evaluates to

$$G(\tau_1, \tau_2) = \frac{K(m)}{2\pi^2 \epsilon_0 D_+}, \quad m = \frac{4R(\tau_1)R(\tau_2)}{D_+^2} = 1 - \frac{D_-^2}{D_+^2}, \quad D_\pm^2 = \left[Z(\tau_1) - Z(\tau_2)\right]^2 + \left[R(\tau_1) \pm R(\tau_2)\right]^2$$

where $K(m)$ is the complete elliptic integral of the first kind. The second version of expression for m may be used when elements are close to each other, i.e., $D_- \to 0$ so that $m \approx 1$. We substitute it into the above expression for G_{ji} which is evaluated numerically. We note that $G(\tau_1, \tau_2)$ is infinite at $\tau_1 = \tau_2$ (because then $m = 1$), which occurs in calculation of diagonal elements G_{ji}, but the singularity can be integrated through. We may comment that avoiding singularity was the motivation of *Balanis* [2012] to use the axis testing (weighting) functions. However, this leads to a much more serious problem of numerical instability, which we will shortly discuss.

A3. Discussion of Stability

Operator represented by Green's function G in (A1) is symmetric and positive definite, which is demonstrated by evaluating it in wave vector $\mathbf{k}$ domain, where it is diagonal with values $\tilde{G}(\mathbf{k}) = \frac{1}{\epsilon_0 |\mathbf{k}|^2} > 0$ for all $\mathbf{k} \neq 0$. These properties mean that solving (A2) is equivalent to minimizing the functional of ρ

$$U[\rho] = \frac{1}{2}(\rho, \hat{\mathrm{G}}\rho) - (\rho, \phi) \to \min \text{ over } \rho(\mathbf{r}) \tag{A5}$$

and the minimum exists.

AGU Journal of Geophysical Research: Atmospheres 10.1002/2016JD026206

After a discretization which is symmetric (i.e., the basis and testing functions are the same, $u_i \equiv w_i$), which is the case in the surface method, the discretized matrix G_{ji} remains a positive-definite symmetric matrix and solving (A4) is still equivalent to a minimization problem (A5) but on a limited set of functions ρ given by (A3). As this limiting becomes less and less restrictive when we decrease the element size, the minimum should get closer and closer to the unconstrained solution. The actual speed of convergence probably depends on how we choose our basis (expansion) functions u_i. A robust analysis of the convergence speed was beyond the efforts we were willing to spend on this paper.

In the axis method, however, the discretized operator $G_{ji}^{\text{axis}} = (w_j, \hat{\text{G}}u_i)$ is neither symmetric nor positive definite, and there is no analogous minimization problem. The method becomes unstable when element sizes are smaller than the radius of the conductor. This may be understood by the following reasoning. The oscillations in ρ with wavelength $l \ll R$ (which can be as small as the element size, $l_{\text{min}} = 2\Delta Z$) on the surface create only very small oscillations in ϕ on the axis, with suppression factor $\sim e^{-2\pi R/l}$. This means that when we solve for ρ, very small fluctuations of ϕ on the axis are amplified by a large factor $e^{2\pi R/l} \sim e^{\pi R/\Delta Z}$. The inability to use small elements leads, among other things, to inability to accurately calculate fields close to the conductor.

Acknowledgments
This study was supported by the European Research Council under the European Union's Seventh Framework Programme (FP7/2007-2013)/ERC grant agreement 320839 and the Research Council of Norway under contracts 208028/F50, 216872/F50, and 223252/F50 (CoE). The data used in this paper are generated by the use of the surface method of moments as described in the appendix, with the specified conditions from the main body of the paper.

References

Balanis, C. A. (2012), *Advanced Engineering Electromagnetics*, 2nd ed., John Wiley, New York.
Bazelyan, E. M., and Y. P. Raizer (2000), *Lightning Physics and Lightning Protection*, 1st ed., pp. 27–137, Nicki Dennis, New York.
Briggs, M. S., et al. (2010), First results on terrestrial gamma ray flashes from the Fermi Gamma-ray Burst Monitor, *J. Geophys. Res.*, *115*, A07323, doi:10.1029/2009JA015242.
Carlson, B. E. (2009), *Terrestrial Gamma-Ray Flash Production by Lightning*, PhD thesis, Stanford Univ., Stanford, Calif.
Carlson, B. E., N. G. Lehtinen, and U. S. Inan (2007), Constraints on terrestrial gamma ray flash production from satellite observation, *Geophys. Res. Lett.*, *34*, L08809, doi:10.1029/2006GL029229.
Carlson, B. E., N. G. Lehtinen, and U. S. Inan (2010), Terrestrial gamma ray flash production by active lightning leader channels, *J. Geophys. Res.*, *115*, A10324, doi:10.1029/2010JA015647.
Celestin, S., and V. P. Pasko (2011), Energy and fluxes of thermal runaway electrons produced by exponential growth of streamers during the stepping of lightning leaders and in transient luminous events, *J. Geophys. Res.*, *116*, A03315, doi:10.1029/2010JA016260.
Celestin, S., W. Xu, and V. P. Pasko (2012), Terrestrial gamma ray flashes with energies up to 100 MeV produced by nonequilibrium acceleration of electrons in lightning, *J. Geophys. Res.*, *117*, A05315, doi:10.1029/2012JA017535.
Celestin, S., W. Xu, and V. P. Pasko (2015), Variability in fluence and spectrum of high-energy photon bursts produced by lightning leaders, *J. Geophys. Res. Space Physics*, *120*, 712–723, doi:10.1002/2015JA021410.
Coleman, L. M. (2003), Effects of charge and electrostatic potential on lightning propagation, *J. Geophys. Res.*, *108*(D9), 4298, doi:10.1029/2002JD002718.
Coleman, L. M., and J. R. Dwyer (2006), Propagation speed of runaway electron avalanches, *Geophys. Res. Lett.*, *33*, L11810, doi:10.1029/2006GL025863.
Cooray, V. (2015), *An introduction to lightning*,1st ed., Springer, Uppsala, Sweden, doi:10.1007/978-94-017-8938-7.
Cummer, S. A., Y. Zhai, W. Hu, D. M. Smith, L. I. Lopez, and M. A. Stanley (2005), Measurements and implications of the relationship between lightning and terrestrial gamma ray flashes, *Geophys. Res. Lett.*, *32*, L08811, doi:10.1029/2005GL022778.
Cummer, S. a., G. Lu, M. S. Briggs, V. Connaughton, S. Xiong, G. J. Fishman, and J. R. Dwyer (2011), The lightning-TGF relationship on microsecond timescales, *Geophys. Res. Lett.*, *38*, L14810, doi:10.1029/2011GL048099.
Cummer, S. A., F. Lyu, M. S. Briggs, G. Fitzpatrick, O. J. Roberts, and J. R. Dwyer (2015), Lightning leader altitude progression in terrestrial gamma-ray flashes, *Geophys. Res. Lett.*, *42*, 7792–7798, doi:10.1002/2015GL065228.
Dwyer, J. R. (2003), A fundamental limit on electric fields in air, *Geophys. Res. Lett.*, *30*(20), 2055, doi:10.1029/2003GL017781.
Dwyer, J. R. (2007), Relativistic breakdown in planetary atmospheres, *Phys. Plasmas*, *14*(4), 42901, doi:10.1063/1.2709652.
Dwyer, J. R. (2012), The relativistic feedback discharge model of terrestrial gamma ray flashes, *J. Geophys. Res.*, *117*, A02308, doi:10.1029/2011JA017160.
Dwyer, J. R., and L. P. Babich (2011), Low-energy electron production by relativistic runaway electron avalanches in air, *J. Geophys. Res.*, *116*, A09301, doi:10.1029/2011JA016494.
Dwyer, J. R., and D. M. Smith (2005), A comparison between Monte Carlo simulations of runaway breakdown and terrestrial gamma-ray flash observations, *Geophys. Res. Lett.*, *32*, L22804, doi:10.1029/2005GL023848.
Dwyer, J. R., D. M. Smith, and S. A. Cummer (2012), High-energy atmospheric physics: Terrestrial gamma-ray flashes and related phenomena, *Space Sci. Rev.*, *173*, 133–196, doi:10.1007/s11214-012-9894-0.
Gjesteland, T., N. Østgaard, P. H. Connell, J. Stadsnes, and G. J. Fishman (2010), Effects of dead time losses on terrestrial gamma ray flash measurements with the Burst and Transient Source Experiment, *J. Geophys. Res.*, *115*, A00E21, doi:10.1029/2009JA014578.
Gjesteland, T., et al. (2015), Observation of intrinsically bright terrestrial gamma ray flashes from the Mediterranean basin, *J. Geophys. Res. Atmos.*, *120*, 12,143–12,156, doi:10.1002/2015JD023704.
Gurevich, A. V., and K. P. Zybin (2001), Runaway breakdown and electric discharges in thunderstorms, *Physics-Uspekhi*, *44*(11), 1119–1140, doi:10.1070/PU2001v044n11ABEH000939.
Gurevich, a. V., G. M. Milikh, and R. Roussel-Dupré (1992), Runaway electron mechanism of air breakdown and preconditioning during a thunderstorm, *Phys. Lett. A*, *165*(5-6), 463–468, doi:10.1016/0375-9601(92)90348-P.
Harrington, R. F. (1993), *Field Computation by Moment Method*, IEEE ed., Macmillan Publ. Comp., Arizona.
Inan, U. S., S. C. Reising, G. J. Fishman, and J. M. Horack (1996), On the association of terrestrial gamma-ray bursts with lightning and implications for sprites, *Geophys. Res. Lett.*, *23*(9), 1017–1020.
Kasemir, H. W. (1960), A contribution to the electrostatic theory of a lightning discharge, *J. Geophys. Res.*, *65*(7), 2156–2202, doi:10.1029/JZ065i007p01873.
Köhn, C., and U. Ebert (2015), Calculation of beams of positrons, neutrons, and protons associated with terrestrial gamma ray flashes, *J. Geophysi. Res. Atmos.*, *120*, 1620–1635, doi:10.1002/2014JD022229.